Distribution Agreement

Signature:

Yonglun Jiang

Date

Effects of polydispersity and Isomorph Theory on shearing soft glassy materials

By

Yonglun Jiang
Doctor of Philosophy

Department of Physics

Eric R. Weeks, Ph.D.
Advisor

Justin C. Burton, Ph.D.
Committee Member

Hayk Harutyunyan, Ph.D.
Committee Member

Connie B. Roth, Ph.D.
Committee Member

Peter J. Yunker, Ph.D.
Committee Member

Nicholas P. Bailey, Ph.D.
Committee Member

Accepted:

Kimberly Jacob Arriola, Ph.D.
Dean of the James T. Laney School of Graduate Studies

Date

Effects of polydispersity and Isomorph Theory on shearing soft glassy materials

By

Yonglun Jiang
B.A., University of Science and Technology of China, 2016

Advisor: Eric R. Weeks, Ph.D.

An abstract of
A dissertation submitted to the Faculty of the
James T. Laney School of Graduate Studies of Emory University
in partial fulfillment of the requirements for the degree of
Doctor of Philosophy
in Department of Physics
2022

Abstract

Effects of polydispersity and Isomorph Theory on shearing soft glassy materials
By Yonglun Jiang

My PhD work consists of two simulation projects. One is to study the effect of polydispersity on the dense 2D granular system under steady shear. We use the Durian bubble model together with Lees-Edwards boundary conditions to generate the shear on our systems with exponential size distributions with various size spans. Then we compare the results with conventional bidisperse system. Shear produces a mean affine flow, and nonaffine plastic deformations resulting from local rearrangements. We calculate the deviation from the affine flow to quantify the nonaffinity for individual particles. We also calculate the deviation from the local group affine motions to quantify the local plastic deformation. We find that both of them significantly depend on the particle size as well as the positions to other particles within the system. In contrast to bidisperse systems, the large particles in our simulations cause a new flow pattern for the relatively smaller particles. This flow pattern leads to more complicated ways of rearrangements that are the origins of the new behaviors we find. We further demonstrate a quantitative way to distinguish between "large" and "small" particles. Finally, we show how these results become increasingly important as the particle size distribution broadens. These findings are qualitatively different than previously found in bidisperse systems.

The other project is to apply the isomorph theory on the glassy simple system under simple shear. After cooling the Kob-Andersen binary Lennard-Jones system below the glass transition, we generate a so-called isomorph from the fluctuations of potential energy and virial in the NVT ensemble: a set of density, temperature pairs for which structure and dynamics are identical when expressed in appropriate reduced units. To access dynamical features, we shear the system using the SLLOD algorithm coupled with Lees-Edwards boundary conditions and study the statistics of stress fluctuations and the particle displacements transverse to the shearing direction in steady state. We find good collapse of the statistical data, showing that isomorph theory works well in this regime. The analysis of the distribution of stress fluctuations allows us to identify a clear signature of avalanche behavior in the form of an exponential tail on the negative side. This feature is also isomorph invariant. We then investigate further and turn our focus on the transient part of the stress and strain curve when the system yields. For the study here, we investigate a much larger density span over which the performance of various isomorph generating methods needs to be examined. Comparisons and comments on these methods are provided. We then shear the system along the identified isomorph. Here since the transient part depends on the thermal history, we shear the glassy samples generated by different cooing rates with different strain rates. Excellent collapsing quality again for steady state stress is verified. We notice however, that the peak stress at the transient part on the stress strain curve is not invariant, but decreases by a few percent for each ten percent increase in density, although the differences decrease with increasing density.

Effects of polydispersity and Isomorph Theory on shearing soft glassy materials

By

Yonglun Jiang
B.A., University of Science and Technology of China, 2016

Advisor: Eric R. Weeks, Ph.D.

A dissertation submitted to the Faculty of the
James T. Laney School of Graduate Studies of Emory University
in partial fulfillment of the requirements for the degree of
Doctor of Philosophy
in Department of Physics
2022

Acknowledgments

First of all, I would like to thank my advisor Eric Weeks, for his patient explanations, the insightful discussions and conversations we had, and all the invaluable advice he gave. Eric is perhaps the nicest person I have ever met who treat everyone equally and politely, which is more important to me than any research suggestions he gave. My ultimate life goal is to become a professor like him. He is smart and able to give me intuitive and constructional ideas and comments which help me keep moving forward along our investigation. I feel so lucky that I made my decision to join Emory and work with him six years ago and I hope that we can still work together to answer more soft matter questions after my graduation.

I also want to thank Nicholas Bailey, Nick, at Roskilde University in Denmark, who is one of my committee meeting members and actually more like one other advisor to me. Nick is also a nice person, just like Eric. And I really enjoy our investigations, the three of us, me, Nick, and Eric together. Again, I feel so lucky that I applied to your summer internship program four years ago and I hope that we can keep our collaboration later if some of us find interesting research questions that we can work together.

I also would like to thank my committee members Justin Burton, Connie Roth, Hayk Harutyunyan, and Peter Yunker for their support, useful suggestions to both my research and time schedule plan towards my graduation, as well as sharing their own working experiences and stories to me, which are all of great importance to me. Also my appreciation to Minsu Kim for supervising my rotation project and I still remember the story Minsu shared with me and his own experience changing from soft matter to biophysics research. And Daniel Sussman, I'd like to thank him for invaluable discussion with us.

I then would like to thank Jirui Qiu, Yiqing Xiao, and Cong Cao who helped me with starting my life at Atlanta. Thank Carlos Orellana for helping me start the experiment and IDL coding, as well as some Spanish sentences that are not appropriate to speak to other people in public haha. Thank Stefan Zotovic, my first office mate, for letting me know that Serbia and China are good friends. There are just too many people appearing in my life for the past six years and it's just too difficult to list all of them. I would like to express my appreciation to all of you. Thanks to all the staff, especially Barbara Conner and Jason Boss, for their patient help with paperwork, electronic and mechanical techniques.

My special thank to my roommates, both current and previous ones, Wenxuan Xu, Guanxiong Chen, Yixuan Han, Chentao Li and his girlfriend Wenting, and Pengfei Tang for being constant sources of support and making my life colorful.

Then my friends, both in China and the U.S, especially Zhenmian and she Jia, Xinran and her parents, for so many free meals, and my old high school friends like Shufang, Wanting, Xiaobei, and Xiaojianjian for chatting with me, which is constant support to my life.

Most importantly, thanks to my parents Xiangping Jiang and Yanlan Lv for their unconditional faith in me all the times. Their support, encouragement, and endless love would be the most invaluable treasure in my life. They will always be my beloved ones.

Finally, I want to thank the National Science Foundation for the grant CBET-1804186 for the financial support for my research. I also would like to thank the physics department, Laney Graduate School and Emory University for the help.

Contents

List of Figures

List of Tables

List of Algorithms

Chapter 1

Introduction

1.1 Amorphous materials and three control parameters

Mayonnaise can support its own weight like a solid but also flow under external stress like liquid. Similar materials, sharing both solid and liquid properties, are known generally as amorphous materials. One of the most important features of such materials is the microscopic disordered structure, like liquids. Many of them can nonetheless possess very solid-like properties such as high strength and stiffness, smooth surfaces, and brittle failures under overwhelming external stress. For decades, people have been trying to connect this irregular disordered structure at any scales to the macroscopic material properties and behaviors. Part of my work recorded here, in some sense, is to add one brick to this big building. Based on the sizes of the individual particles, various systems have been investigated from a few nanometers, such as metallic glass, to centimeter scale such as granular materials including grains and disks. In between, people also study from small to large, polymer glasses, colloids (solid particles dispersed in liquid like ink and toothpaste), foams (bubbles of gas in a liquid like shaving cream) and emulsions (droplets of one liquid present in a second immiscible liquid like mayonnaise). Corresponding computation works have also been done and various models and theories have been proposed to address the question mentioned above, how to understand the macroscopic behaviors of the system from the microscopic, individual particle level. Let me first introduce some background information about what people generally care about for these systems from the "macro" point of view.

There are three major parameters controlling the macroscopic properties and behaviors of the amorphous systems. First of all, density ρ, the total mass of particles divided by the volume of the system (number density is also frequently used when the mass of each particle is the same). Volume fraction in 3D and area fraction ϕ in 2D are also used, defined as the total volume (area in 2D) of particles divided by the system volume (area in 2D). Take colloidal systems in 3D as an example. When the volume fraction is low below 0.494, the system is in general a liquid in equilibrium. With the increase of volume fraction, the system can either crystallize when the size distribution of the particles in the system is monodisperse and fully crystallized above a value of 0.545, as shown in Fig. 1.1 by the top arrows. However, the crystal state or crystalization process is not what we would like to investigate. The alternative route for increasing volume fraction is that the system can enter a supercooled liquid state (see next paragraph for definition of supercooled liquid) when the particles are more polydisperse or unable to crystallize. For supercooled liquid system, further increasing the volume fraction moves it into the glassy state where only localized vibrational motion survives [60]. It should be mentioned that if prepared properly, the system can form crystal even with high polydispersity, not one crystal as a whole, but with sub-regions containing different states of crystals [126]. The process by which a system entering the glassy state (solid like) from supercooled liquid state (liquid like) is called glass transition, shown by Fig. 1.1.

Temperature is another key parameter. As mentioned above, the individual particles in different systems vary in size. Foams and emulsions, bubbles or droplets

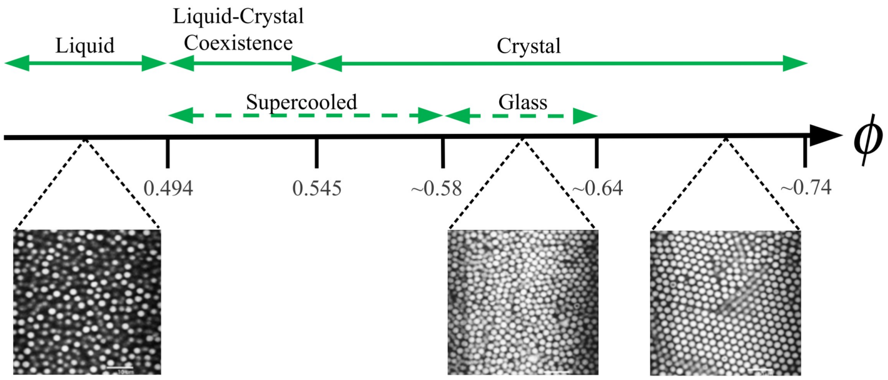

Figure 1.1: Figure 1 in [60] shows a phase diagram of hard spheres versus volume fraction, Φ. Solid (dashed) arrows indicate (non)equilibrium states. Note that the existence of the glassy state requires some polydispersity. Bottom inset images are confocal micrographs. Republished with permission of IOP Publishing, Ltd, from ”The physics of the colloidal glass transition”, Gary L. Hunter and Eric R. Weeks, 75, 6, copyright (2012) [60]; permission conveyed through Copyright Clearance Center, Inc..

dispersed in a continuous liquid phase, are usually larger than tens of microns. These sort of systems with particles that are large enough so that the Brownian motion effect can be ignored are called athermal system. Thermal fluctuations play a major role in other systems consisting of smaller particles like colloids and polymers. The glass transition mentioned above is a great example where temperature is as crucial as density [86, 127]. When the density is moderate and temperature is high, thermal fluctuation enables particles to move around to find the equilibrium state so that the system is liquid like. When the temperature is low such that the particles are mostly frozen, the system again either rearranges to form an ordered crystal where particles mainly vibrates, or becomes out of equilibrium (enters glassy state) where the system cannot sample the whole configuration space. More specifically, there are two situations where the material does not crystallize. Some materials consist of polydisperse particles and can avoid crystallization even when undercooled; alternatively, a sample can be cooled faster than nucleation can occur. In such situations, the sample is said to be a supercooled liquid. Further cooling the supercooled liquid returns a liquid-like

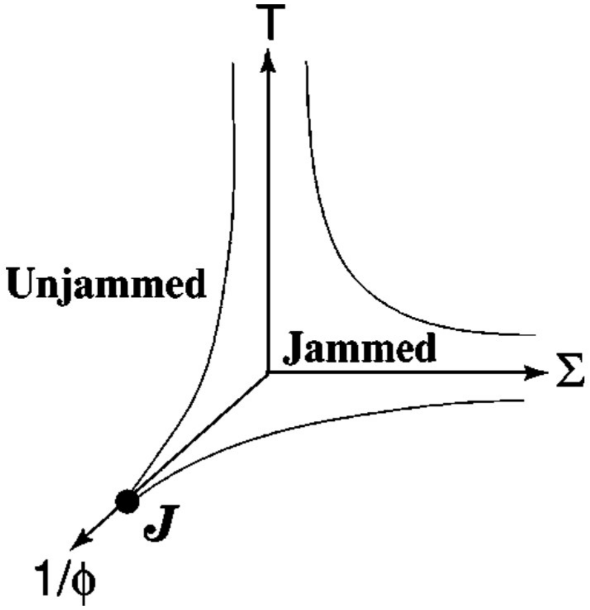

Figure 1.2: Phase diagram where control parameters are temperature, density, and applied load. The state below the curved surface is solid-like, with the projection onto the load-density plane being the jammed state and the other being glassy state. The curved plane corresponds to the regular glass transition. The transition line, or the projection of the curved plane on the density-load plane is the jamming transition. Reprinted by permission from [102], ["Jamming at zero temperature and zero applied stress: The epitome of disorder", Corey S. O'Hern, Leonardo E. Silbert, Andrea J. Liu, and Sidney R. Nagel, Phys. Rev. E 68, 011306, 2003.] COPYRIGHT (2003) by the American Physical Society.

structure but frozen microscopic dynamics, i.e. the system becomes a glass. Therefore, for a certain density, there is also a transition in terms of temperature where a system changes between liquid and glass states and the corresponding temperature is called glass transition temperature T_g.

Figure 1.1 mentioned above is a one-dimensional phase diagram of colloidal system that only considers density of a system. The glass transition is a point in Fig. 1.1. The interplay of the two parameters density and temperature can thus determine a line on a two-dimensional phase diagram separating glass and liquid which is called glass transition line. See the transition line in the $T - 1/\Phi$ plane in Fig. 1.2 below for an illustration.

The study on glass transition density and temperature is one example that people work hard to understand from the microscopic scale, for example from the micro structures. Various models and theories are proposed and debates are still ongoing [89, 127, 21]. Another example is aging in the glassy state. Theoretically, as long as the temperature is not zero, thermal fluctuation always exists and it is always possible for a system to evolve towards a more stable, lower energy state (more solid like). This evolution process is called aging [69, 113, 46, 42]. This means that the system is constantly changing with time. Consequently, the thermal history matters. How a thermal system is prepared thus has a strong effect on its properties. For example, cooling or quenching a system quickly usually results in a less stable glass compared with slowly preparing the glass [7, 37, 116]. The slowly prepared system has more time to evolve during the preparation process and thus can be more stable. This quenching rate $\dot{T}$ is therefore an important factor and one of my studies considers this situation. Since the evolution involves the rearrangements of particles (if every particle is completely frozen, i.e. at zero temperature, then the system won't evolve), many previous studies attempted to explain the phenomenon by looking at the microscopic individual particle behaviors. Athermal systems are a different story. Since no thermal effects are present, once the density is high enough so that no space is available for particles to move, the system is entirely frozen and such state is called jammed state. The entering of system into the jammed state is called jamming transition. The dynamic is completely frozen in the jammed state and people turn to apply external influence to the systems and consider the reactions.

The externally applied influence, normally stress, is the third parameter. People apply external force mainly to probe the mechanical or rheological properties of the systems, such as failure, creep, and yield of materials, shear thinning and shear thickening (see below for definition), etc. Again, many studies try to explain these macro system-wise properties and behaviors from the micro individual particle level

[123, 39, 45, 27, 32]. People working on glassy systems where aging takes effect but is not desired also apply shear to 'rejuvenate' an ageing sample [96]. See next section for more explanation. The applied force can also drive the jammed system to flow and thus unjam. Therefore, density and external force together determine the state of athermal systems and just like the glass transition line mentioned above, a jamming transition line can also be defined by the two factors. Take the three controlling parameters into account at the same time and a transition plane can be defined on the phase diagram as shown in Fig. 1.2, separating solid-like (below the plane) and liquid-like (above the plane) phases.

Figure 1.2 is believed to be universal and works for various amorphous materials mentioned above. Below the curved plane is defined as jammed or solid phase. Some people consider the projection of the solid phase onto the zero temperature plane as the jammed phase and the rest of solid region as glassy phase. They thus treat the jamming transition as a special case of glass transition while others believe the two are fundamentally different [61, 86, 75]. Many studies work on trying to investigate the relation between the two [61, 16, 75]. On the transition plane (transparent plane in Fig. 1.2), three important critical quantities are the glass transition temperature T_g, jamming transition density ϕ_j, stress that yields (unjams) the system which is called yield stress σ_y, as shown in Fig. 1.2. The mechanical, dynamical, and rheological behaviors of amorphous materials are shown to depend significantly on the distance to these critical points. For example, numerous experimental and numerical studies have found universal scaling of many quantities of the systems like shear modulus G with distance to ϕ_j, which are called critical scaling laws [35, 40, 102, 103]. Microscopic level origins behind these behaviors are still under investigation.

My two projects are on both thermal and athermal systems with simulation, in glassy state and above ϕ_j (in jamming state) respectively. External stress is applied to both systems in the form of simple shear with constant strain rates $\dot{\gamma}$. Details about the simulation are in Chapter 2. We vary the $\dot{\gamma}$, T, ρ in 3D or ϕ in 2D, $\dot{T}$ and examine their influences on the behaviors of our systems.

1.2 Yield of amorphous solid

When the system is in a liquid like state, normally called complex liquid, applying external force is generally for the purpose of testing the rheological properties of the system. Examples include investigating the flow curve, constitutive laws, dependence of viscosity on shear rate, and shear thinning, shear thickening, and shear banding, etc (see below for the definitions). We work on the other branch, where the external force is applied to glassy or jammed systems. For athermal system, as mentioned above, an external force is necessary to activate their dynamics and enable the configuration evolution. For thermal system, both external force and thermal fluctuation can drive the configuration changes. Therefore, there are both situations involving competition between the two where people need to consider questions like which one dominates and which one can be neglected, and situations involving summation of the two where people account both effects on the final response of the system like both their contribution to the stabilization (energy release) of the system [17, 18]. These differences highlight the necessity of different considerations for thermal and athermal systems. Nevertheless, the methods people use to apply the external force are similar.

Typical protocols include shearing by rotating the wall of a rheometer (Couette shear), applying pressure in given directions (indentation, pure shear, simple shear, cyclic shear, and compression), or simply using gravity such as placing the material on a tilted plane [29]. Rheometers control either the applied torque τ or the angular velocity Ω of the rotating plate. In the former case, the applied macroscopic shear stress is kept constant on a rotating cylinder and one monitors the resulting shear strain γ or strain rate $\dot{\gamma}$. Conversely, strain-controlled experiments control the strain γ or strain rate $\dot{\gamma}$ and keep track of the stress response $\sigma(\gamma)$. Examples of experiments and simulation works to name a few include [67, 22, 98, 88, 70, 109, 20].

The response to the external force also varies for different systems. Generally speaking, when a small stress is applied, the deformation of a system is mostly elastic, meaning that the configuration can return back to the initial stage, in other words, the deformation is reversible. Under larger stress, the change of configuration starts to become irreversible and is called plastic deformation. When the stress on the system is larger than a threshold value, which is termed as yield stress σ_y, the system yields. After the yield, the plastic deformation accumulates in brittle materials and the system finally fails and displays macroscopic fracture, while in ductile materials the plastic deformation mainly release the accumulated energy and stress in the system and the configuration enters a lower energy and more stable state, after which the energy and stress accumulate again and process repeats. We observe steady flow for such materials. The stress and strain curve in Fig. 1.3 illustrates such process. The starting linear part corresponds to the elastic response where the system behaves like a Hookean solid. Then a transient overshoot part occurs where the system yields. The maximum stress is defined as the static yield stress σ_{max}. This key quantity highly depends on the stability of the system and thus is highly influenced by the preparation process of the system, for example the quenching rate used to prepare the sample. Then the system either undergoes failure or enters the steady flow state where the stress fluctuates around a mean value called steady state stress σ_{ss}. This quantity is less affected by the thermal history since the memory of the initial preparation state is erased in this steady flow state. Note that not all systems under shear show the overshoot of stress.

The curve showing the dependence of σ_{ss} on the shear rate $\dot{\gamma}$ is the flow curve. A Newtonian fluid typically shows a linear relationship between σ_{ss} and $\dot{\gamma}$ and the slope

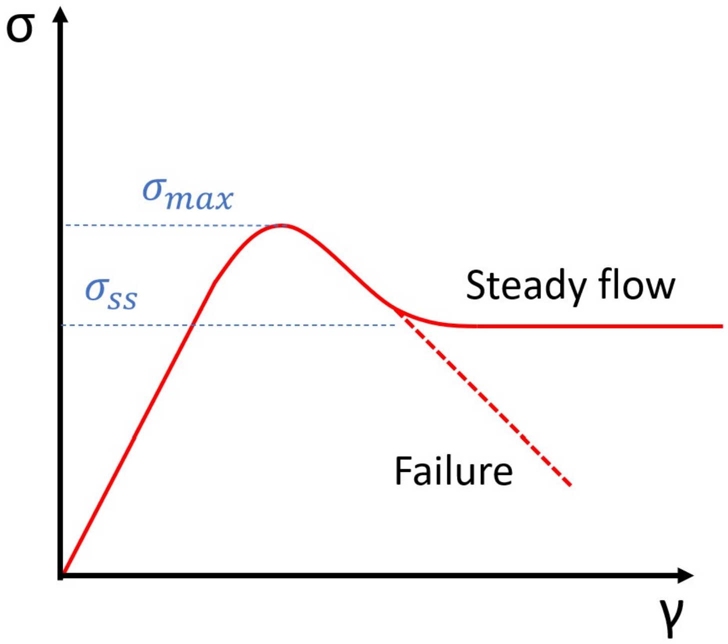

Figure 1.3: Sketch of stress and strain curve, i.e. macroscopic response of amorphous materials to external load. Failure and steady flow correspond to brittle and ductile materials respectively. The static yield stress σ_{max} and steady state stress σ_{ss} (SS strands for steady state, also the steady flow state in the sketch) are indicated.

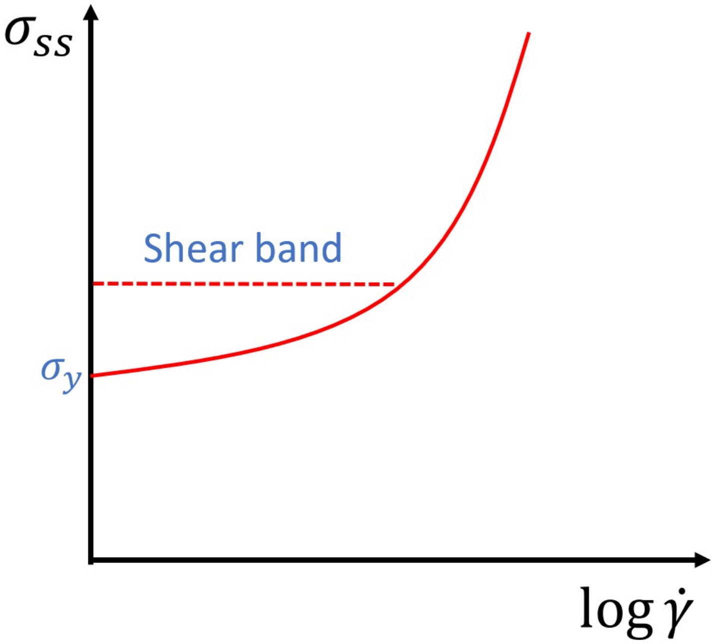

Figure 1.4: Sketch of a typical flow curve, i.e. the steady-state shear stress σ_{ss} against the shear rate. A shear band forms when a stress plateau is observed no matter the shear rate. A more general definition of shear band is region where the local response is clearly different than the bulk.

is the viscosity η. Nonlinear relation includes $\eta(\dot{\gamma})$ increasing with $\dot{\gamma}$ which is called shear thickening, and decreasing with $\dot{\gamma}$-shear thinning. Shear band forms where the σ_{ss} is a constant no matter how large $\dot{\gamma}$ is. See Fig. 1.4 for illustration. Numerous studies address these quantities from different views and perspectives [45, 108].

Looking deeper and closer at the stress and strain curve, people find that instead of a smooth curve, the detailed shape is mostly jagged with very local basins and bumps resulting from the repeated process mentioned above. Let us recall that the energy U accumulates elastically where the stress increases and then is released through plastic deformations at some threshold points where stress reaches a peak and then drops, forming a bump and basin. This process happens locally at different places among the system, forming the overall stress and strain curve. It is thus of particular importance to investigate the nature of these plastic deformations in order to better understand the macroscopic behaviors of these systems. Various methods and ideas are proposed to identify and quantify these deformations, see next section. One particularly hot topic recently is to predict the positions in a system where plastic events are highly likely to happen based on solely on the structural information of the system. These positions are called soft spots [31, 128, 30]. One of my studies also shows that simple predictions can also be made provided the local information of sizes and positions of individual particles. See chapter 3 for more results.

Once a plastic deformation happens, the released stress propagates away in certain directions [34, 81], which might be able to trigger other plastic deformation at places close to the threshold stress. Therefore, long-range interaction exists between these events and avalanches might be triggered. The scale of such nonlocal effect highly depends on the position to the jamming transition point ϕ_j. The strain rate used to shear the system and the temperature (for thermal systems) also have strong effects on the length scale of the nonlocal effect, and under certain situations avalanches spanning the whole system can be found. We also demonstrate evidence of such avalanches in one of our studies, see chapter 4 for more details.

My first project focuses on the plastic deformation of athermal system above jamming transition point ϕ_j under simple shear using simulation. See the details of our simulation in chapter 2 and results about dependence of individual particle behaviors on polydispersity (see below for more description) in Chapter 3. My second project works on the thermal system in glassy state under shear again using simulation and we look at the two key quantities σ_{max} and σ_{ss} on the stress and strain curve. We also investigate the properties of the stress drop in the steady flow state between the bump and basin. See the simulation details in chapter 2 and related results in Chapter 4 and 5.

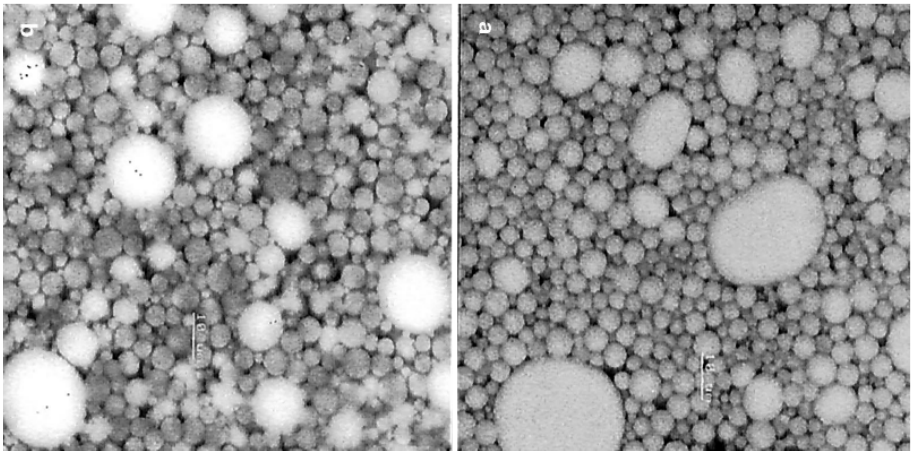

Figure 1.5: Confocal laser scanning microscopy photos of a commercial mayonnaise with/without fish oil (The two images are rotated by 90 degrees for better illustration). Various sizes of particles can be seen, showing the high polydispersity of real products. Reprinted by permission from Springer Nature Customer Service Centre GmbH: European Food Research and Technology [66], "Oxidation in fish-oil-enriched mayonnaise 1. Assessment of propyl gallate as an antioxidant by discriminant partial least squares regression analysis", Jacobsen, C., Hartvigsen, K., Lund, P. *et al*, COPYRIGHT (1999), November 1999 (doi: 10.1007/s002170050526)

1.3 Effect of polydispersity

Polydispersity means that the samples are composed of particles of different sizes. For a given sample, there is a size distribution P(R) of the particle radii. The polydispersity is quantified by $\delta = \sqrt{\langle \Delta R^2 \rangle}/\langle R \rangle$. Here $\Delta R = R - \langle R \rangle$ and the moments of R and ΔR are defined as $\langle R^n \rangle = \int R^n P(R)\, dR$ and $\langle \Delta R^n \rangle = \int \Delta R^n P(R)\, dR$. Polydispersity $\delta = 0$ means monodisperse and for the conventional bidisperse systems it is normally less than 0.2.

As mentioned in previous sections, many of amorphous materials in real life, appearing in nature and industrial applications and commercial products, in various length scales, are mixtures of various sizes of particles. For example, the cytoplasmic and nucleoplasm environment in cell usually contain various sizes of inclusions and organs [114]. Figure 1.5 also shows the microscopic structure of mayonnaise. It is obvious that various sizes of droplets are there in the mayonnaise sample, which is certainly more complicated than the single-size systems. The goal of one of my projects is to bridge between the simple model systems studied previously with low polydispersity, and the complex highly polydisperse real-world materials, by examining the role of the particle size distribution in sheared materials. In addition, in real life applications and experiments, polydispersity is in fact almost inevitable due to the manufacturing process, even if a completely monodisperse sample is demanded. For example, the monodisperse colloidal samples that many labs study normally come with a polydispersity index, indicating the quality of how monodisperse the samples are. On the other hand, in many computational studies on amorphous materials, a small polydispersity is introduced to avoid crystallization *e.g.* by using a binary size distributed system [67, 48, 81]. Although it commonly exists in numerous applications and researches, most previous studies are about model systems with no- or low-polydisperse size distributions, bidisperse system for example, where polydispersity is generally considered to play a small role and particles are treated equally and size differences are ignored. For example, many computational studies use two distinct sizes with size ratio $O(1)$ [139, 49, 135, 95, 30] and many experimental studies use nominally single component systems with intrinsic polydispersity [87, 97, 55, 110, 117, 19, 134]. These studies have led to insights such as the importance of non-affine motion in sheared disordered materials [49, 135, 117], but generally treat the amorphous system as homogeneous. However, even in this sort of model systems, evidence can be found that the small and big particles in the bidisperse system are different in structure and dynamics [90]. Moreover, a confocal microscopy study of a sheared highly polydisperse emulsion showed qualitative differences in the motion of large and small droplets [26]. The universality of polydispersity as well as these signs indicating the importance of particle size call the need to investigate its influence on the behaviors of polydisperse systems.

Indeed, polydispersity leads to interesting physics. For example, polydisperse hard spheres can phase separate into multiple crystalline phases [126]. Polydispersity can lead to new phases for active matter systems [76]. An experimental study of polydisperse colloidal glasses found that different particle sizes had different dynamics and local environments [56]. Diffusion of tracers in porous materials becomes anomalous when the porous medium is highly polydisperse [23]. Force chains in granular materials become dramatically more heterogeneous in more polydisperse systems [99, 100, 15]. The viscosity of particulate suspensions strongly depends on polydispersity [107], varying by as much as a factor of 150 for constant volume fraction of particles [24]. These studies highlight the role of the particle size distribution in leading to new physics.

In conclusion, polydispersity is important, in one sense that polydisperse systems behave differently from conventional monodisperse and bidisperse systems, in a second sense that different sizes of particles in the polydisperse system behave differently even for the conventional bidisperse system, in a third sense that previously mentioned quantities and ideas which work nicely for low polydispersity systems might not be suitable anymore for polydisperse systems, and in the final sense that in many real situations, polydispersity must be taken into account.

We work on investigating the effect of polydispersity on different properties of the amorphous system under shear, like plastic deformation quantified by $D^2_{min,i}$ and nonaffinity quantified by the individual nonaffine motion, etc. See how we generate certain size distribution in Chapter 2, more discussion on the influence of polydispersity on the calculation of these quantities and our results in Chapter 3. The work in chapter 3 has been submitted to “PHYSICAL REVIEW L”.

1.4 Isomorph theory

Recently, it was discovered that a broad class of classical condensed matter systems exhibit an approximate scale invariance[4, 5, 6, 120, 51, 121]. Upon changing a system's density, a corresponding change in temperature can be found such that the structure and dynamics of the system are unchanged, as long as they are compared in an appropriate dimensionless form. State points which are equivalent in this sense are said to be isomorphic, and the key feature of systems exhibiting so-called hidden scale invariance is the existence of isomorphic curves, or isomorphs, in the thermodynamic density temperature phase diagram. The sketch in Fig. 1.6 illustrates the idea. Take a system in the figure with density ρ_1 and temperature T_1 as the starting point. When scaled to a different density ρ_2, the isomorph theory says that a corresponding temperature T_2 can be found such that many structure and dynamical properties are the same if compared in the correct units (which are called reduced units). Tracing all such points on the phase diagram for the reference point (ρ_1, T_1) returns us the isomorph of the point (ρ_1, T_1).

The theory of isomorphs shows how they can be identified straightforwardly in computer simulations, how to appropriately scale quantities for comparison, and which quantities are expected to be isomorph invariant. Isomorphs have been identified and investigated in the equilibrium liquid state for many model systems[4, 63, 64, 13, 137]. Systems with good isomorphs include those dominated by van der Waals interactions, including molecular systems, and most metals[59], while strong directional bonds, as in hydrogen-bonding systems and network formers, generally give rise to more complex behavior and the absence of isomorphs. Water is a good example of a system without good isomorphs. The phase is not important for whether isomorphs can be found, as long as relatively-high-density condensed phases are considered. Equilibrium is also not essential that isomorphs have been studied in conditions of nonequilibrium steady state shearing[124] and aging[51, 52, 42] and zero-temperature

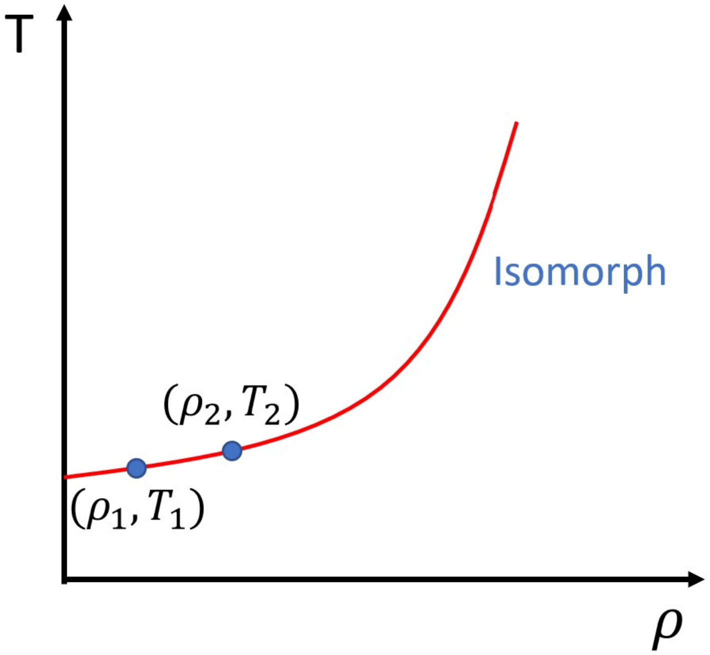

Figure 1.6: Sketch of a random isomorph on the density temperature diagram. The system at (ρ_1, T_1) and (ρ_2, T_2) are isomorphic if they have same structure and dynamics (in appropriate units). Therefore, the physics is essentially invariant along this curve.

shearing of a glass[85]. The class of systems exhibiting good isomorphs has been referred to as R-simple systems (R denoting Roskilde University where the theory was proposed). We work on one R-simple system in glassy state, the Kob-Andersen binary Lennard Jones (KABLJ) glass forming model (see chapter 2 for the definition), at finite temperature. Finite temperature glassy systems under shear have not been checked before as to whether the isomorph theory works or not.

Demonstrating the presence of good isomorphs in the glassy state has theoretical relevance not just because it permits a simplification of the phase diagram (since all points on an isomorph are invariant), but for two other reasons. First, given the existence of isomorphs, it becomes clearer what the relevant thermodynamic variables are: Pressure, while being of course extremely relevant from an experimental point of view, becomes secondary to density. Moreover, strain rates should be specified and compared in their dimensionless (reduced) form. Second, the existence of isomorphs puts a strong constraint on theories of glassy behavior. Several theories for the mechanical properties of amorphous materials have been proposed. Hidden scale invariance imposes constraints on candidate theories, since a theory which purports to be general should in particular apply to systems with hidden scale invariance and should therefore involve equations expressed in reduced-unit quantities which are explicitly isomorph invariant. This principle has been called the isomorph filter[51, 28]. In the context of theories of the glass transition, for example, a theory connecting the (reduced) relaxation time to the configurational entropy, with no other dependence on thermodynamic state, passes the isomorph filter because both quantities are isomorph invariant.

One key question is then how to express the quantities in the correct dimensionless reduced units. There are various ways to nondimensionalize quantities. People normally normalize them using either microscopic unit system or macroscopic unit system. For example, if the Lennard Jones potential between pairs of particles is applied $U_{LJ}(r) = 4\epsilon[(\frac{r}{\sigma})^{-12} - (\frac{r}{\sigma})^{-6}]$. The microscopic units are ϵ for energy and σ for length. Alternatively, if the material has temperature T and length L, then the units can be k_BT for energy and L for length. The correct units to use are macro ones [41]. Here what we do is that we essentially scale out the direct effects of changing density and temperature on structure and dynamics: If we have N particles in a volume V, then the system's (number) density is $\rho \equiv N/V$. A basic length scale l_0 is defined by interparticle spacing $\rho^{-1/3}$. If the system is in equilibrium at temperature T, then a basic timescale is defined by the time for a particle with the thermal velocity $\sqrt{k_BT/m}$ to cover a distance l_0: $t_0 = \rho^{-1/3}(k_BT/m)^{-1/2}$. In the case of a mixture, the average mass $\langle m \rangle$ should be used. Given l_0 and t_0, we can rescale space and time, making it possible, for example, to compare trajectories at different state points; the rescaling accounts for the most trivial effects of changing density and temperature. In fact, all physical quantities can be rescaled similarly, by taking appropriate combinations of l_0, t_0, and $\langle m \rangle$. For a quantity with dimensions of energy, the scale factor is just k_BT. For a pressure (or stress or elastic modulus) the scale factor is ρk_BT. We denote the rescaled reduced-unit quantities by a tilde; thus the reduced form of a particle position $\mathbf{r}$ is $\tilde{\mathbf{r}} \equiv \rho^{1/3}\mathbf{r}$, similar for other quantities. Note that these units are experimentally assessable.

Another key question is how to identify isomorphs. The scale invariance that underlies the existence of isomorphs derives ultimately from the fact that the potential energy landscape of the N-particle system changes in a somehow homogeneous way when density is changed. For example, suppose changing the density of any microscopic configuration ρ_1 by a factor λ to ρ_2 results in the potential energies being changed by a factor λ^γ for some exponent γ. This can then be compensated by increasing temperature by the same factor, meaning all Boltzmann factors will be unchanged, so the statistical probability of all microstates will be the same at the new density as for the corresponding unscaled configurations at the original density.

The method based on this idea is called the direct isomorph check (DIC). The temperature factor can be derived by requiring the potential energy at the scaled density scales accordingly. Details about how to perform the DIC are in chapter 5. It follows that all statistical measures of structure will be invariant when expressed in terms of the reduced coordinates $\tilde{\mathbf{r}}$. It can also be shown [120] that the equation of motion is also the same for both states when expressed in reduced units and therefore that all dynamical quantities are also invariant in reduced units. There are also several other methods based on other ideas that are able to generate isomorphs. Since we are interested in glassy system at finite temperature, i.e. the system is in nonequilibrium state, other factors like thermal history (aging) must be considered, making the identification of isomorphs more subtle. Extra carefulness is needed about which method to use to generate the isomorph. Details about how the different methods work and how to perform them in simulation as well as their performance (quality of isomorph, in other words the quality of the invariance) can be found in chapter 5. It should be noted that there are also ways to identify isomorphs in experiments. For any R simple system, isomorphs may be obtained by tracing density and temperature points with constant reduced viscosity or diffusion constant. For highly viscous liquids the isomorphs are basically the lines of constant relaxation time, the so-called isochrones.

My study on isomorphs involves three parts. For the first part, we check the quality of isomorph theory for the KABLJ glass at two different starting temperatures under shear with different strain rates $\dot{\gamma}$. Here we don't bother too much about which methods to use to generate the isomorph. We choose the most common and classic one (see chapter 4) and only test a small density span $\rho \in [1.265, 1.384]$ and $[1.324, 1.448]$ for the two starting $T = 0.1, 0.55$. We focus on the steady state and verify the invariance of the structure and particle dynamics, and quantities related to the steady state stress σ_{ss} mentioned in previous section. The other two parts involve a much larger density span $\rho \in [1.183, 2.789]$. The work has been published on “PHYSICAL REVIEW E” [67]. For the second part, we test 5 methods (see chapter 5 for details) to generate isomorph to compare their performance for such a large density span. We evaluate them by checking the quality of the invariance of the $\sigma_f = \langle \sigma_{ss} \rangle$, the mean stress in the steady flow state. For the third part, we investigate both the σ_f at the steady state and σ_{max} at the transient overshot part of the stress and strain curve. Since σ_{max} is the stress at the peak, we call it peak stress and label it as σ_p. As mentioned before, the peak stress sensitively depends on the thermal history of the system. Therefore, we also vary the cooling rate we use to obtain the starting glassy configuration. Results and discussion are in chapter 5. The work in chapter 5 is planned to be submitted to “PHYSICAL REVIEW E”.

Chapter 2

Simulation method

For the first project about polydispersity, I work with programming language IDL. For the second project about isomorph, I use Python. Here, I'd like to comment on simulation as a tool in soft matter research area. Insights of the new understandings of amorphous solids have often originated from computer simulations. People use simple models to simulate the systems being studied and ignore factors and effects that are not important under the certain situations that people care about. For example, when studying the packing of amorphous solids, a classic model to use is the hard sphere model where only a repulsive force is considered when a pair of particles are in contact or within a certain amount of distance [91, 131, 140]. Other factors such as possible attraction between particles and slight deformation of particles are neglected because they are assumed to play a small role in the packing of the system. Indeed many significant results have been found and consistency has been proved with experimental studies [38, 68, 122, 2]. Ultimately experiments are still needed but there are many times that the experiments are difficult to perform and time consuming. Simulation is a good alternative here.

Most of the time people mainly consider pairwise interactions in the system. Usually the first step is to choose the potential energy, since force can be derived from the potential energy and thus the dynamics of the system can then be determined. However, sometimes people can also directly choose the needed force and skip the potential step. The next step is to derive the force and then solve the equation of motion for each single particles in the system. Then the dynamics of the whole system can be calculated. Common pair potential includes Lennard-Jones (LJ), the purely repulsive inverse-power law (IPL), the Yukawa 'screened Coulomb' pair potential, the Morse pair potential, the hard sphere potential, etc. The final step normally is to investigate the properties of interest based on each particle's position and velocity information.

The simulation method that involves numerically solving the equations of motion, which if are the Newton's equations of motion, is called "molecular dynamics" (MD). It traces the trajectories for every particle. Newtonian dynamics conserves the energy E (when no damping effects such as viscous force are considered). When considered at constant volume V and particle number N, this is referred to as NVE dynamics. NVT simulation where temperature is conserved and NVU simulation where constant potential energy is applied (tracing out a geodesic curve on the constant-potential-energy hypersurface) and NPT simulation with constant pressure are also frequently applied depending on the needs and systems under investigation. All these simulation methods are deterministic that the system's evolution is uniquely determined once the simulation is started. Brownian or Langevin stochastic dynamics on the other hand work differently. Usually they return the similar results and statistics. People choose from these methods based on the specific properties the systems have. Other simulation strategies are also frequently applied but my current interests are on MD simulation.

2.1 Durian bubble model and Runge-Kutta method

We use the Durian bubble model to simulate soft granular particles in 2D, where we only consider a harmonic repulsive force when two particles are in contact and a viscous force when two particles move by each other with different velocities [40, 57].

$$\vec{F}_{ij}^{repulsive} = F_0[\frac{1}{|\vec{r}_i - \vec{r}_j|} - \frac{1}{|R_i + R_j|}]\vec{r}_{ij} \tag{2.1}$$

$$\vec{F}_{ij}^{viscous} = b(\vec{v}_i - \vec{v}_j) \tag{2.2}$$

Here, $\vec{F}_{ij}^{repulsive}$ is the repulsive force from j on i and same for $\vec{F}_{ij}^{viscous}$. F_0 and b are constants indicating the relative strength of the two forces. We use 1 for both of them. i, j indicate particles i and j. $\vec{r}_i$, R_i, and $\vec{v}_i$ are the displacement vector (where a particle is), the radii, and the velocity vector of particle i. Same for j. $\vec{r}_{ij}$ is the direction vector pointing from particle j to i. Only when the distance between two particles is smaller than the sum of their radius (the two in contact) is the repulsive force between them nonzero. It should be noted that this repulsive force models interaction between soft particles, since $\vec{r}_{ij}$ must be smaller than $R_i + R_j$ for the force to be nonzero, meaning that particles must deform. The term $R_i + R_j$ also indicates that larger particles are softer. Note here that the Durian bubble model is also harmonic.

With the forces given, particle equation of motion can be determined and solved to obtain the position and velocity of each particle at each time step. We use the Runge-Kutta method to numerically solve the equation of motion [112]. In our system, the inertial effects are negligible and the net force on each bubble sums to zero. The equation of motion for particle i by summing over neighbors in touch j then is

$$\vec{v}_i = 1/N_i \sum_j (\vec{F}_{ij}^{repulsive}/b + \vec{v}_j) \tag{2.3}$$

Here N_i is the number of j particles for i. We then calculate $\vec{r_{ij}}$ and get the neighbor list j for all particles in the system. Below is an example showing how we perform the Runge-Kutta method.

The calculation process is the following to obtain the velocity of particle i at time $t_0 + dt$:

$$\vec{v_i} = 1/N_i(t_0) \sum_j (\vec{F}_{ij}^{repulsive}(t_0, r_i(t_0), r_j(t_0)) + \vec{v_j}(t_0)),\ \vec{v_i}(t = t_0) = \vec{v_0} \tag{2.4}$$

$$k_{1,i} = 1/N_i(t_0) \sum_j (\vec{F}_{ij}^{repulsive}(t_0, r_i(t_0), r_j(t_0)) + \vec{v_j}(t_0)) \tag{2.5}$$

$$k_{2,i} = 1/N_i(t_0 + dt/2) \sum_j (\vec{F}_{ij}^{repulsive}(t_0 + dt/2, r_i(t_0) + k_{1,i}dt/2, r_j(t_0) + k_{1,j}dt/2) + k_{1,j}) \tag{2.6}$$

$$k_{3,i} = 1/N_i(t_0 + dt/2) \sum_j (\vec{F}_{ij}^{repulsive}(t_0 + dt/2, r_i(t_0) + k_{2,i}dt/2, r_j(t_0) + k_{2,j}dt/2) + k_{2,j}) \tag{2.7}$$

$$k_{4,i} = 1/N_i(t_0 + dt) \sum_j (\vec{F}_{ij}^{repulsive}(t_0 + dt, r_i(t_0) + k_{3,i}dt, r_j(t_0) + k_{3,j}dt) + k_{3,j}) \tag{2.8}$$

$$\vec{v_i}(t = t_1) = \frac{1}{6}dt(k_1 + 2k_2 + 2k_3 + k_4),\ t_1 = t_0 + dt \tag{2.9}$$

$$r_i(t = t_1) = r_i(t = t_0) + \vec{v_i}(t = t_1)dt \tag{2.10}$$

Here j indicates the neighbors of i in contact and we omit b since $b = 1$. The above calculations are done for all particles and repeated so that we are able to obtain the tracking array of the system with the positions and velocities of every single particles at each time step. Then it is just a matter that how often we need to save these information. dt can be tuned to adjust how accurate the calculation is. And each time the neighbor list needs to be updated to acquire the correct forces. For our purpose, we choose a relatively large $dt = 2$ that is able to return us consistent results with a small dt like $dt = 0.1$ and a reasonable flow movie of the system under shear.

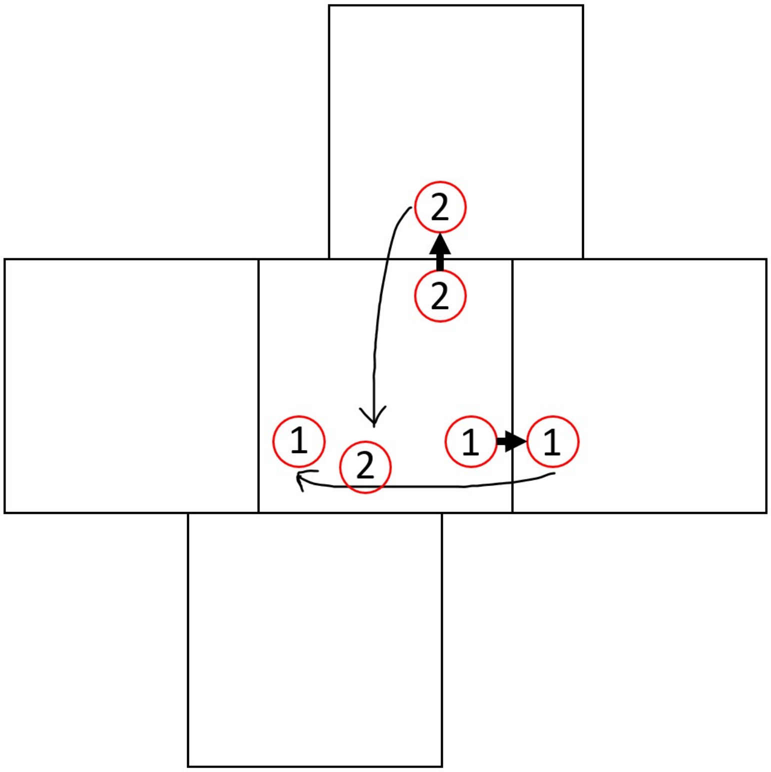

Figure 2.1: An illustration of Lees-Edwards boundary conditions. Two motions are shown: particle 1 crosses the y boundary, it appears at the other side of the simulation box with same x, y position; particle 2 crosses the y boundary and appears with the same y position but a shifted x position. The amount of the shift is treated as the applied shear strain times the box length in y direction.

The Runge-Kutta method is generally good for solving most differential equations. Once the equations are determined, the above steps can be easily performed. Thus, it is of great use to understand how the method works. Other forces and interactions can be easily added into the model to simulate other situations.

2.2 Lees-Edwards boundary conditions

As mentioned in previous sections, we work on shearing the amorphous system. In our investigation using the Durian bubble model, we achieve it by applying the Lees-

Edwards Boundary condition, which is called boundary driven flow. The sketch in Fig. 2.1 illustrate the idea. In the x direction, the normal periodic boundary condition is applied, i.e. when a particle moves outside of the simulation box by crossing the y boundaries, it appears at the other side of the simulation box with the same y position and the x position in the fake simulation box. In calculation it is the following

$$x \to x \mod l_x,\ y = y \tag{2.11}$$

Here x is the x position and l_x is the box's x length. $I \mod J$ is equal to the remainder when I is divided by J. In the y direction, the Lees-Edwards boundary condition is applied, i.e. when a particle crosses the x boundaries, it appears at the other side of the simulation box with the y position in the fake simulation box and the x position subtracted by the amount of shear. In calculation it is the following

$$x \to x \pm dx,\ y = y \mod l_y \tag{2.12}$$

Here dx is the amount the top boundary of the box is sheared, i.e. the strain γ times box y length l_y. $\pm$ correspond to crossing the bottom and top boundaries and indicate that we apply opposite shear at the two boundaries.

This Lees-Edwards boundary condition together with the previous section are able to achieve shearing the system uniformly with simple shear, i.e. the applied bulk strain is constant all over the system. At the first time step, the strain is 0. Then the positions and velocities are calculated and updated for the second time step. At the second time step, the strain becomes $\delta\gamma$. Here $\delta\gamma$ divided by the time step dt is the strain rate, one of the controlling parameters in our system, which indicates how fast we shear the system. Then the positions and velocities are updated again. Now, the particles outside of the simulation box need to be moved back to the box with new positions after applying the boundary conditions. The process is repeated and a steady shear can be achieved.

It should be noted that carefulness is needed for the velocities of particles crossing the top and bottom boundaries. The velocities are the same if crossing the left and right boundaries. However, when crossing the top and bottom ones, the direction of the velocity of the boundary-crossing particle is opposite in the real box and fake box in our strain profile. In our system the top half and bottom half are sheared in opposite directions. Therefore, the Lees-Edwards boundary condition also needs to be applied to the velocities in x direction.

It should also be pointed out that that the neighbor calculation for particles near boundaries also requires to consider the Lees-Edwards boundary condition. Figure 2.2 shows one example. The red particle is the reference center particle. Green ones are its neighbors. The one far away, touching the bottom boundary, is actually also touching the top boundary in the fake box. Therefore, the y distance between it and the red one is small. In our simulation box, the distance between two particles can never exceed $l_x/2$ in x direction and $l_y/2$ in y direction.

Another key process in our simulation is to generate the polydisperse radius for each particle. The random number generation method is used. See the book "Numerical Recipes" [111] for more information. The idea is very straightforward. The first step is to generate n random numbers following uniform distribution between 0 and 1, meaning that it is equally likely to get any value between 0 and 1. Here we just use the function **randomu** that comes with the IDL language. The next step is to derive the transformation equation to translate each uniform distributed number to the needed distribution. Assume x follows the uniform distribution between 0 and 1: $p(x)dx = dx$, $0 < x < 1$. Here $p(x)$ is the probability of getting x and is normalized so that the integration of it between 0 and 1 is 1. Suppose the distribution that we need is y and we can set y as a function of x. $p(y)$ then follows by the fundamental transformation law of probabilities $|p(y)dy| = |p(x)dx|$. To obtain an exponential

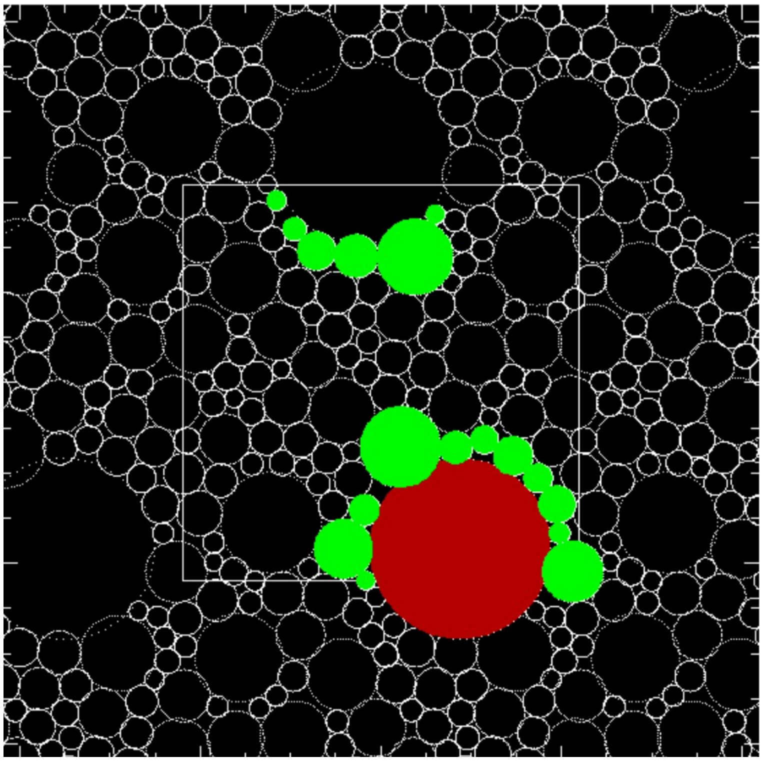

Figure 2.2: An example of the neighbor calculation. The red particle is the center one and the green particles are its neighbors.

size distribution for y, assume $y(x) = -\ln(x)$, then $p(y)dy = |\frac{dx}{dy}|dy = e^{-y}dy$. Here, we just need to solve for $x(y)$ with given needed $p(y)$ and then calculate the inverse function of $x(y)$ so that the transformation from x to y is determined. The idea to obtain other distributions is similar. Check "Numerical Recipe"[111] for methods to get other distributions such as Gaussian, Gamma, Poisson, and binomial, etc.

With this method, we are able to generate different size distributions such as exponential size distribution, gaussian, uniform, power law, etc. We mainly focus on the exponential size distribution, see chapter 3. Other ones are also tested, see chapter 4.

2.3 RUMD

RUMD is a high-performance molecular dynamics simulation free open source software package optimized for NVIDIA's graphics cards developed by research group "Glass and Time" at the Department of Sciences in Roskilde University in Denmark. Another similar package that is widely used is called "LAMMPS". RUMD uses graphics processing units(GPUs) for its calculation, which is getting more and more popular nowadays. The details about how to install RUMD, how it is developed, and GPU coding etc can be found at http://rumd.org. Here, I'll describe some key features of RUMD and what can be achieved with RUMD as well as what I did with RUMD as an example to illustrate how to perform a MD simulation with it.

As mentioned above, a pairwise potential is required. RUMD can achieve Lennard-Jones, Gaussian core, inverse power law, exponential, Yukawa, etc and it is easy to implement new pair potentials. It can run all ensembles aforementioned, NVT, NVE, NVU, and NPT. For example, it can perform constant NVT integration to update positions and velocities each timestep for each individual particles in the group using a Nosé/Hoover temperature thermostat. This creates a system trajectory consistent with the canonical ensemble. Shear simulation is also possible using Lees-Edwards boundary conditions and the SLLOD equations of motion. It also comes with many analysis tools to calculate some classic structure and dynamics properties of the system. See chapter 5 and 6 for some analysis I did with RUMD.

How to start a RUMD simulation and more advanced usages can be found again at http://rumd.org. I use RUMD to simulate KABLJ system with 8000 big particles and 2000 small ones interacting with Lennard Jones potential [71]. The microscopic units of energy and length scale (see previous chapter) for big-big (AA), big-small (AB), small-small (BB) interactions are separately chosen as $\epsilon_{AA} = 1$, $\sigma_{AA} = 1$, $\epsilon_{AB} = 1.5$, $\sigma_{AB} = 0.8$, $\epsilon_{BB} = 0.5$, $\sigma_{BB} = 0.88$ in Lennard Jones units where ϵ is for energy and σ is for length. I first equilibrate the configuration at $T = 1$ using NVT

simulation and then cool the system to $T = 0.3$ with different cooling rate $\dot{T}$ again with NVT simulation. Then the glassy system is sheared with planar Couette flow using SLLOD integrator and Lees-Edward boundary conditions (see previous section).

The idea of creating shear in the simulation is similar to what I do with the Durian bubble model. Here, the SLLOD equations of motion below are applied together with the Lees-Edwards boundary conditions.

$$\begin{aligned} &\dot{x}_i = P_{xi}/m + \dot{\gamma} y_i, \\ &\dot{y}_i = P_{yi}/m, \\ &\dot{z}_i = P_{zi}/m, \\ &\dot{P}_{xi} = F_{xi} - \dot{\gamma} P_{yi}, \\ &\dot{P}_{yi} = F_{yi}, \\ &\dot{P}_{zi} = F_{zi} \end{aligned} \tag{2.13}$$

They were originally proposed by Hoover and Ladd [58, 77] and then proven to be equivalent to Newton's equations of motion for shear flow by Evans and Morriss [47]. Daivis and Todd [33] later showed that they can generate the desired velocity gradient and the correct production of work by stresses for all forms of homogeneous flow. For SLLOD equations of motion, the Lees-Edwards boundary conditions are not required for the velocities. As with Durian bubble model, here I also shear the system with fixed strain rate. The reason is that we achieve the shear in both methods by deforming the simulation box in a sense of simple shear with fixed rate. Therefore, each point in the simulation box can be thought of as having a "streaming" velocity which scales linearly with the positions perpendicular to the shear direction, y for example if shear in x.

Some final comments on both methods, coding the Durian bubble model and shearing ourselves and applying RUMD package to achieve the MD simulation. The pros of the former are that I know every detail of our simulation and I learned how to use the Runge-Kutta method to solve simple differential equations. I can easily modify our codes and adapt to other situations that need more flexibility and degrees of freedom. For example, we can easily add terms in the equation of motions and simulate clogging of particles falling under gravity in a hopper [57]. The pros of using packages like RUMD and LAMMPS are that it is easy for a beginner to start a MD simulation quickly from knowing nothing about MD simulation. The details of solving equations and saving results are all in the package. Users just need to understand the user manual about the meaning of each functions and related parameters. The development of these packages is already very mature and many information of the system can be easily obtained by choosing correct functions and correct keywords in the functions. For example, the calculation of stress and potential energy and pressure and other quantities are already included in the packages. However, in our homecoded simulations, we need to add them one by one ourselves if we need.

Chapter 3

Effects of Polydispersity on 2D dense soft particles under steady shear

We examine the particle-scale motion of highly polydisperse dense 2D granular systems under shear using simulation. The largest particles are as much as ten times the size of the smallest in our system. Shear produces a mean affine flow, and nonaffine deviations. We calculate the deviation to quantify the nonaffine behaviors of both individual and local groups of particles. Strikingly different behaviors from the more commonly studied amorphous systems with low polydispersity are found. We show that all quantities under investigation significantly depend on the particle size. The large and small particles' behaviors are qualitatively different. In contrast to low polydisperse systems, the large particles in our simulations give rise to a new flow pattern for the smaller particles, which we demonstrate could be one of the origins of the local nonaffine and plastic behaviors we find. These findings are qualitatively different than previously found in low polydisperse systems. Moreover, we quantify the local fields of individual and group nonaffine motions around certain sizes of particles and check the dependence on particle size in different size distributions including a bidisperse system. We show that on one hand, both fields depend on the size of particles and looks qualitatively different between big and small particles, enabling us to define “big” and “small” effectively in the particular system under study. Even a bidisperse sample exhibits noticeable differences between the two sizes of particles. In most previous studies on bidisperse system, the two sizes are treated to be the same for granted. Our results show that new physics is very likely to be learned if size dependence is considered. On the other hand, the properties of the fields also vary between different size distributions, especially different between bidisperse and highly polydisperse systems. We characterize the crossover in the two nonaffine behaviors from the low- to high-polydispersity regime.

3.1 Introduction

In this chapter, we use the Durian bubble model [40] to simulate several highly polydisperse 2D granular systems with different size distributions and one bidisperse system under steady shear. We find that the particle-level behaviors of our polydisperse systems are qualitatively different than the previously studied low polydisperse system. Specifically, we show that the large particles are more likely to follow the bulk flow, even in bidisperse system. An examination of local averaged particle behaviors around particles with various sizes (in a coshearing reference frame) show that the presence of the large particles can dramatically change the motions of nearby particles. We also find that the pattern of such averaged local behaviors are completely opposite for small and large particles and the pattern changes gradually with increasing particle size. By comparing systems with different size distributions, we find that the abovementioned results of the flow pattern are generally true and the magnitude increases with the size span or the size ratio between the largest and smallest particles. High-polydisperse systems also show novel plastic behaviors in the local scale and position dependence (relative to certain sizes of particles) than bidisperse system. These findings prove the significant effects brought by the large polydispersity and emphasized the needs for future theoretical studies to consider the size of particles in amorphous systems. For instance, our results show that the largest particles strongly influence nearby particles to rearrange, suggesting that previously studied soft spots (e.g. [95, 30]) will be different in character – and easier to identify – in highly polydisperse materials. Our results also confirm the importance of simulating polydisperse systems to the glass physics community. For example, recently the "Swap Monte Carlo" method used to probe increasingly low temperatures of the glassy systems crucially relies on having sufficiently broad polydispersity so that Monte Carlo swaps of particle radii help equilibrate the system [101].

3.2 Simulation

Here we provide more details of our simulation. We use the Durian bubble model, where particles feel a repulsive contact force and a viscous force from neighboring particles moving at different velocities. No inertial effect is considered. Detailed definition can be found in chapter 2. We consider a variety of exponential size distributions $P(R) \sim \exp(-R/\lambda)$ with R being the radius. The distributions are over $R_{\min} \leq R \leq R_{\max} = \alpha R_{\min}$ with α ranging from 2 to 10 which controls the breadth of the distribution. The decay constant λ is set to $R_{\min}$. We take $\langle R \rangle$ as our unit of length; equivalently we adjust $R_{\min}$ so that $\langle R \rangle = 1$. An example of the probability distribution function of the $\alpha = 10$ size distribution is shown in Fig. 3.1. To nondimensionalize time we use the microscopic relaxation time, which is set by the time scale characterizing two individual particles of radius $\langle R \rangle$ pushing apart, based on the inter-particle spring constant and viscous damping forces [40]. We use number

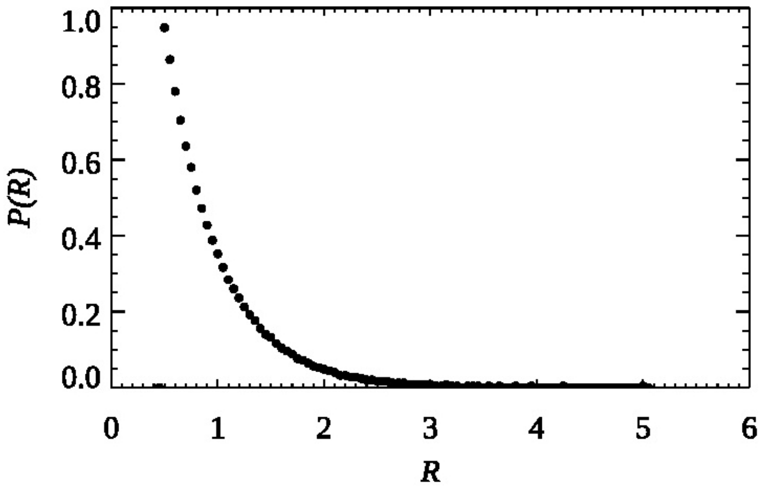

Figure 3.1: The probability distribution function of the $\alpha = 10$ size distribution. The mean radius $\langle R \rangle = 1$.

ratio 50 : 50 and size ratio 1/1.4 for the bidisperse system. These distributions can be characterized by their polydispersity, defined as the standard deviation of $P(R)$ divided by $\langle R \rangle$. The polydispersity ranges from 0.20 to 0.50 for the exponentially decaying $P(R)$ we consider, and is 0.17 for the bidisperse sample.

These systems are sheared in square boxes with length L using Lees-Edwards boundary conditions. We keep the quantity $\frac{L}{\langle R \rangle} = 100$ constant and guarantee that L is at least 20 times larger than the R_{max} for all systems. The area fraction ϕ is 0.93, which is well above the jamming transition point ranging between 0.841 to 0.859 for our systems so that our systems are all well jammed withour shear. Our nondimensional strain rate is $\dot{\gamma} = 10^{-4}$, chosen to be in a rate-independent regime [40, 104, 81] (see next paragraph for the meaning of rate-independent). We simulate the shear at least up to strain $\gamma = 10$ to ensure enough statistics; an initial transient response for $\gamma < 0.2$ is discarded before analysis. We define steady state by investigating the evolution of two quantities, the averaged nonaffine motion squared and D^2_{min} of the whole system (see the sections below for definition). We find that the two quantities enter a steady state after around $\gamma = 0.1$. We use data $\gamma > 0.2$. Other simulation details can be found in Ref. [57]. We will focus most of our discussion and

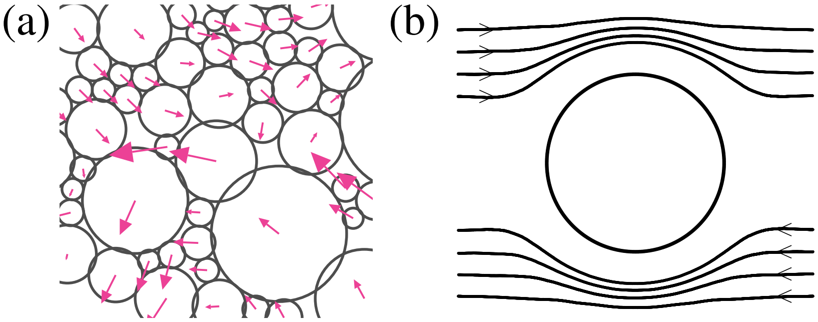

Figure 3.2: (Color online). Panel (a) shows an example of the exponential size distribution system with the particle size ratio $R_{\mathrm{max}}/R_{\mathrm{min}} = \alpha = 10$. Pink arrows indicate the motions of particles for a strain interval of 0.005. The sketch on the right demonstrates the flow pattern around large reference particles under the applied shear strain.

comparison on the polydisperse system with $\alpha = 10$ that contains 2500 particles and the bidisperse system with 3098 particles unless otherwise clarified. A snapshot of the $\alpha = 10$ system under shear is shown in Fig. 3.2(a).

It should be noted here that we choose the number of particles for each system to satisfy that the nondimensional simulation box length $L/\langle R\rangle$ is a constant for all size distributions in order to make proper comparisons between different systems. Our examination on the number of particles shows that the dynamical properties of the system are very sensitive to the system size. We define an effective diffusion constant D as the slope of the linear fitting of the mean square displacement to the lag time Δt. The dependence of D on $L/\langle R\rangle$ is qualitatively consistent with what Lemaître *et al.* found in a finite size effect check for a two-dimensional Lennard-Jones glass at $T = 0$, sheared at finite strain rates $\dot{\gamma}$ [81]. The reason for using a constant nondimensional strain rate is similar to using constant $L/\langle R\rangle$. Our check on the dependence of D on the strain rate also qualitatively agrees with Lemaître et al [81], see Fig. 4 and 5 in their paper. For a certain strain rate, D increases with increasing system size and the increasing rate increases with decreasing strain rate. For a certain system size, D increases with decreasing strain rate and the increasing rate increases with increasing system size. To avoid the boundary effect where a big particle can interact with itself, we must use a large system size to achieve a large simulation box. In accordance, we use a rather small strain rate so that the quantity D/L is in the plateau regime as in their Fig. 5, which is considered to be rate-independent. We then fix the two nondimensionalized quantities $L/\langle R\rangle$ and $\dot{\gamma}\langle R\rangle$ to achieve the same effective dynamics among all systems. Our hypothesis is that our main results (shown below) would not change if larger system size and slower strain rate are used.

3.3 Nonaffine motion

To examine rearrangements and other behaviors of particles, we choose a lag time Δt to satisfy a strain interval $\Delta\gamma = 0.005$. Smaller $\Delta\gamma$ are also checked and does not change our story. Larger choice of $\Delta\gamma$ would lead to increasing possibility of investigating the accumulation effect of multiple rearrangements. In order to characterize the behavior of individual particle, we define the affine motion $\Delta\vec{r}_{A,i}$ for particle i as $\Delta\vec{r}_{A,i} = \Delta\gamma\, y_i \cdot \hat{x}$, where y_i is the position of particle i in the gradient direction and $\hat{x}$ is the velocity direction. All particles in the system would follow this imposed affine motion if no particle rearrangement occurs. Local rearrangements on the other hand cause deviations. As shown in Fig. 3.2(a), although in general particles follow the sketch, deviations such as motions in the gradient direction are obvious. We define such deviation as the nonaffine motion $\Delta\vec{r}_{NA,i} = \Delta\vec{r}_{real,i} - \Delta\vec{r}_{A,i}$, where $\Delta\vec{r}_{real,i}$ is the real motion of particle i. We note that $\Delta\vec{r}_{NA,i}$ only describes the behavior of individual particles and does not involve neighbors of particles defined in the next section. Note that the magnitude $|\Delta\vec{r}_{NA,i}|$ can also be used to describe an effective mobility of individual particles. Nonaffine motion quantifies the nonaffinity of particles but

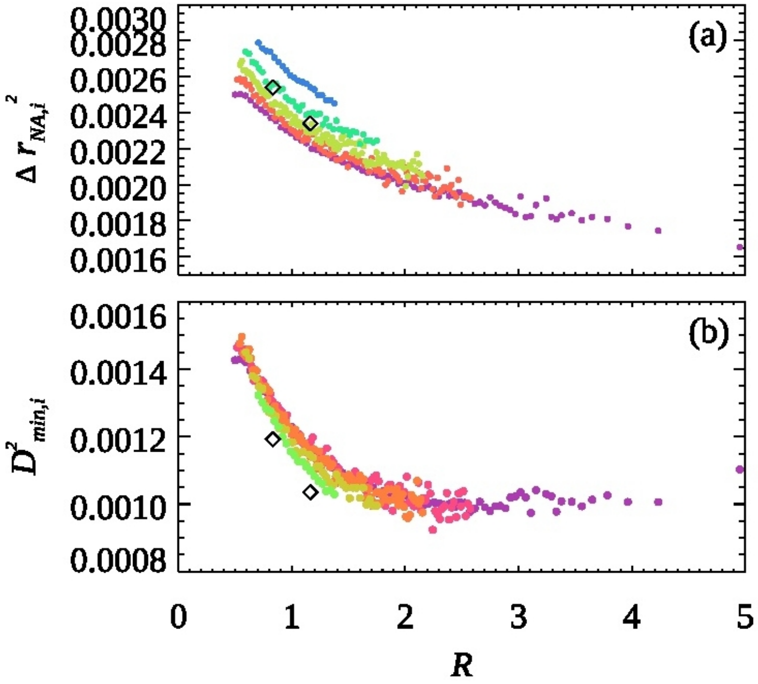

Figure 3.3: Averaged normalized $\Delta\vec{r}^2_{NA,i}$ (a), $D^2_{min,i}$ (b) versus the size R for systems with different size distributions. Data shown with span in x axis from large to small corresponds to exponential size distribution with $\alpha = 10, 5, 4, 3, 2$ (purple to blue legends), and finally bidisperse indicated by diamonds

not the plastic deformations of them. Here plastic means irreversible. A nonaffine motion can be either reversible or irreversible so that it is not necessarily plastic. To determine whether a nonaffine motion is plastic or not, a reverse shear back to the original position is required and is beyond the scope of our study here. Nonetheless, it can still provide useful information about how individual particles behave locally. We apply another quantity to investigate the plastic deformations in the system, see the next section.

We first check how the nonaffine motion depend on the sizes of particles in the systems, as shown in Fig. 3.3(a). We find that on average $\Delta\vec{r}^2_{\mathrm{NA,i}}$ decreases as particle radius R increases for all systems, including the bidisperse system; this agrees qualitatively with previous observations in polydisperse emulsions under cyclic shear [26]. Therefore, large particles are more likely to follow the affine shear flow, whereas small particles will have more nonaffine motions, or shear-induced diffusivity. A simple

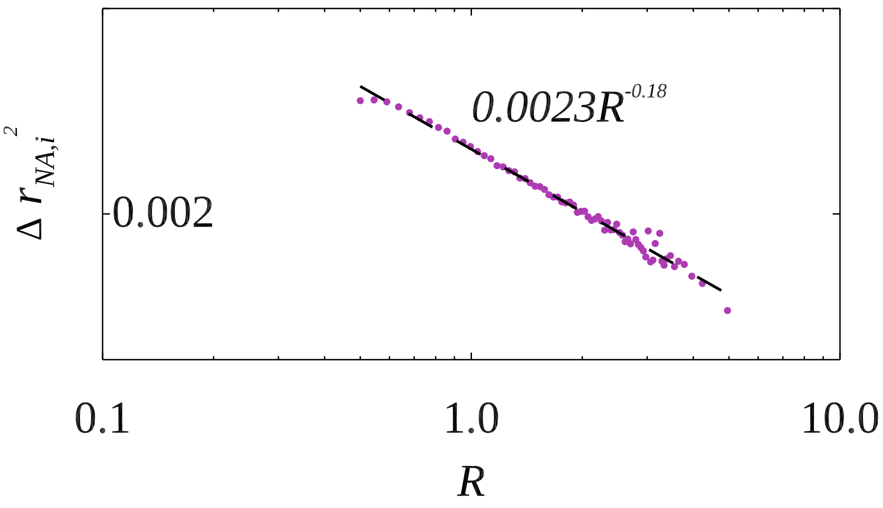

Figure 3.4: The power law fitting $\Delta\vec{r}^2_{\mathrm{NA,i}} \sim R^{\beta}$ with $\beta = -0.18$ for the $\alpha = 10$ system. The figure is in log-log axis and the black dashed line is the fit.

explanation is that large particles have more neighbors than small ones. The motions of these neighbors on average cancel with each other, which results in the larger particles having smaller magnitude of $\Delta\vec{r}_{\mathrm{NA,i}}$. Equivalently, moving a large particle non-affinely requires more neighboring particles to also move non-affinely to make room, which is harder to do. The data with the broadest span in R in Fig. 3.3(a) are well fit by $\Delta\vec{r}^2_{\mathrm{NA,i}} \sim R^{\beta}$ with $\beta = -0.18$ as shown in Fig. 3.4, although the data do not span a big enough range to conclusively decide that this is power law behavior. The limitation of the breadth of the size distribution for the power law fit is difficult to improve. Adding one order of magnitude of fitting range would require a size ratio of 100, which needs extremely large system size. Note that the bidisperse results are also consistent with those of the polydisperse systems, showing clear different $\Delta\vec{r}^2_{\mathrm{NA,i}}$ values for small and large particles.

The $\alpha = 2$ system seems to deviate much from the rest. The reason behind the deviation is not clear yet. One possible reason is that the system is more crystalline, *i.e.* hexagonally ordered [25]. The meaning of the power law behavior, if true, is also not clear and needs further investigation.

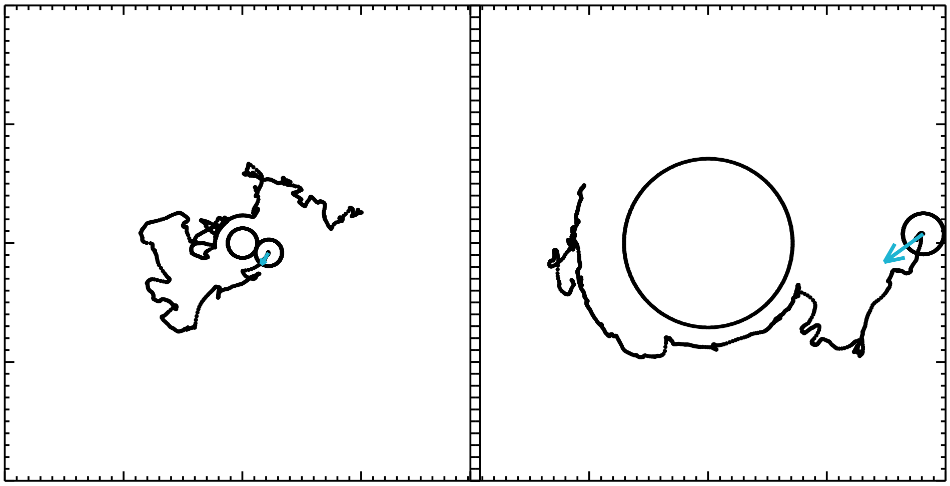

Figure 3.5: (Color online). Example of the specific detouring movement in the co-shearing reference frame around a large particle (right panel) in the $\alpha = 10$ system. Cyan arrows indicate the initial velocities here. A comparison with a small particle case is provided in the left panel, showing no such detouring movement.

These results reveal the following microscopic picture of motion near the large particles. Large particles are "strong" and have less nonaffine motion; they are more likely to follow the affine imposed shear flow. In the reference frame co-moving with the affine velocity of a large particle, this relative immobility causes the "weaker" small particles to detour around the larger particles, as sketched in Fig.3.2(b). Indeed, it is this detour motion that gives the smaller particles their larger average $\Delta\vec{r}^{2}_{\rm NA,i}$ seen in Fig. 3.3(a). Examining the trajectories of individual particles reveals motions that qualitatively match the sketch of Fig. 3.2(b), as shown in Fig. 3.5.

To better understand how large particles perturb the flow we need to calculate the average non-affine flow field around particles of different sizes. With the center of reference particle being the origin, we divide the local area around reference particles into bins of (x, y). We then average the non-affine motion $\langle\Delta\vec{r}_{{\rm NA},j}\rangle$ of all particles j at a specific (x, y) bin relative to a reference particle i. We then average that field over all reference particles i with radii R_r in a specific range to get better statistics yielding $\langle\Delta\vec{r}_{\rm NA}\rangle(x, y)$. In Fig. 3.6 we show this average field for particles with $2.0 \leq R_r \leq 2.8$.

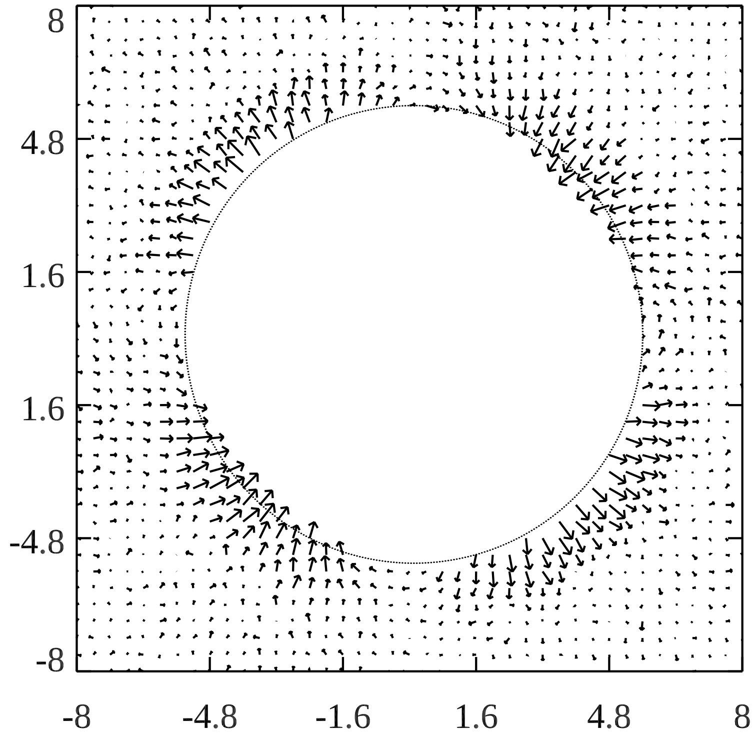

Figure 3.6: $\Delta\vec{r}_{NA,i}$ vector field for particles with $2.0 \leq R_r \leq 2.8$ in the system with $\alpha = 10$. Arrows indicate $\Delta\vec{r}_{NA,i}$ and are magnified by a factor of 200. The central region with a distance to the reference particle being less than 5.6 (here the axis is not normalized) indicated by the black circle is removed for clarity.

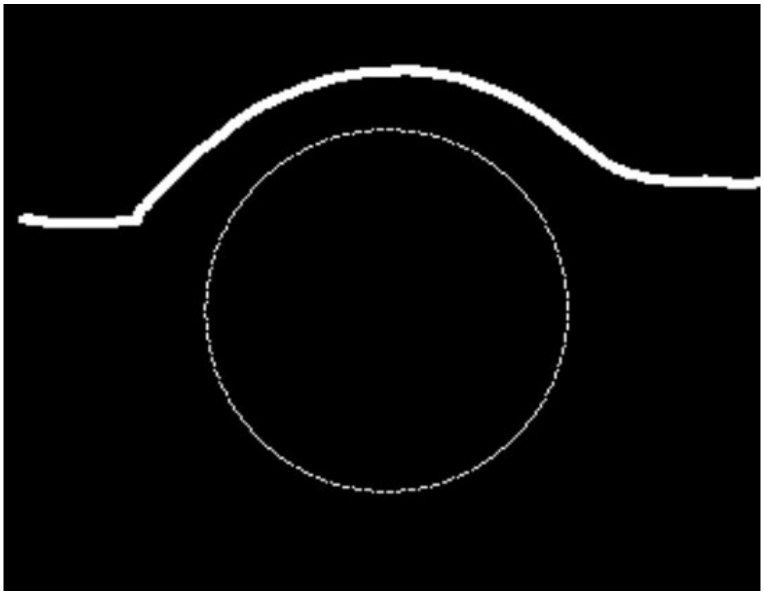

Figure 3.7: Example of the fake trajectory obtained by combining the affine shear flow and the field of Fig. 3.6 around the same large particles as in Fig. 3.2(b).

At the top left and bottom right, the mean non-affine flow field is outward, whereas at the top right and bottom left, the mean non-affine flow is inward. The top left and bottom right, relative to the reference particle, are referred to as the "compressive directions" as the imposed affine flow tries to push neighboring particles toward the reference particles [9, 10]. This affine push is resisted by the large reference particle, resulting in outward-pointing non-affine motion. Likewise, the regions at the top right and bottom left are referred to as the "extensional directions" in terms of the background flow, and the non-affine motion is inward. In fact, adding the background affine shear flow to the nonaffine flow field of Fig. 3.6 yields the qualitative sketch of Fig. 3.2(b). One example is provided in Fig. 3.7 where the trajectory is integrated using the affine motion and nonaffine motion in Fig. 3.6 from the starting position. This non-affine motion field clearly illustrates the importance of relative positions in the polydisperse sample.

We then wish to understand how the flow patterns measured by $\Delta\vec{r}_{\mathrm{NA}}(x, y)$ depend on the reference particle size R_r, so accordingly Fig. 3.8 shows four examples of the

$\hat{r}$ component of this field. The top two panels are data from the broadest particle size distribution, examining the flow around smaller (top left) and larger (top right) particles. For comparison, the bottom two panels are from the simulation with the bidisperse distribution, again showing the smaller (bottom left) and larger (bottom right) of the two particle sizes. The first observation is that the pattern of the field in the top left panel is opposite to the one at top right. We find it changes gradually with increasing R_r, see Fig. 3.9(a) below. In both of the top panels, a large near field and a relatively small but still clear far field can be identified. Both near and far field behaviors change with R_r. The second observation is that the data from the bidisperse sample shown in the bottom panels is qualitatively different: the regions near by reference particles have rings related to the pair correlation function, and the far field is closer to the neutral color.

The interpretation of Fig. 3.8(top right) is that large particles are strong, move more affinely, and force the other particles to detour around them. For the smaller reference particles in Fig. 3.8(top left) the influence of the reference particle is clearly different. At the surface of these small reference particles, for a center of a neighboring particle to be close, the neighboring particle must also be small. Thus the region immediately around the small reference particle looks similar to the region around the large particle: small reference particles cause an outward non-affine motion along the compressive direction, and inward non-affine motion along the extensional direction. However, farther away from small reference particles, the size of neighboring particles can be significantly larger than the reference particle. These small reference particles are weaker and more likely to be moved nonaffinely by their neighboring particles. Thus, the inward moving (dark blue) colors around the small reference particle along the compressive directions reflect that, on average, the small reference particle is being pushed away from the neighbors along these directions. In other words, the non-affine motion pattern around large reference particles, as seen in Fig. 3.8(top

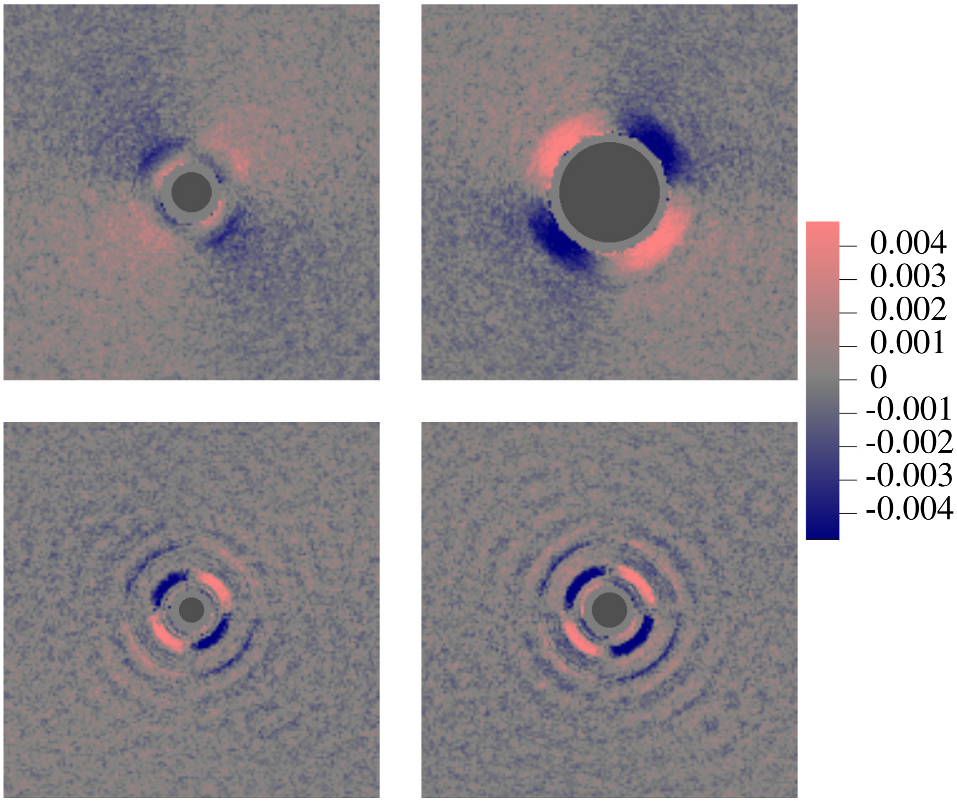

Figure 3.8: Color field of $\Delta\vec{r}_{\mathrm{NA,i}} \cdot \hat{r}$; the dot product with $\hat{r}$ selects for components of the motion that are outward (light red) or inward (dark blue), as indicated by the color bar. From left to right, the top two panels are size ranges $R_r = 0.80 - 0.84$ and $2.0 - 2.8$ using data from the broadest size distribution ($R_{\mathrm{max}}/R_{\mathrm{min}} = \alpha = 10$). The bottom two panels are from the bidisperse system (particles in size ratio $1 : 1.4$) for the small (lower left) and large (lower right) particles.

right), is precisely because the large reference particles are larger than many other particles; and the pattern around smaller reference particles is qualitatively different precisely because they are smaller than many other particles.

To verify this assertion, we quantify the behavior of $\Delta\vec{r}_{\mathrm{NA}}(x,y)\cdot\hat{r}$ by least squares fitting the field data to $-A_2(R_r,r)\sin 2\theta$, that is, switching from (x,y) to (r,θ) with the origin sitting at the center of the reference particle and taking advantage of the symmetry of Fig. 3.8 to express the magnitude of the flow in terms of the amplitude $A_2(R_r,r)$. In this way, r is the distance to origin and θ is the angle between the line of r and the horizontal line passing origin pointing to the right. This amplitude varies as a function of distance r to the center of the reference particles. The results for $A_2(R_r,r)$ for several reference droplet radii R_r are shown in Fig. 3.9(a), showing an obvious dependence of $\Delta\vec{r}_{\mathrm{NA}}$ field on size. For the largest reference particles [$R_r = 5$, the dark purple curve] A_2 is negative for all distances r from the reference particles. This negative A_2 indicates that the large particles are strong, and cause the average flow field sketched in Fig. 3.2(b) and quantified in Fig. 3.8(top right). The shape of A_2 gradually changes with decreasing R_r. For the smallest reference particles [$R_r = 0.5$, the light pink curve], A_2 is positive over most of the range, with a small exception at the smallest r. This confirms that these particles are weak, and are the ones whose motion is most often perturbed by the larger particles, quantifying what is seen in Fig. 3.8. These results are qualitatively different from the bidisperse case where the two A_2 curves for the two sizes show similar oscillatory pattern, as shown in Fig. 3.11(a) and (b), which reflects the pair correlation function and matches the rings visible in the bottom two panels of Fig. 3.8.

We then wish to understand how these results depend on the reference particle size R_r. In particular we will focus on the far field: in some cases $A_2 > 0$ for large r indicating weak particles, and in others, $A_2 < 0$ indicating strong particles. We quantify the far field by calculating the average $\langle A_2(r)\rangle_r$ over $R_r + 6 \leq r \leq 40$; the

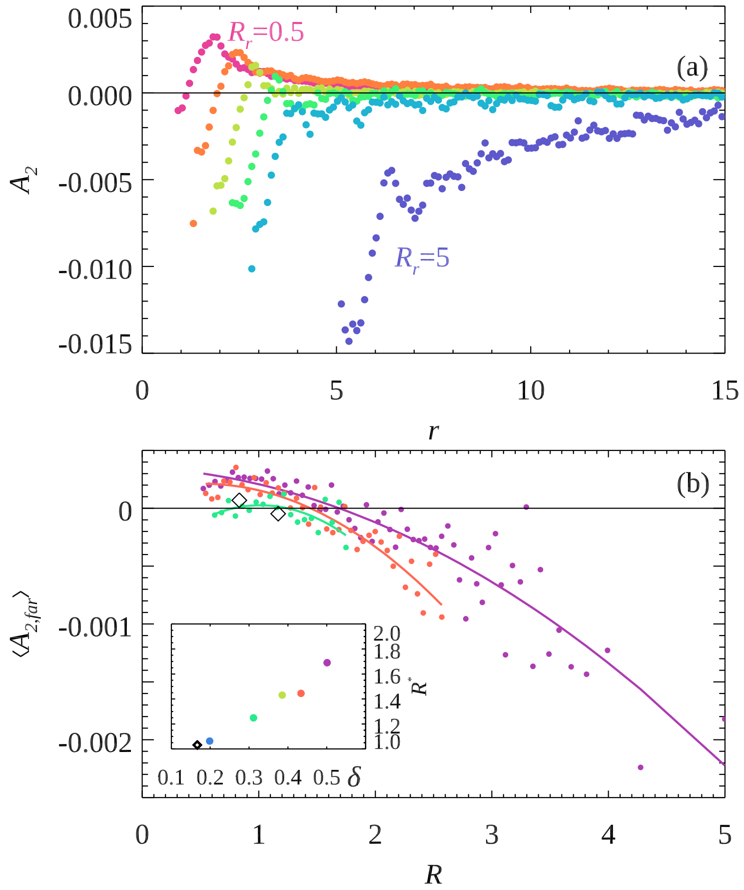

Figure 3.9: (a) A_2 against distance r for the $\alpha = 10$ system. Color indicates different R_r. (b) $\langle A_{2,far}\rangle$ versus R curves for three systems. The color here indicates size spans for exponential size distributions [$\alpha = 10, 5$, and 3; colors matching Fig. 3.3(a)] and the open diamonds correspond to the bidisperse system. Solid lines are quadratic fits to guide the eye. The crossing zero point at each solid line is defined as R^*. The inset in (b) shows R^* obtained from A_2 as a function of the polydispersity.

results are not sensitive to this choice of averaging region. The data are shown in Fig. 3.9(b), confirming the qualitative results discussed above: that the flow pattern for non-affine motion differs in sign for small reference particles as compared to large reference particles. Solid lines are quadratic fits to guide the eye. These results answer two interesting questions. First, for a given size distribution, how do we distinguish between "large" and "small" particles? The size R_r for which $A_2 = 0$ gives us a threshold R^* separating the two particle sizes. For the broadest particle size distribution that we have discussed extensively above, $R^* \approx 1.7$. Essentially this analysis says that large particles are strong in the sense of causing the flow field sketched around a large particle in Fig. 3.2(b), and that small particles are weak in the sense of being more likely to follow the Fig. 3.2(b) flow field around larger particles. Second, how does R^* depend on the particle size distribution? The inset to Fig. 3.9(b) shows R^* as a function of the polydispersity δ of the particle size distributions. Not surprisingly, R^* grows for broader particle size distributions. Intriguingly, the amount of particles larger than R^* decreases from 39% at $\alpha = 2$ to only 9% at $\alpha = 10$, our broadest size distribution.

A short conclusion here: 1) large particles behave qualitatively different than small ones; 2) a transition particle radius, R^*, separating the two classes of particles can be defined; 3) these effects become increasingly important as the particle size distribution broadens.

Before moving on to the $D^2_{min,i}$ results in the next section, we here demonstrate that one simple relative size idea is able to explain each A_2 curve in Fig. 3.9(a). We again start from exponential $\alpha = 10$ system. To save computational cost, we here divide the particles into 8 bins noted as from bin_1 to bin_8 based on size (See caption of Fig. 3.10 for the size range of each bin). We first calculate the $\Delta\vec{r}_{NA,i} \cdot \hat{r}$ field with only one bin of particles R_b in the background for each reference bin, *i.e.* 8 A_2 curves for each reference particles bin. Here R_b is the radius of background particles.

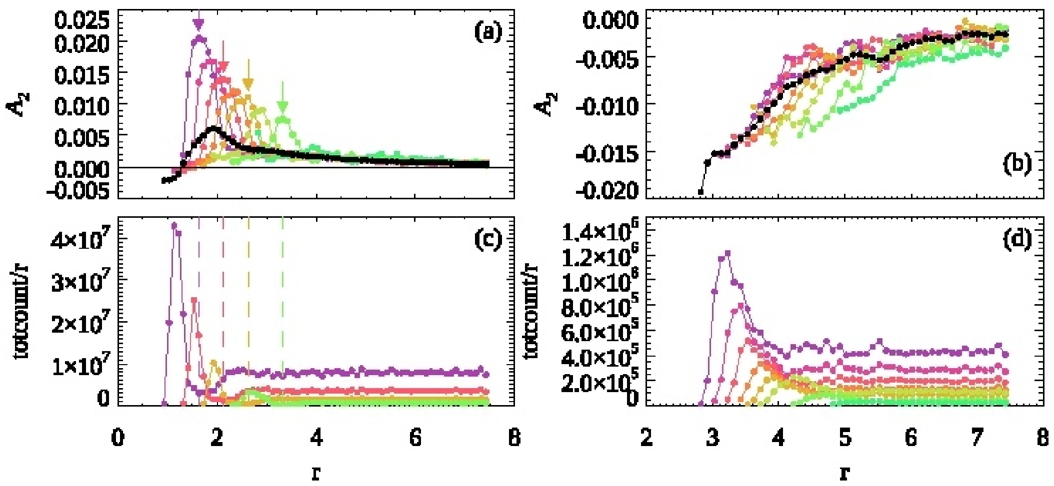

Figure 3.10: A_2 and $count/r$ versus r curves for the smallest (panel a and c) and largest (panel b and d) reference particle subgroups in the $\alpha = 10$ system. Color indicates bins. From purple to light green, the size range is $0.5 - 0.7$, $0.7 - 0.9$, $0.9 - 1.1$, $1.1 - 1.3$, $1.3 - 1.5$, $1.5 - 2$, $2 - 2.5$, $2.5 - 5$. Black curves in panel a and b show results using all particles (all 8 bins) in the background. For clarity, only 4 curves corresponding to the 4 arrows in panel a are plotted in panel c.

For example, for bin_1 as the reference particles, we have A_2 curves of using from bin_1 to bin_8 as background particles, resulting in 8 curves. Therefore, we generate 64 A_2 curves in total.

Figure. 3.10 shows comparison between the smallest and largest reference bins. In addition, the bottom two panels show the number of counts the relative background particles appear at the corresponding distance r to the center of the reference particle divided by r. This is alternative to the conventional plot of $g(r)$. In other words, the larger the value is, the more frequent, or more likely the background particles are to be at the distance r. We have checked $g(r)$ and find same results. Here we use the count to show that our statistics are fairly good. Color indicates different bins in the background and black shows results using all particles (all 8 bins) in the background. It is obvious that particle size again is important. Different relative sizes lead to different shapes of A_2 curve. For a small R_r like in Fig. 3.10(a), the peak value of A_2 decreases with R_b. No clear peak can be found for large R_r. The far field value of A_2 however does not show a clear trend or dependence on R_b. We also notice that the position of peak A_2 in Fig. 3.10(a) coincides with the first valley of corresponding curve in Fig. 3.10(c), indicated by arrows in Fig. 3.10(a). We interpret it from one possible microscopic picture. Some background particles strongly prefer to moving away at such distance r (valley at r in Fig. 3.10(c)) while other particles behave exactly the opposite (peak at r) or have no preference, leading to the large A_2. More importantly, the difference between the black A_2 curve and the sum of other colors weighted by the *count*/r curves in Fig. 3.10(c) is negligible, leading to

$$A_2^{(R_r,all)} = \sum_i w_i A_2^{(R_r,R_{b,i})} \tag{3.1}$$

Here, i indicates the group of background particle with radius $R_{b,i}$ and w_i is the weight of group i calculated as $w_i = count_i / \sum_i count_i$. Equation 3.1 illustrates that each A_2 curve in Fig. 3.9 is simply the weighted sum of contributions from all subgroups with various relative sizes. Other size spans and bidisperse system have also been checked and we reach same conclusions. Two more examples are given below in Fig. 3.11 and 3.12 for the bidisperse system and $\alpha = 4$ exponential size distribution system. Same results are reached. We hence note here that the validity of this expression is assumed to be applicable to any size distributions.

3.4 $D^2_{min,i}$

The other quantity independent from $\Delta\vec{r}_{NA,i}$ is $D^2_{min,i}$. We follow ref[48] and calculate it between strain γ and $\gamma + \Delta\gamma$ to measure the group nonaffine motion of particle i and its surroundings at strain γ.

$$D^2_{min,i}(\gamma) = \frac{1}{N_i}\sum_j^{N_i}[\vec{r}_{ij}(\gamma+\Delta\gamma) - E_i(\gamma)\vec{r}_{ij}(\gamma)]^2 \tag{3.2}$$

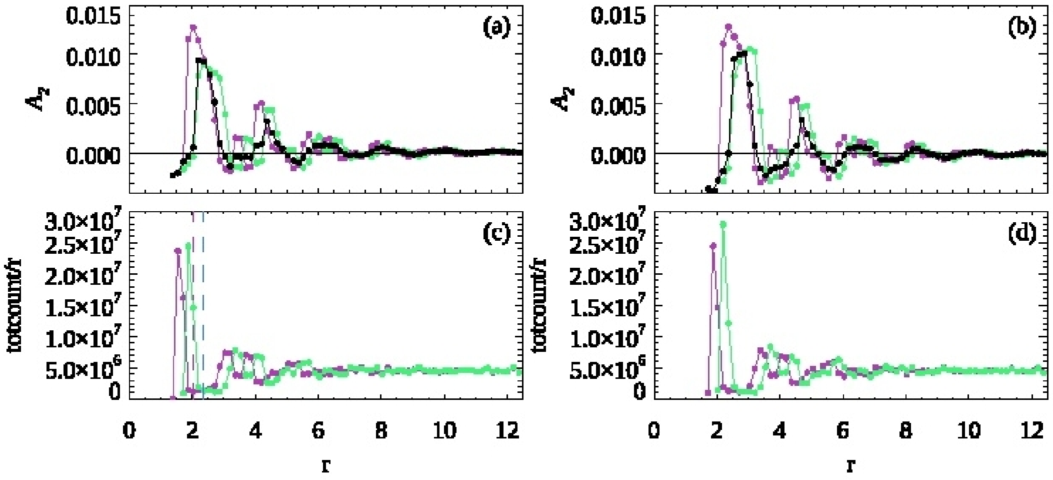

Figure 3.11: A_2 and $count/r$ versus r curves for the bidisperse system. Purple shows results for the smaller size and green corresponds to the larger size. Black curves show results using all particles in the background.

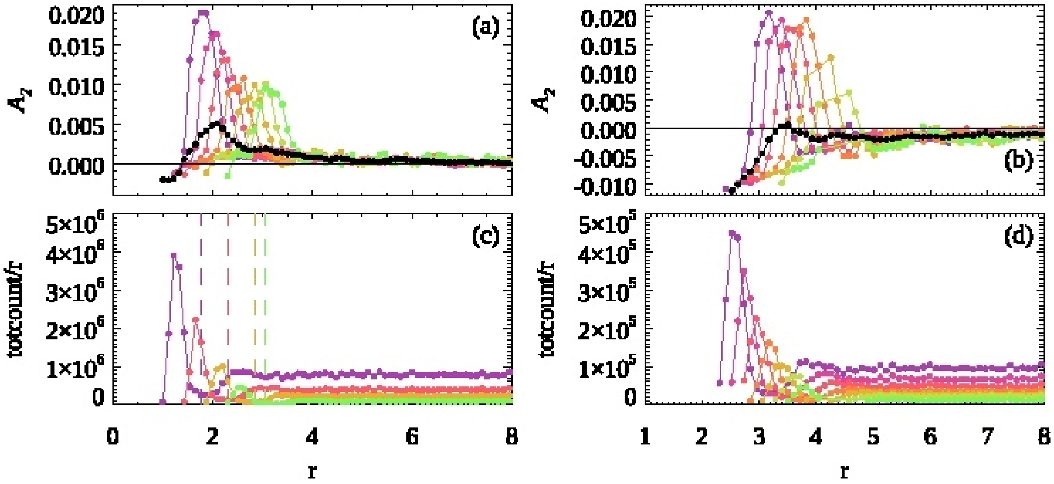

Figure 3.12: A_2 and $count/r$ versus r curves for the $\alpha = 4$ system. Color indicates the six bins and black curves show results using all particles in the background. The left two panels are for the smallest reference particles bin and right two are for the largest. Only four colors are shown in panel (c) for clarification. Vertical dashed lines in panel (c) correspond to the first minima.

Here, the summation range N_i are neighbors of particle i. We fix $N_i = 15$ for all particles by taking the closest 15 particles to particle i from the surface to surface distance. $\mathbf{r}_{ij}(\gamma)$ is the separation vector between particle i and j at strain γ. $E_i(\gamma)$ is the local strain tensor that minimizes $D^2_{min,i}$ for particle i at strain γ calculated by least square fitting. This local strain defines the local affine group motion for all the neighbors, which is the second term in the summation in equation (3.2). We note that $D^2_{min,i}$ quantifies the averaged deviation of all the neighbor motions from this local affine group motion, and is calculated based on the relative motions to particle i. In other words, a large $D^2_{min,i}$ does not imply specifically that particle i is moving problematically, but the particles in the neighborhood of particle i are moving incoherently, indicating possible plastic rearrangements. The idea in one sentence is that it measures how nonaffine the local group displacements around a particle are. If the motions of these particles can be perfectly described by a deformation tensor (strain tensor) $\leftrightarrow E$, then these motions are perfectly affine and the nonaffinity of the group is 0, $D^2_{min,i} = 0$ at this moment. $D^2_{min,i}$ thus can serve as a localized plastic rearrangements indicator and characterizes the local plastic behavior. Larger $D^2_{min,i}$ value in general indicates larger plastic deformation in the specific local neighborhood.

One important feature of $D^2_{min,i}$ is that it highly depends on the number of neighbors included in the calculation. We notice that $D^2_{min,i}$ increases with number of neighbors when using simple random Gaussian distributed motions and random relative positions of neighbors. Thus, a constant N_i is required for properly compare $D^2_{min,i}$ of different sizes of particles. Previous choices of N_i definition to name a few include: 1) particles within a certain distance to the reference particle i are considered neighbors (usually the first minimum $g(r)$ distance); 2) the first layer of neighbors in contact; 3) first Voronoi layer particles as neighbors. These ideas work for low polydisperse systems since N_i varies little for different particles. They fail to work in our polydisperse systems because on one hand N_i defined in these ways strongly

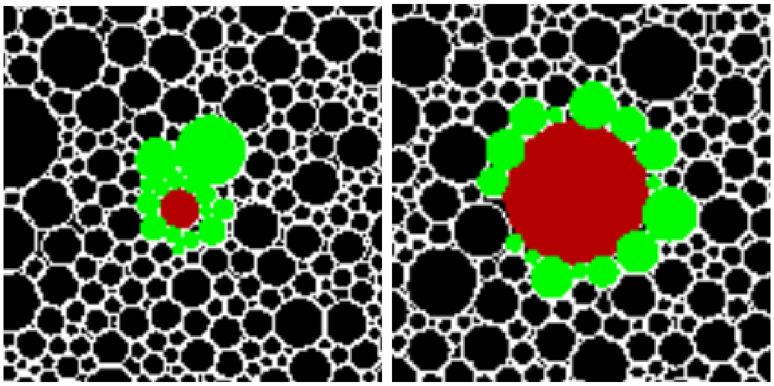

Figure 3.13: Two examples of our neighbor definition. We use the closest 15 particles as neighbors of the reference particle. Red indicates reference particle and green is for neighbor. Left panel is for a $R = 1.5$ particle and right is for an $R = 5$ particle (the largest).

depends on particle size, and on the other hand it is possible that big particles would never be the neighbors of small ones. Therefore, we choose to use the closest 15 neighbors in our calculation. Other choices of such as 10 and 20 are also tried. The main results remain almost the same and our conclusions do not change. However, $N_i = 15$ generally returns us around two layers of neighbors for the smallest particles and slightly less than a full layer of neighbors for the largest particle in our exponentially distributed system, which is reasonable for our purposes. Two examples are provided in Fig. 3.13.

We again first check the dependence on the sizes of particles in the systems, as shown in Fig. 3.3(b). Similar to individual nonaffine motion result, on average $D^2_{min,i}$ decreases with particle size for all systems, including the bidisperse system. The negative slope of $D^2_{min,i}$ suggests smaller plastic rearrangement during the strain interval in the local neighborhood very close to the surface of large particles. One possible explanation is that at the region very near the surface of large particles, the special movement pattern shown in Fig. 3.2(b) dominates and neighbors mainly behave accordingly and coherently. In the meantime, this detour motion conflicts with particles nearby that can move affinely. This leads to possible rearrangements near

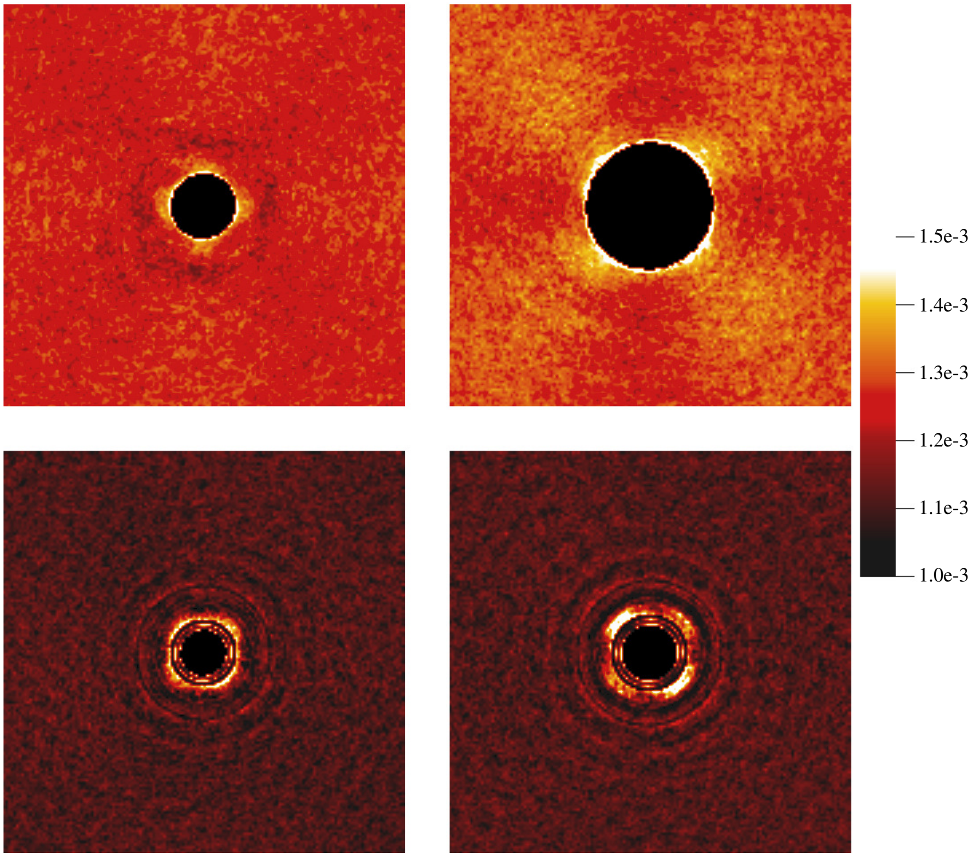

Figure 3.14: Color field of $\frac{D^2_{min,i}}{\langle R \rangle^2}$ for the same groups of particles in Fig. 3.8. Color bar indicates the magnitude.

large particles, promoting large $D^2_{min,i}$ for small particles. Therefore, it is more likely to observe large $D^2_{min,i}$ values at certain positions around large particles in the system. Note that again, the bidisperse results also collapse well to the family, showing clear different $D^2_{min,i}$ values for small and big particles. These are clear evidence indicating that size is important.

To confirm the position dependence we anticipate, we follow the same way we investigated the nonaffine motion field in the previous section and show the same four examples as in Fig. 3.8 of the $D^2_{min,i}$ field in Fig. 3.14. We focus on the same places and directions where the outflow and inflow lie and point, *i.e.* the compressive and extensional directions. The top two panels again show opposite patterns of $D^2_{min,i}$ field for small and large reference particles. Moreover, the clear quadrapole pattern around large particles agrees with our position argument above, emphasizing the importance of “relative positions” regarding the local plastic behaviors. The patterns of bidisperse system are qualitatively different from the top two panels and are almost the same for the two sizes of particles. We note that the magnitude of $D^2_{min,i}$ away from the very surface of the reference particles in the top panels is larger than the bottom panels, suggesting an enhancement of local plastic rearrangements with the presence of large polydispersity. A much larger decay length can also be found for the top two panels. In other words, the length scale of the effects brought by the presence of big particles is much larger in the highly polydisperse systems. A quantification of such decay length and its dependence on the sizes would be interesting.

Similar quantification method is applied to the $D^2_{min,i}$ field with

$$D^2_{min,i} = -A_4(R_r, r)\cos 4\theta + B \tag{3.3}$$

Here r and θ is defined in the same way as we did for A_2 analysis. Again, the A_4 versus r curves also depends on R_r. An example is in Fig. 3.15. A positive A_4 value corresponds to the typical quadrapole pattern around large reference particles. A negative one then is for a quadrapole pattern with shifted phase, which looks completely opposite to positive case, corresponding to small reference particles. A_4 reaches the background value at $r > 10$ (corresponding to 20 in the x axis in Fig. 3.15), indicating the large decay length and that the influence of large particles can extend to very far away. It also shows that we can quantify the decay length by either simply finding the r where A_4 first reaches the background value or first fitting the curve and then obtain the length. We leave this to future study.

We use the same far field definition as in previous section and calculate the mean far field A_4 to perform the same R^* analysis. A comparison between $\langle A_{2,far}\rangle$ and $\langle A_{4,far}\rangle$ is shown in Fig. 3.16. We define R^* the same way and find a similar trend

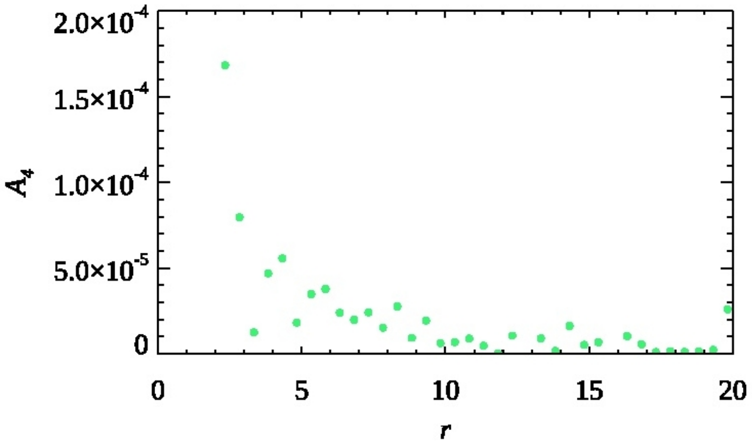

Figure 3.15: An example of A_4 versus r curves in the $\alpha = 10$ system for $R_r = 2 - 2.8$ particles.

to the result from A_2, as shown in the insets. Same conclusion can be drawn as in previous section. The comparisons between the R^* and mean radius $\langle R \rangle$ for each size distribution from A_2 and A_4 analysis are shown in the insets of Fig. 3.16. Take the $\alpha = 10$ system as an example, the R^* from A_2 analysis leads to 9.2% of particles being large and 7.2% from A_4 result. In terms of area of particles, R^* from A_2 analysis corresponds to 37.4% of particle area being large and 32.5% from A_4 result. However, we have checked the percentage of large particle either in terms of particle number or area, from both A_2 and A_4 analysis against the polydispersity and α, and find no clear trend.

3.5 Discussion

The above two sections contain our main results from investigations on the size dependence of various quantities and comparisons between polydisperse and bidisperse systems. All our results shown here are strong evidence that polydispersity is important and different sizes of particles need to be treated differently. We also demonstrate that two major questions can be addressed: 1) for a given size distribution, is there a threshold radius R^* that effectively distinguishes between small and big? 1) if so, how

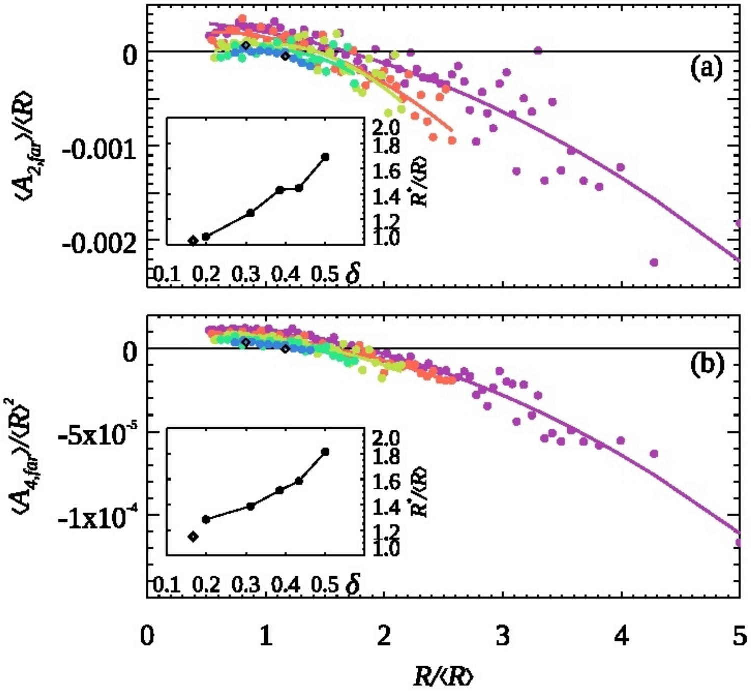

Figure 3.16: A comparion between $\langle A_{2,far} \rangle$ and $\langle A_{4,far} \rangle$ against R_r for all systems. Here panel (a) shows same results as in Fig. 3.9. Solid lines are quadratic fitting to guide the eye. Color indicates different size distributions and black diamonds are for bidisperse system. Insets show R^* versus polydispersity δ.

does this particle size scale depend on the particle size distribution? The consistent results from our analysis using two separately defined quantities $\Delta\vec{r}_{NA,i}$ and $D^2_{min,i}$ verify that R^* exists and grows for larger size spans.

A further consequence of our work will be on predicting sites of plasticity in highly polydisperse athermal amorphous materials under shear or particle rearrangements at finite temperature. Current analyses typically focus on the rearrangement statistics of only large particles, or implicitly assume via their definition of plastic activity that the qualitative nature of rearrangements are insensitive to particle size [95, 30, 118, 8, 12, 36, 105]. Our results suggest that if one wishes to perform similar analysis in polydisperse materials, a definition of softness that explicitly depends on particle sizes will be necessary.

3.6 Conclusion

In this work we have shown that in a sheared amorphous material with high polydispersity, particle size matters. Large particles are more likely to move affinely, following the imposed shear flow, as they feel the average motion of all of their neighbors. We term such particles as “strong” in the sense that they resist being pushed non-affinely by their neighbors. The imposed shear flow causes those neighbors to detour around the strong particles, which means the smaller a particle is, the “weaker” it is and thus the more its motion is nonaffine. We show that one can quantify this by identifying a transition particle radius, R^*, separating the two classes of particles. Furthermore, we see that these effects become increasingly important as the particle size distribution broadens. Intriguingly, we demonstrate this distinction still matters, albeit only slightly, for the canonical bidisperse sample with particle size ratio $1 : 1.4$. Nonetheless, the behavior of the highly polydisperse samples is qualitatively distinct from the more homogeneous samples with low polydispersity. Our results may have implications, e.g., for diffusive motion in biological cells, which are highly polydisperse crowded environments [114].

Chapter 4

Isomorph theory on sheared glassy systems: Part I

The majority of this chapter of this dissertation was first published as follows: [67]. copyright(2019) American Physical Society. Reused with permission.

We study hidden scale invariance in the glassy phase of the Kob-Andersen binary Lennard-Jones system. After cooling below the glass transition, we generate a so-called isomorph from the fluctuations of potential energy and virial in the NVT ensemble: a set of density, temperature pairs for which structure and dynamics are identical when expressed in appropriate reduced units (meaning of hidden scale invariance). To access dynamical features, we shear the system using the SLLOD algorithm coupled with Lees-Edwards boundary conditions (see chapter 2) and study the statistics of stress fluctuations and the particle displacements transverse to the shearing direction. We find good collapse of the statistical data, showing that isomorph theory works well in this regime. The analysis of stress fluctuations, in particular the distribution of stress changes over a given strain interval, allows us to identify a clear signature of avalanche behavior in the form of an exponential tail on the negative side. This feature is also isomorph invariant. The implications of isomorphs for theories of plasticity are discussed briefly.

I use the RUMD package for simulation and python for analysis and xmgrace for making figures in this chapter.

4.1 Introduction

Background information can be found in chapter 1. In our investigation here on the steady state part of the stress and strain curves, we consider a glassy system created by cooling a viscous liquid down below its glass transition and then apply Couette-type shearing at constant volume and fixed strain rate. This necessarily involves a departure from equilibrium and in principle introduces a potential dependence on thermal history, for example, through the cooling rate, as well as possible aging effects, into the system's behavior. We minimize these issues by restricting our attention to steady-state shearing: If one shears the system at a constant strain rate beyond, say, 0.5 or 1.0 strain, a steady state is obtained which depends only on the density, the temperature, and the strain rate. We define the system entering the steady state here when the stress starts to fluctuate around a certain mean value.

More specifically, we work with the usual Kob-Andersen binary Lennard Jones glass forming model[71, 72, 73], which is useful because it is difficult (though not impossible[133, 65]) to crystallize on computer timescales. Our system contains 800 big (A) particles and 200 small (B) ones. From now on, when not using reduced units, we work with the unit system defined by the Lennard-Jones (LJ) parameters of the A particles' interactions with each other, σ_{AA} and ϵ_{AA}, and the mass which is the same for both A and B particles; thus, temperature is given in units of ϵ_{AA}/k_B. The potential is cut off using the shifted-force method[132] at 2.5σ for each type of interaction. I first run a NVT simulation to equilibriate the system at a high temperature $T = 1$. The glassy states are created by cooling the liquid at constant pressure (NPT simulation) at a fixed cooling rate from temperature $T = 1.0$ down to a given start temperature T_{start}. Different cooling rates are applied, but for the steady-state results presented in this work the cooling rate is not relevant. The reason for cooling at fixed pressure rather than fixed volume is to avoid arriving at a state where the pressure is very low or negative, since good isomorphs are generally obtained at not too low pressures.

We are interested at two glassy systems acquired after the above steps: 1) $\rho = 1.265$ and $T = 0.55$ and 2) $\rho = 1.324$ and $T = 0.1$, corresponding to two states in the thermodynamics phase diagram with one close to liquid state and one deep in glassy state, as shown in Fig. 4.1. We use the two as starting configurations and calculate two isomorphs (see next section for the method we use) for them separately, each containing 10 points. For these 20 configurations, we then shear them with different strain rates to a strain of at least 4 and focus on the data belonging to the second half of the shear, where the system is in the steady flow state. We analyze the statistics related to the stress there. We check the dependence on how "glassy" the system is by comparing the results of the two.

4.2 Methods to generate isomorph

The simplest way to express and identify hidden scale invariance was shown in Ref. [119], where the essential condition was stated as follows: A change of density must preserve the order of potential energies of microstates. In other words, $U(\mathbf{R_a}) < U(\mathbf{R_b}) \Rightarrow U(\lambda\mathbf{R_a}) < U(\lambda\mathbf{R_b})$ where upper case boldface $\mathbf{R}$ represents the entire 3N-vector of the particle coordinates and the density is scaled by λ. To test for scale invariance, we consider infinitesimal changes of density under uniform scaling, whereupon changes in the potential energies U of microstates are given by

$$dU = W d\ln\rho; \tag{4.1}$$

here W is the virial, a quantity typically calculated in computer simulations due to its appearance in the formula for pressure[1]. Requiring that the order of energies be preserved means in particular that configurations at a given density with the same U will experience the same change in U upon an infinitesimal change of ρ. By Eq. 4.1 this means they have the same W. In other words, the potential energy and virial must be strongly correlated (the discovery of strong U and W correlations[106] marked the beginning of the development of isomorph theory). Linear regression applied to a scatter plot of W versus U yields two parameters, namely, the correlation coefficient

$$R = \frac{\langle \Delta U \Delta W \rangle}{\sqrt{\langle (\Delta U)^2 \rangle}\sqrt{\langle (\Delta W)^2 \rangle}} \tag{4.2}$$

and the slope

$$\gamma = \frac{\langle \Delta U \Delta W \rangle}{\langle (\Delta U)^2 \rangle} \tag{4.3}$$

Here angular brackets denote canonical ensemble averages and $\Delta X \equiv X - \langle X \rangle$ for any quantity X. A value of R close to unity in a region of the phase diagram (typically values above around 0.9 are considered good, although lower thresholds have also been used[59]) indicates that the system exhibits hidden scale invariance and should have good isomorphs in that part of the phase diagram. The interpretation of the slope γ was given in Ref. [51]: It is the slope of curves of constant excess entropy (that is, configurational adiabats) in the $(\ln\rho, \ln T)$ phase diagram

$$(\frac{\partial \ln T}{\partial \ln \rho})_{S_{ex}} = \gamma(\rho, T) \tag{4.4}$$

The excess entropy is defined as the entropy minus that of the ideal gas with the same density and temperature and is one of the thermodynamic properties which is invariant along an isomorph. Thus, in systems with good isomorphs, the γ of Eq. 4.3 is just the density scaling exponent γ discussed above. In the Schrøder-Dyre formulation

Table 4.1: Thermodynamic data for the starting points of glassy isomorphs, obtained by cooling at constant pressure $P = 10.0$ from temperature 1.0 over 10^8 steps of size $dt = 0.0025$. The cooling rate is therefore 1.8×10^{-6} for cooling to T=0.55 and 3.6×10^{-6} for cooling to T=0.1.

$T_{start} = 0.55$					$T_{start} = 0.10$				
ρ	T	P	R	γ	ρ	T	P	R	γ
1.265	0.550	9.35	0.955	4.950	1.324	0.100	9.75	0.824	5.011
1.278	0.577	10.68	0.954	4.971	1.337	0.105	11.21	0.834	5.002
1.291	0.606	11.99	0.962	5.078	1.351	0.110	12.79	0.843	4.953
1.304	0.637	13.72	0.960	5.033	1.364	0.116	14.48	0.855	4.944
1.317	0.669	15.37	0.965	5.015	1.378	0.121	16.29	0.864	4.916
1.330	0.702	16.99	0.968	4.936	1.392	0.127	18.22	0.873	4.879
1.343	0.737	18.94	0.972	4.927	1.406	0.134	20.29	0.879	4.873
1.356	0.773	21.07	0.973	4.874	1.420	0.140	22.49	0.886	4.829
1.370	0.811	23.09	0.976	4.901	1.434	0.147	24.85	0.893	4.817
1.384	0.851	25.24	0.979	4.869	1.448	0.154	27.37	0.899	4.799

of the theory, the status of configurational adiabats was raised such that these are considered to define isomorphs in systems with strong U and W correlations[119]. Since $\gamma(\rho, T)$ can be calculated at any state point using the fluctuation formula 4.3, Eq. 4.4 provides a general method to generate isomorphs by numerical integration. Typically, steps of order 1% in density are used.

The temperatures chosen for starting isomorphs again are 0.55 and 0.1. For generating glassy isomorphs a configuration is drawn from the cooling run close to the desired temperature, and its density is used as the initial state for isomorphs. Due to fluctuations, its density is not necessarily the same as the mean density for the chosen temperature and pressure; similarly, when performing NVT simulations in the glassy state the mean pressure is close to but not equal to the pressure of the cooling run. Table 4.1 shows thermodynamic information including the isomorph parameters R and γ for the different state point along each of the two isomorphs.

We estimate that the starting temperature of our high-temperature isomorph corresponds, if we were to follow the isomorph down to the usual density 1.2, to a temperature close to 0.421. At this temperature the Kob-Andersen mixture can be equilibrated as a liquid, but it requires substantial patience (see discussion below); at the strain rates we apply in our deformation runs, the system can be considered a glassy solid. According to Chattoraj *et al.*[18], particle displacements become driven more by strain than thermal motion once the strain rate exceeds $10^{-2}/\tau_\alpha$, where τ_α is the relaxation time (in our study is obtained by fitting the self-intermediate scattering function to a stretched exponential function). Since our lowest strain rate is of order 10^{-5} and τ_α certainly exceeds 10^3, this criterion is met and therefore we can speak of deformation of a glassy amorphous solid, at least regarding steady state dynamics. Our second isomorph, starting at the lower temperature 0.1, gives a system deep in the glassy state for which virtually no spontaneous relaxation is expected on conceivable simulation timescales. From Table 4.1 we see that the R values for the lower-temperature isomorph are somewhat lower than for the high-temperature isomorph, staying between 0.8 and 0.9; one might therefore expect poorer collapse of curves, but we will see that this is not the case for our data. Starting with the glassy states taken from the cooling run as mentioned above, we ran NVT simulations and then increased the density in steps of 1% while adjusting the temperature based on the observed value of γ, according to

$$T_{n+1} = T_n[1 + \gamma_n(\rho_{n+1} - \rho_n)/\rho_n] \tag{4.5}$$

This integrates Eq. 4.4 numerically using the Euler method and when applied to systems in equilibrium generates curves of constant excess entropy. In applying it here we essentially ignore possible complications from being out of equilibrium, assuming, for example, that no significant aging occurs during this NVT simulation. The number of time steps is 10^7 and the starting configuration for each state point is the final configuration from the previous state point. Figure 4.1 shows three isomorphs in the density-temperature phase diagram including one equilibrium liquid isomorph and

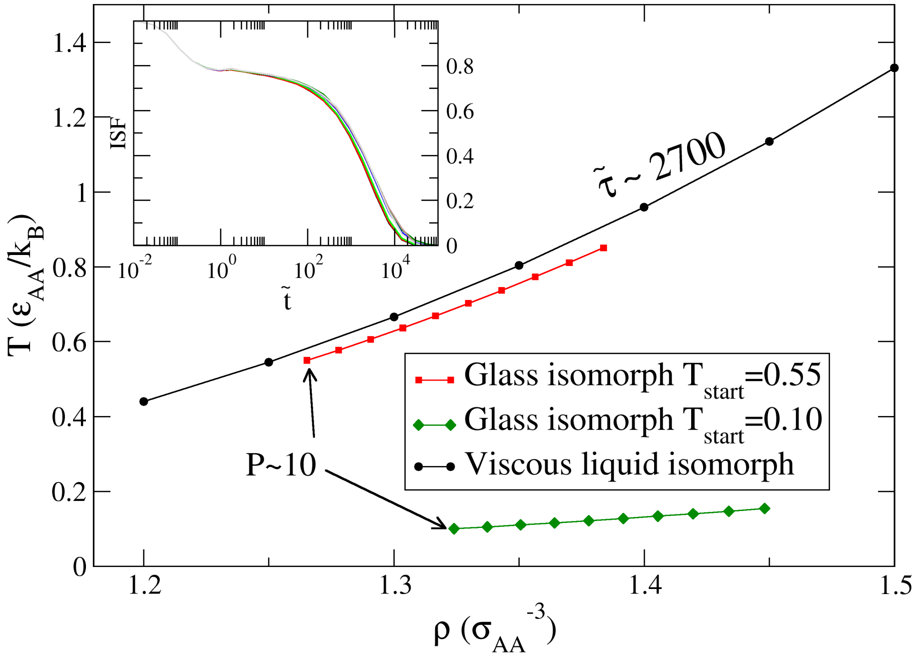

Figure 4.1: The black symbols indicate an isomorph in the supercooled liquid which includes the point $\rho = 1.2, T = 0.44$. We use this as a guide to locating the glass transition; its relaxation time is about 2700 in reduced units, corresponding to 3850 in LJ units at the lowest density 1.2). The inset shows the intermediate scattering function for the different state points, lying almost on top of each other. The red and green symbols indicate isomorphs generated in the glass which we use for studying deformation, referred to as those starting at temperature T=0.55 and T=0.1, respectively. Note that the starting densities are not the same, since these are taken from a cooling run at fixed pressure $P = 10$.

the two glassy isomorphs. Figure 4.2 shows a very good degree of collapse for the radial distribution function along the glass isomorphs when plotted as a function of the reduced pair distance $\tilde{r} = \rho^{1/3} r$. This is true even for the high-temperature isomorph, which one might expect to show some (small) changes of structure due to aging[74]. The results of isomorph calculated using above method are listed in Table. 4.1.

Before considering the stress and strain related results, it is useful to have an idea of where the glass transition is, so as to locate our glassy isomorphs in the

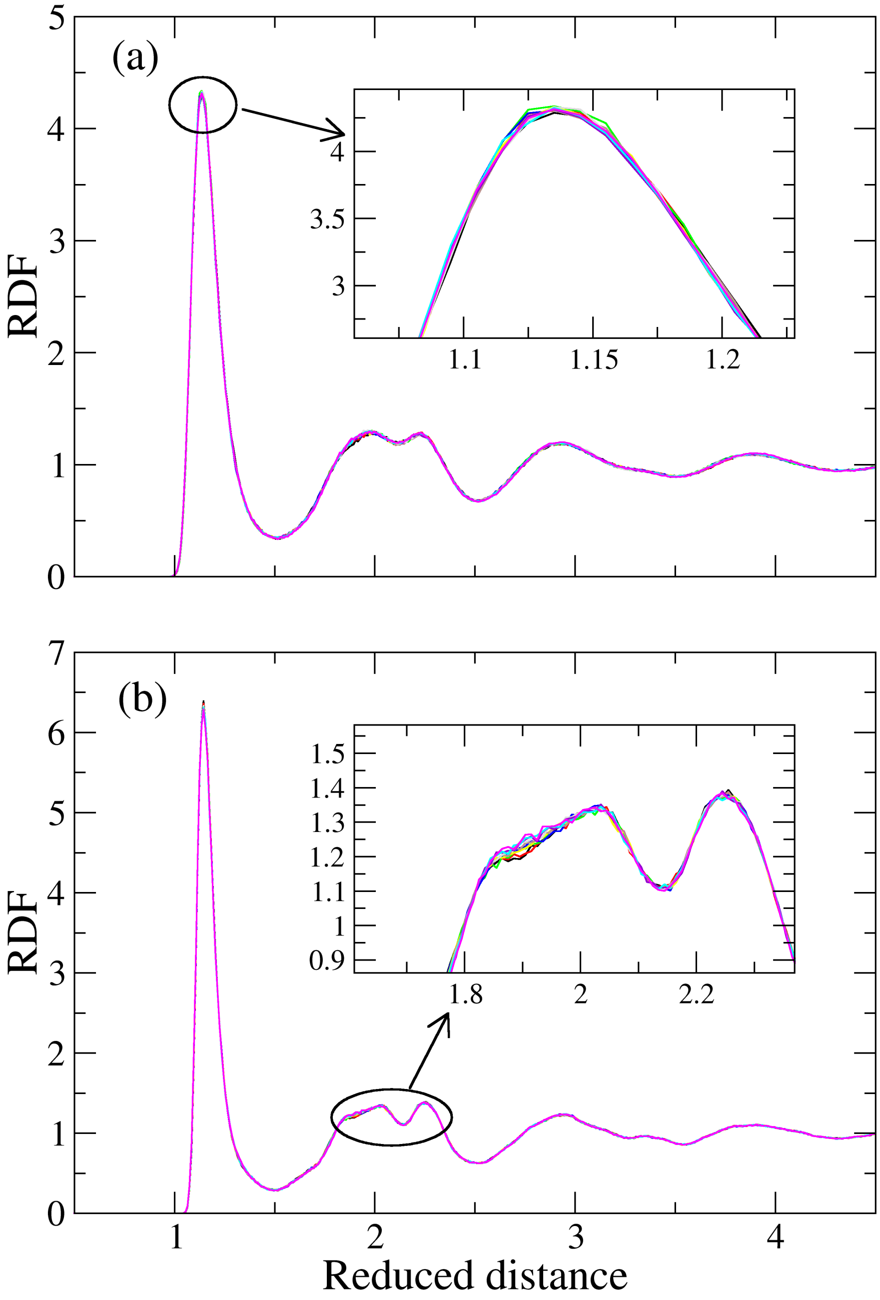

Figure 4.2: Radial distribution function for the large (A) particles in reduced units along glassy isomorphs starting at (a) $T = 0.55$ and (b) $T = 0.1$. Each figure shows 10 curves, where the density is increased by 1% for each state point, giving a 9.4% change in density overall; the temperature increases by 54% overall. The insets show close-ups of (a) the first peak and (b) the second peak where very some small deviations are discernible.

phase diagram and compare to other work on this system. When considering the full phase diagram the glass transition can be defined as the set of (ρ, T) points where the liquid's relaxation time attains some fixed value. There are two sources of ambiguity or arbitrariness in such a definition: which observable to use when defining the relaxation time and which value to set as defining $T_g(\rho)$. Experimentally, for the latter one chooses conventionally a value of order $100s$ in real units; with the isomorph theory in mind it is natural to specify a criterion in reduced units, since in a system with isomorphs the glass line will then correspond to an isomorph[52]. In computer simulations, relaxation times of order $100s$ are nowhere near realistic, so as a guide we choose a viscous liquid state which can be equilibrated in reasonable time. In Fig. 4.1 we plot a viscous liquid isomorph whose temperature at the usual Kob-Andersen density 1.2 is 0.44. The relaxation time there (based on fitting the self-intermediate scattering function of the A particles to a stretched exponential function) is 3850 (LJ units), which corresponds to about 2700 in reduced units. This isomorph is generated using the analytical expression for Lennard-Jones potentials as described in Ref. [13] (using the same reference density 1.6 but a slightly lower value of γ at the reference density, 4.58 instead of 4.59) and simulated for 10^8 time steps per state point. This line is used as a reference in our system.

4.3 Invariance of various quantities

Now that we have the two isomorphs, we then shear the total 20 configurations with various strain rates and check the invariance of quantities related to the steady state stress.

4.3.1 Analysis of Stress-strain Curves

We first directly check the stress and strain curves. It should be noted here that when identifying isomorph-invariant properties it is important that the shear rate be specified in an isomorph-invariant way; that is, the reduced-unit strain rate $\tilde{\dot{\gamma}} = \dot{\gamma}(k_B T/m)^{-1/2}\rho^{-1/3}$ should be fixed when comparing the stress and strain curves at different density-temperature points on an isomorph[124]. The full set of flowing states is therefore characterized by a triple $(\rho, T, \tilde{\dot{\gamma}})$. Since the physics is in principle invariant along a (ρ, T) isomorph at a given reduced strain rate, we have thus a two-dimensional phase diagram, where a state can be labeled by the isomorph and reduced strain rate. This has been previously shown in the nonviscous regime for the Lennard-Jones fluid[124], but has not been tested below the glass transition. In our simulations we choose nominal strain rates of 10^{-2}, 10^{-3}, 10^{-4}, or 10^{-5} and nominal time step of 0.004. By "nominal" time step and strain rate we mean the value in real units at the first point of each isomorph. These values are scaled to keep the reduced-unit time step and strain rate (SR) fixed along the isomorphs. For all our deformation runs we simulated 10^8 molecular dynamics steps, which for the above nominal strain rates give total strains of 4000, 400, 40, and 4, respectively. Chattoraj *et al.* found that total strains of up to 13.0 or even 24.0 were necessary for accurate statistics[18]. This suggests that our runs are sufficiently long except possibly for the lowest strain rates. Note that the strain itself is dimensionless and therefore does not need to be put into reduced units.

Isomorph theory predicts the whole stress-strain curve to be invariant along isomorphs when stress is given in reduced units $\tilde{\sigma} = \sigma/\rho k_B T$. In the small systems typically studied in simulations and particularly at low temperatures and strain rates, however, stress-strain curves in the glassy regime exhibit extremely intermittent behavior[92, 93, 94, 3] which is sensitive to initial conditions and other sources of randomness. Examples of this can be found in Fig. 4.3. Therefore, a collapse of the

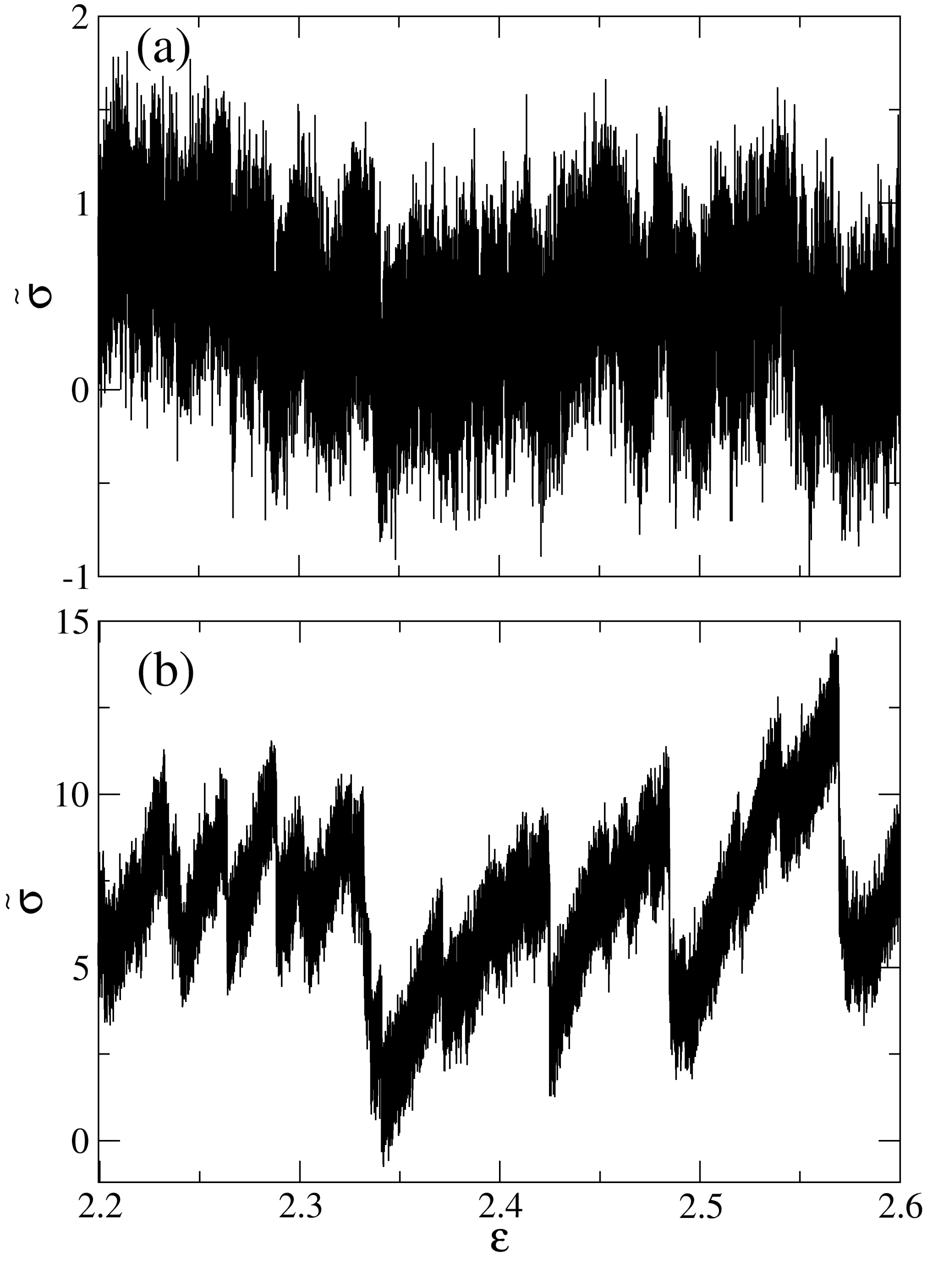

Figure 4.3: (a) Section of stress-strain curve for lowest-density state point on the higher-temperature isomorph ($\rho = 1.265, T = 0.550$) at the lowest nominal strain rate 10^{-5}. (b) Section of stress-strain curve for a state point on the lower temperature isomorph ($\rho = 1.324, T = 0.100$) at the lowest strain rate 10^{-5}. The abrupt drops can be identified with avalanches of plastic activity. The difference in vertical scale between (a) and (b) can be attributed partly to the definition of reduced units for stress.

actual stress-strain curves cannot be expected, except perhaps the initial part which covers the elastic regime and the transition to a flowing state. We hence choose to study the statistical properties of the steady-state region instead where properties become time independent, apart from fluctuations.

It should be noted that in principle, however, isomorph theory allows for independent configurations from equilibrium states above the glass transition which are isomorphic to each to be cooled into the glassy state in an isomorphic way such that the entire thermal histories and deformation histories are isomorphic. In that case the entire stress-strain curves could be compared, rather than simply the steady state part. Some ten years ago Lerner and Procaccia proposed a scaling theory for steady-state plasticity based on approximating the pair potential by an inverse power law[82]. The relation between that work and isomorph theory will be discussed below in this section.

The most basic statistical measures that can be extracted from the stress-strain curve are the mean value of the stress (the flow stress) and its standard deviation. Figure 4.4 shows these quantities plotted in reduced units along the two isomorphs studied, with different nominal strain rates. The curves are consistent with being all flat within the statistical error (for the flow stress at the highest strain rate and the low-temperature isomorph a small systematic decrease with increasing density can be detected, not visible on the scale of the figure). The errors are rather large for the standard deviation at the lowest strain rates where, as we noted above, the total strain is significantly smaller. This figure demonstrates isomorph invariance, the focus of this work. We can also comment briefly on the strain rate and isomorph dependence. The dependence of flow stress on strain rate is relatively weak given three orders of magnitude variation in the latter. Equivalently, the shear viscosity varies by several orders of magnitude, indicating we are in a strongly non-Newtonian (shear-thinning) regime, as expected for glassy systems[11, 138]. Comparing the two isomorphs, the

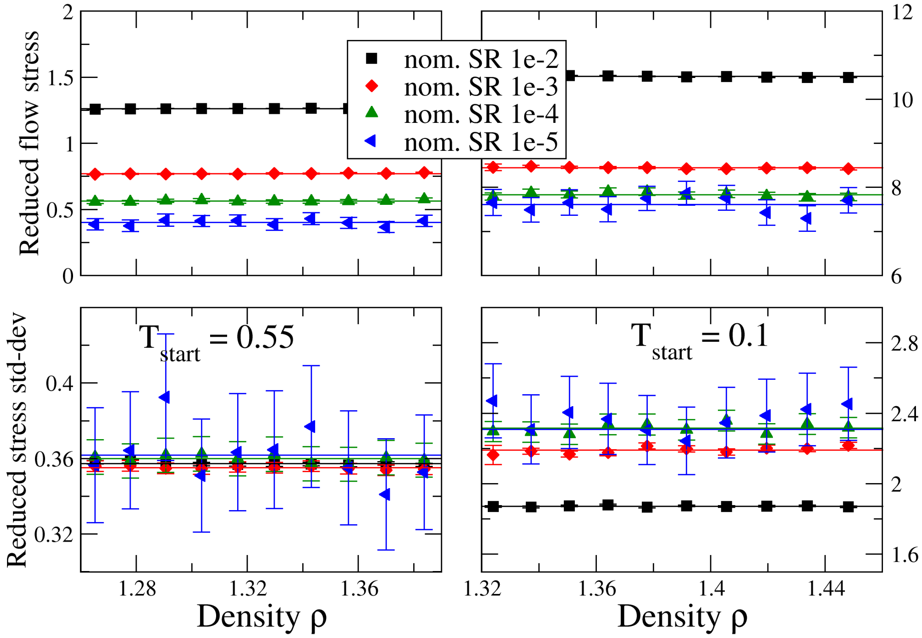

Figure 4.4: Flow stress and standard deviation during steady-state regime as a function of density along (left panels) high- and (right panels) low-temperature isomorphs for different strain rates. The legend indicates the nominal strain rates, that is the real strain rates at the first point on each isomorph; for other state points in each data set the reduced unit strain rate is the same. Error bars have been calculated using standard formulas[130]; the horizontal lines indicate the mean value over the isomorph.

reduced flow stress is a almost factor of 10 smaller at the high-temperature isomorph compared to the low-temperature one, partly reflecting its proximity to the supercooled liquid state, but to some extent also an effect of our choice of reduced units (see below for a discussion of alternative choices). Interestingly, for the high-temperature isomorph the fluctuations of the stress are independent of the strain rate (as well as being invariant along the isomorph). This must mean that the fluctuations here are essentially thermal in origin, despite the rheology being clearly glassy in this regime (as determined from the strain rate dependence of the flow stress).

To investigate the dynamical correlations present in the stress-strain curves and check these for isomorph invariance, we consider the autocorrelation function of the shear stress, plotted as a function of strain interval. Figure 4.5 shows the results. The collapse is not as good as we have seen in the flow stress. While the curves are somewhat noisy, inspection of the curves shows a trend where the decorrelation moves to lower strain intervals as density increases along the isomorph. To illustrate this more clearly, we fit the autocorrelation curves to a compressed exponential

$$C(\delta\epsilon) = A\exp[-(\Delta\epsilon/\epsilon_c)^{\beta}] \tag{4.6}$$

where β is greater than unity. For $\beta < 1$ this function is known as a stretched exponential, typically used to fit time dependent relaxation correlation curves in the dynamics of supercooled liquid. The characteristic strain ϵ_c corresponds to the relaxation time τ in time-dependent correlation functions, indicating roughly the strain interval after which a stress fluctuation has decayed away. As shown in Fig. 4.5, the compressed exponential expression can fit the main part of the decay reasonably well, but not the initial slow decay or the negative portion at long times, with values of the characteristic strain ϵ_c falling in the range $0.01 - 0.035$ and values of the compression exponent β in the range $1.3 - 1.5$. Figure 4.6 shows that along the isomorphs, ϵ_c

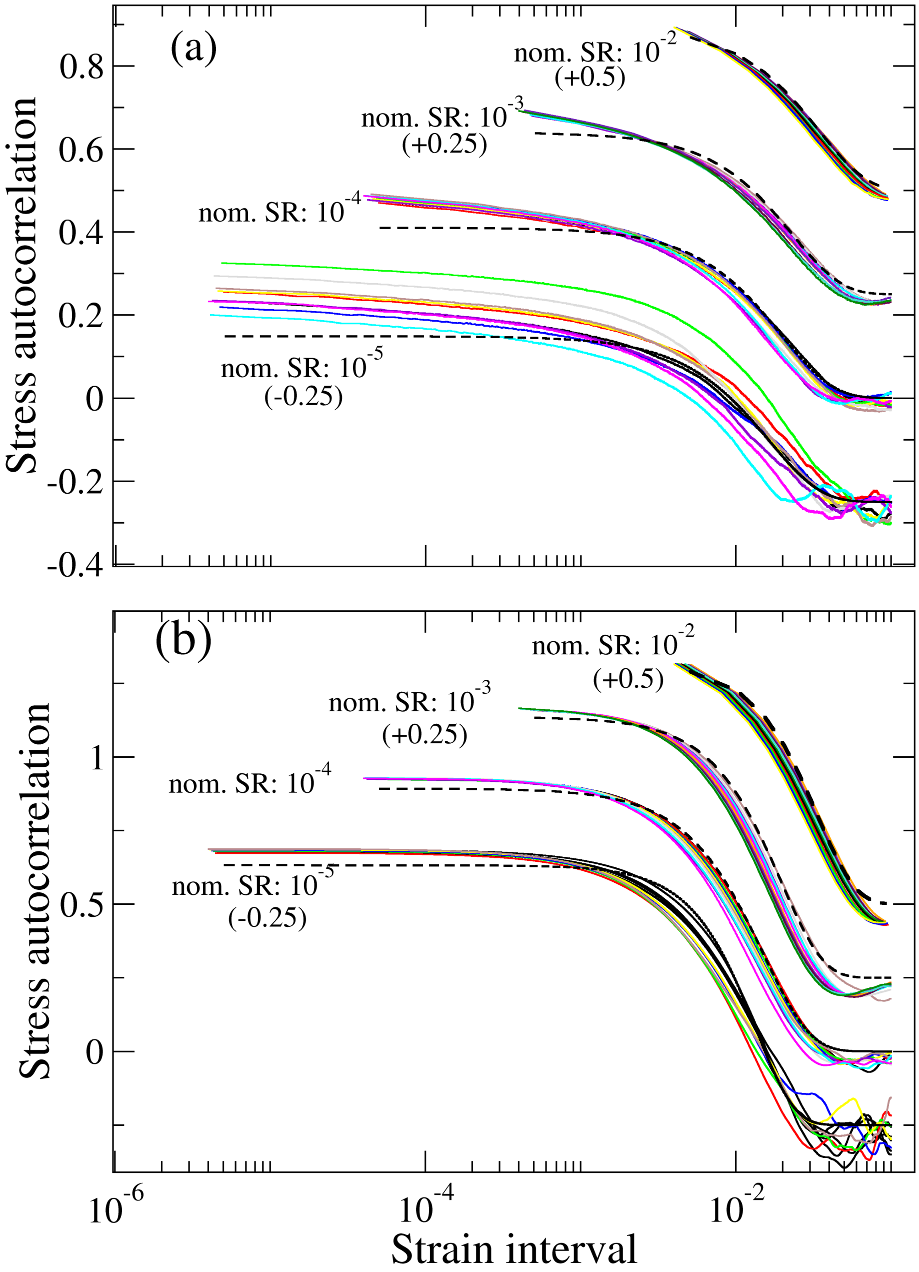

Figure 4.5: Normalized shear stress autocorrelation functions along the high (a) and low (b) temperature isomorphs for three different strain rates. Curves have been shifted for clarity. The dashed lines indicated fits using a compressed exponential function for the first curve in each set (lowest density and temperature); the parameters can be seen in Fig. 4.6.

decreases approximately linearly as density increases, in a similar manner for both isomorphs, while β increases slightly for the high-temperature isomorph but shows little variation on the low-temperature isomorph. Comparing different strain rates, both ϵ_c and β decrease as strain rate decreases, although for β the effect is weak compared to noise. Further investigation with longer runs will be necessary to determine if the apparent variation of ϵ_c is an artifact of insufficiently long runs, a sign of an imperfect procedure for generating isomorphs, or a genuine limit of isomorph invariance (which is never exact). We note also that there seems to be a systematic undershoot to negative correlation, after most of the stress has decorrelated. This could tentatively be interpreted as a sign of avalanche-type dynamics (discussed below).

As a further type of statistical analysis of the stress-strain curves we attempt to infer something about the microscopic processes by considering the distributions of stress changes $\Delta\sigma$ over a given interval of strain $\Delta\epsilon$. Unlike the case of athermal, infinitely slow driving (quasi static) also called AQS simulation that has been studied by several authors[92, 93, 94, 3, 83, 84, 85], it is not possible to unambiguously identify single flow events or so-called avalanches, since thermal fluctuations tend to merge them together. Lemaître *et al.* have shown, however, that the dynamics of a glassy system can still be understood in terms of avalanche-type behavior at relatively high temperatures, up to around $0.75T_g$[17, 18]. This would put our high-temperature isomorph outside the avalanche-dominated regime and our low-temperature one well within it. Indeed, visual inspection of the stress-strain curves for lower strain rates and lower temperature shows drops in the stress reminiscent of avalanche behavior [see Fig. 4.3b]. The distribution of stress changes over a given strain interval can be used to identify signatures of avalanche behavior without having to identify precisely when avalanches occur.

Figures 4.7 and 4.8 show histograms of the reduced unit stress changes $\Delta\tilde{\sigma} = \delta\sigma/\rho k_B T$, for different strain intervals $\Delta\epsilon$ and different strain rates, from simulations

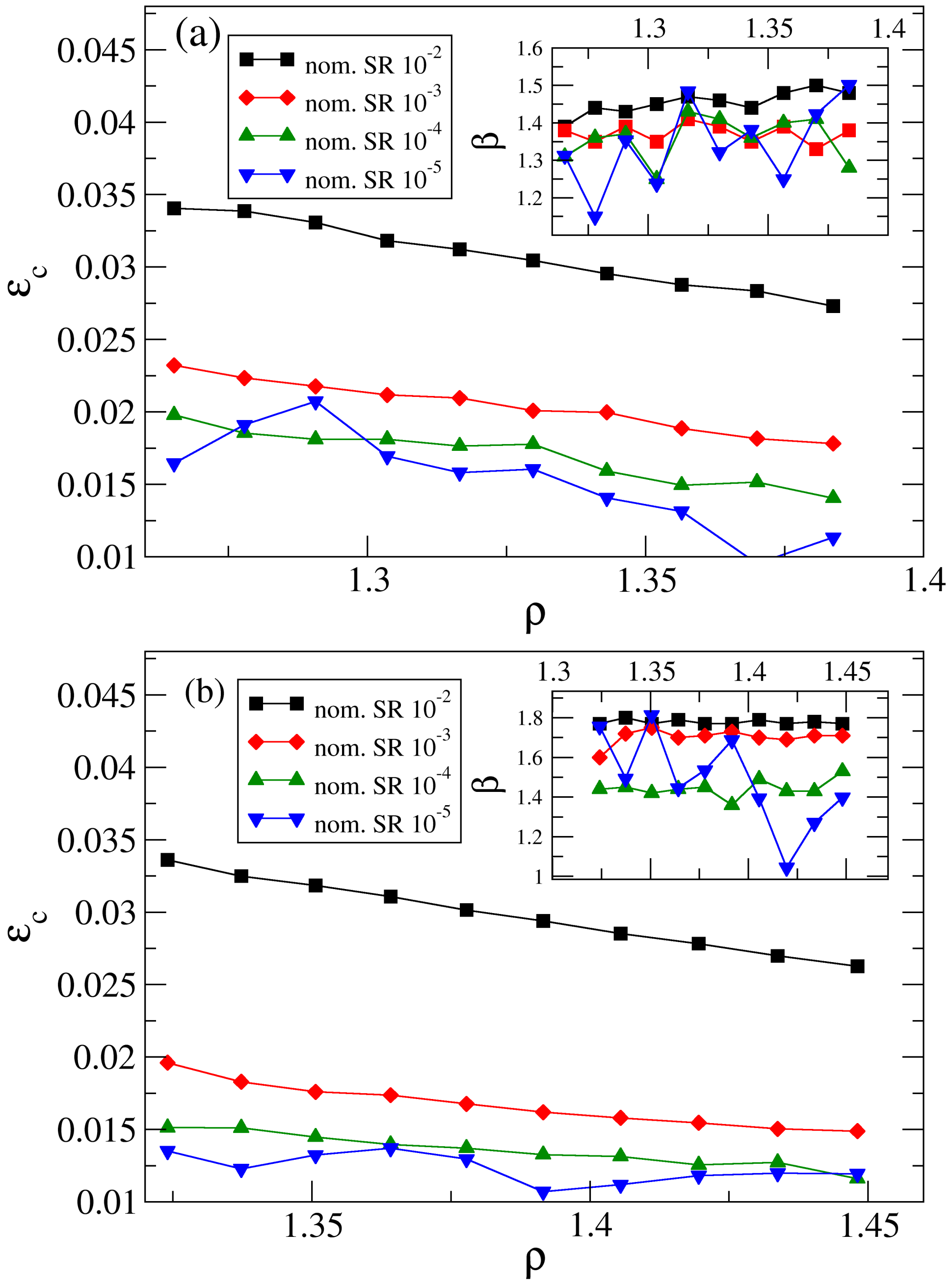

Figure 4.6: Fits of shear stress autocorrelation to Eq. (4.6) shown as functions of density along the high (a) and low temperature (b) isomorphs. The characteristic strain over which decays occurs, ε_c, decreases approximately linearly as density increases.

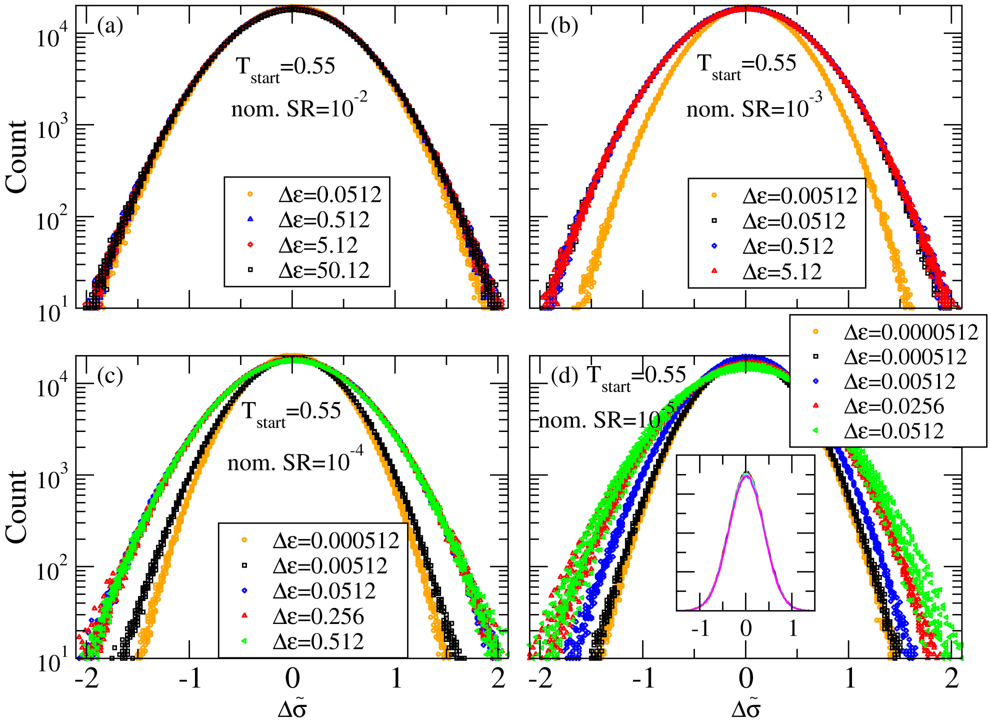

Figure 4.7: Histograms of stress changes of intervals as indicated for the high-temperature isomorph for different strain rates. For each strain rate and $\Delta\varepsilon$, distributions from the ten members of the isomorph are plotted in the same color. The fact that they appear as one curve for each color, apart from broadening due to statistical noise at the lowest strain rates, indicates a high degree of collapse. The distributions are essentially Gaussian for all strain rates and strain intervals $\Delta\varepsilon$, and their widths are relative insensitive to $\Delta\varepsilon$ even at the lowest strain rates, indicating that most of the fluctuations are thermal rather than strain-driven. The inset in (d) shows an alternative way of exhibiting isomorph invariance for $\Delta\varepsilon$=0.000512 by coloring different members of the isomorph differently, and on a linear scale.

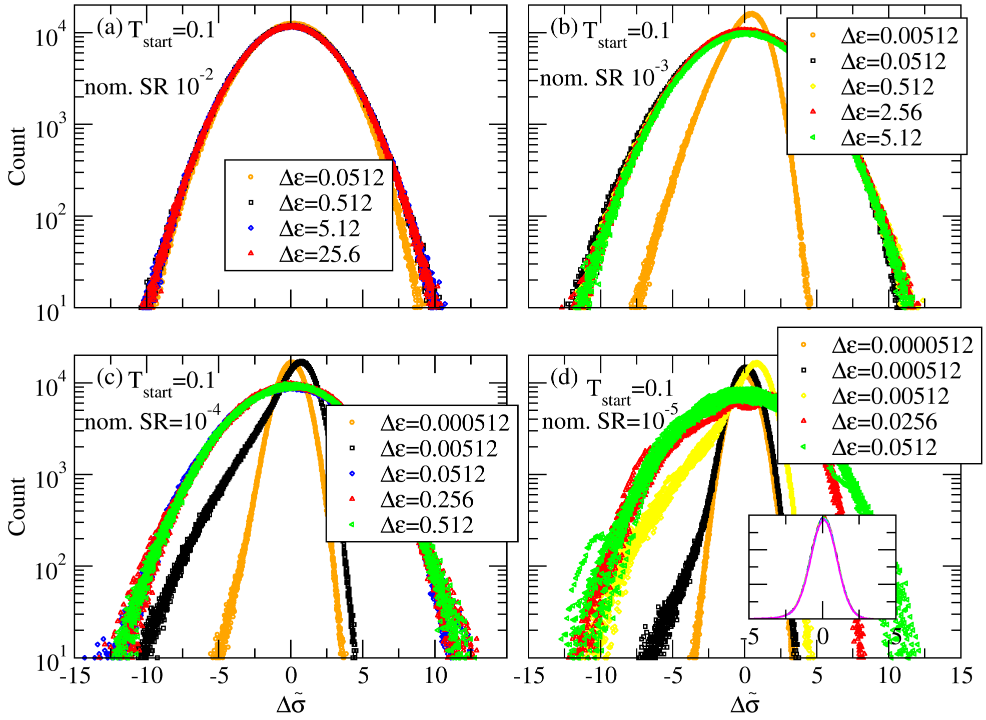

Figure 4.8: Histograms of stress changes of intervals as indicated for the low-temperature isomorph for different strain rates. As in Fig. 4.7 distributions for a given strain rate and strain interval, but different members of the isomorph, are plotted in the same color. They are Gaussian for the largest strain intervals $\Delta\varepsilon$ as well as for the shortest $\Delta\varepsilon$ at the slowest strain rate, where the contribution of strain to the fluctuations is negligible compared to the thermal contribution. For larger $\Delta\varepsilon$ at the slowest strain rate an exponential tail on the negative side is a clear indication of plastic events organizing into avalanches. For even larger $\Delta\varepsilon$, and at the larger strain rates, mixing of thermal and mechanic noise, and multiple avalanches lead to more disorganized histograms. The inset of (d) shows on a linear scale distributions of the second smallest strain interval with the different members of the isomorph represented with different colors as an alternative check of the invariance.

on the high- and low-temperature isomorphs, respectively. Curves of the same color represent data from different state points on the isomorph, *i.e.* each color contains results from 10 configurations along the isomorph. The near collapse shows that the statistics as probed by these histograms are isomorph invariant to a high degree. This can be seen more explicitly in the insets of Figs. 4.7(d) and 4.8(d), where the distributions for the different members of the corresponding isomorph are shown in different colors, for one particular strain interval. Having demonstrated isomorph invariance, it is interesting to note some of the other features of these data. One feature common to both isomorphs and all strain rates is that for sufficiently large $\Delta\epsilon$, over 0.05, the histograms converge to a Gaussian whose variance is twice that of the stress fluctuations (mostly within 1%, 10% for the slowest two strain rates at the lower temperature isomorph, where the statistical errors are larger). This is expected since our analysis of the autocorrelation indicates that correlations vanish by strain 0.05 in all cases (see Fig. 4.5) (the characteristic strain interval for decay is between 0.015 and 0.035, with the functions essentially reaching zero by $\Delta\epsilon = 0.05$). For smaller intervals $\Delta\epsilon$ the distribution is generally narrower and reflects contributions to stress fluctuations from the mechanical driving as well as from thermal fluctuations. As noted above, these cannot be necessarily separated, but a reasonably clear picture emerges from considering the dependence on the isomorph, strain rate, and $\Delta\epsilon$.

Focusing first on the high-temperature isomorph, Figs. 4.7(a)–(d) show stress change histograms for strain rates 10^{-2}, 10^{-3}, 10^{-4}, and 10^{-5}, respectively. For all strain rates the distribution converges to the same Gaussian at large intervals $\Delta\epsilon$. This is consistent with the bottom left panel of Fig. 4.4, which showed that the fluctuations of the stress-strain curve are independent of the strain rate (as well as being isomorph invariant) in the high-temperature case, a sign that the fluctuations are dominated by thermal noise in this regime. For the high strain rate $\Delta\epsilon = 0.05$, so we see no dependence on the interval here. Some dependence on the strain interval can be seen at low strain rate where the width of the distribution appears to converge to a lower value in the limit of small strain intervals. The timescale for the shortest interval is of order 5 Lennard-Jones units (at the lowest-density point on the isomorph), which should be still somewhat longer than the vibrational timescale; therefore this apparent limit presumably represents the full thermal contribution to the fluctuations for an undeformed glassy system. The increased width at high intervals can therefore be interpreted as coming from the sampling of different glassy configurations due to deformation. Note that this would presumably also happen even without any deformation by waiting long enough for liquid dynamics to become relevant; in that case time, rather than strain, becomes the relevant parameter.

Figure 4.8 shows histograms for the lower-temperature isomorph and the same nominal strain rates as Fig. 4.7. More interesting behavior is apparent at these low temperatures, particularly at the lowest strain rates, for example (nominal) 10^{-5}: For the shortest intervals we see a Gaussian, representing purely thermal fluctuations, which are small at this temperature. In other words, for a strain interval of 0.00005 the stress change due to driving is hidden by the thermal fluctuations. As discussed above, we see a Gaussian at the largest intervals where all correlations have decayed. For intermediate strain intervals, however, a marked deviation from Gaussian behavior appears in the form of a roughly exponential tail on the negative side. This is a clear indication of avalanches: correlated aggregations of multiple microscopic flow events which release the stress, giving large negative stress changes, as studied in the quasistatic case[92, 93, 94, 3, 83, 84, 85].

An analysis somewhat similar to ours was carried out by Rottler and Robbins[115], who also found exponential tails at low temperature and strain rate. Note that since we consider a steady-state situation, the mean of the stress changes must be zero, implying that the main Gaussian is shifted slightly to positive values. We have checked this by fitting the Gaussian part. The positive mean of the nonavalanche fluctuations

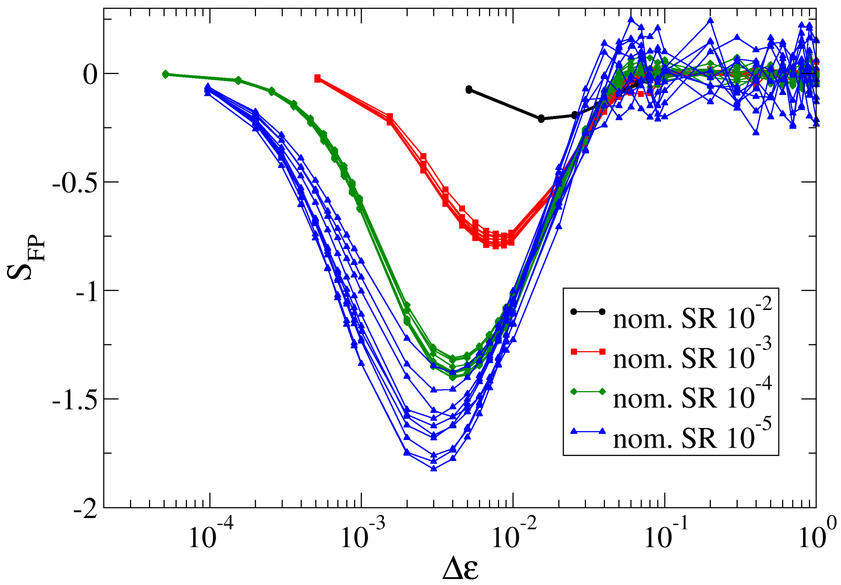

Figure 4.9: Fisher-Pearson skewness S_{FP} of (reduced) stress drop distributions as a function of strain interval for different strain rates for the low-temperature isomorph. Different curves of the same color correspond to different points on the isomorph.

corresponds to elastic loading which is then released by the avalanches. In the limit of zero temperature and then infinitely slow deformation[94], the narrow Gaussian seen at short intervals would converge to a δ function at a small positive value (the shear modulus times the strain interval).

The asymmetric deviations from Gaussianity can be quantified by the Fisher-Pearson coefficient of skewness, based on the third moment of the distribution scaled by the cube of the standard deviation

$$S_{FP} = \frac{m_3}{m_2^{3/2}} \tag{4.7}$$

where

$$m_i = \frac{1}{N} = \sum_{n=1}^{N} (x_n - \bar{x})^i \tag{4.8}$$

where $\bar{x}$ is the sample mean. Figure 4.9 shows S_{FP} as a function of strain interval

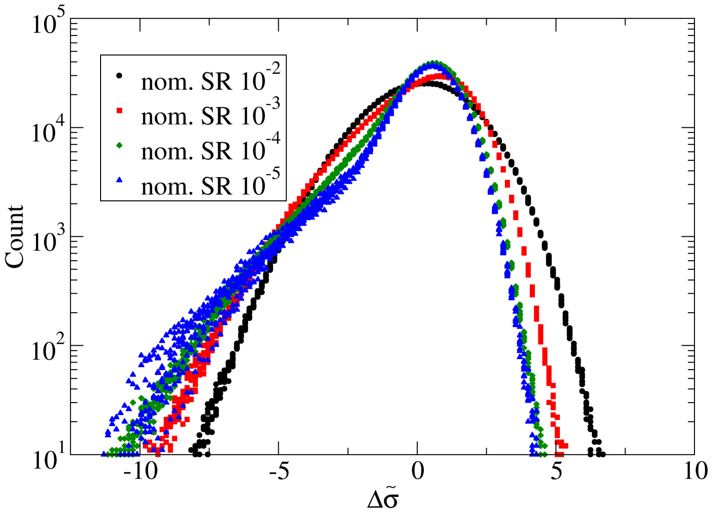

Figure 4.10: Histograms of (reduced) stress changes over strain intervals ε_s chosen to minimize skewness for each strain rate, on the low temperature isomorph. Data for different points on the isomorph are plotted in the same color for each nominal strain rate. In order of decreasing strain the minimum-skew strain intervals, as judged by eye from Fig. 4.9, are 0.02, 0.008, 0.004, 0.003.

for four different strain rates along the low temperature isomorph. Different curves with the same color come from different members of the isomorph for a given strain rate. The skewness vanishes for short and long strain intervals where, as discussed above, the distributions become Gaussian. The variations between the distributions for a given strain rate are not systematic and thus presumably reflect statistical uncertainty. The variation is relatively small and thus consistent with this measure of the dynamics being isomorph invariant (this follows of course also from the good collapse of the distributions in Figs. 4.7 and 4.8). The minimum (most negative) value of the skewness parameter identifies a strain interval ϵ_s at which the deviation from Gaussianity is most pronounced. Histograms for this strain interval are plotted in Fig. 4.10 for the low-temperature isomorph and different strain rates, with the values of ϵ_s given. These values are a factor of $2-3$ smaller than the characteristic strain intervals identified from the autocorrelation functions (see Fig. 4.6). For the lowest strain rate it is an order of magnitude larger than the strain interval at which the exponential tail indicating avalanche behavior is seen, 5×10^{-4} (see Fig. 4.8). Denoting the latter by ϵ_a (where a denotes avalanche), we can tentatively identify, in the low-temperature low strain-rate limit at least, a broad hierarchy of strain scales which characterize different physical processes: (i) the smallest strain scales where stress fluctuations are purely thermal or vibrational; (ii) the avalanche strain ϵ_a over which stress changes show signs of correlated avalanche-type behavior, of order 5×10^{-4}; (iii) the strain over which stress change distributions deviate most from Gaussianity ϵ_s an order of magnitude larger than ϵ_a, where the exponential tails of the avalanches and the changes due elastic loading between them merge to make a broader distribution, but signs of correlation remain; (iv) the characteristic strain ϵ_c identified via the stress autocorrelation function, where ϵ_c is of order 2×10^{-2}, which is a small factor $(2 - 3)$ larger than ϵ_s; and (v) the strain interval around 5×10^{-2} beyond which all correlation has vanished (though this is not physically independent of ϵ_c; rather it represents where the autocorrelation function is small compared to $1/e$).

4.3.2 Particle Dynamics under Shear

We also check the invariance of particle dynamics under shear in the steady state by looking at the transverse diffusivity. Accounting for the contribution to a particle's displacement in the shearing direction when using Lees-Edwards boundary conditions is nontrivial[79], so we consider only the components of a particles displacement transverse to the shearing direction. Based on these displacements, we compute the self-intermediate scattering function (ISF) and the mean square displacement (MSD). For the ISF one must choose a wave number q, which, as is conventional, we choose to be near the first peak in the structure factor $S(q)$. This must be of course scaled according to $\rho^{1/3}$ along an isomorph such that the reduced wave number

$\tilde{q} \equiv q\rho^{-1/3}$ is constant [this is compatible with choosing q to be near the first peak, as $S(q)$ is invariant in reduced units][51]. We restrict consideration to the larger (A) particles for brevity. The ISF is shown in Fig. 4.11.

For both isomorphs and all strain rates we find a good collapse, though slightly less so for the lowest strain rates. Fitting of the curves to a stretched exponential form [Eq. 4.6, where $\beta < 1$ and with τ instead of ϵ_c], indicates at most a slight systematic variation in relaxation time τ, suggesting the apparent failure to collapse perfectly is mostly due to statistical error. From the fits, for the high-temperature isomorph we find near-exponential behavior ($\beta \simeq 1$) for the highest strain rates and mildly stretched exponential behavior as the strain rate decreases ($\beta \simeq 0.85$ at the lowest strain rate). For the low-temperature isomorph we find near-exponential behavior for all strain rates. Stretched exponential behavior is typical of dynamics in the supercooled, highly viscous liquid. The vanishing of stretching, *i.e.*, the near-exponential behavior, at low temperatures and slow shearing indicates that the nature of particle dynamics is different in this regime. Exponential behavior of the self-intermediate scattering function for the same system under shear in the limit of zero temperature was also reported by Berthier and Barrat[11].

Plots of the mean-square transverse displacement in reduced units are shown in Fig. 4.12. The form of the curves is reminiscent of what is seen for equilibrium viscous liquids: a ballistic regime at short times (where the slope is 2), a plateau of varying extent, followed by a transition to diffusive behavior (slope 1). The collapse is good in all cases, although again some deviations are apparent for the lowest strain rates, particularly around the crossover to diffusive behavior. Superficially, not much difference can be seen between the low- and high-temperature isomorphs, but upon closer examination one can see some physically relevant differences (see Fig. 4.13). On the higher-temperature isomorph thermal motion is greater; thus the height of the plateau (in units of the interparticle spacing) is larger. More interestingly, in

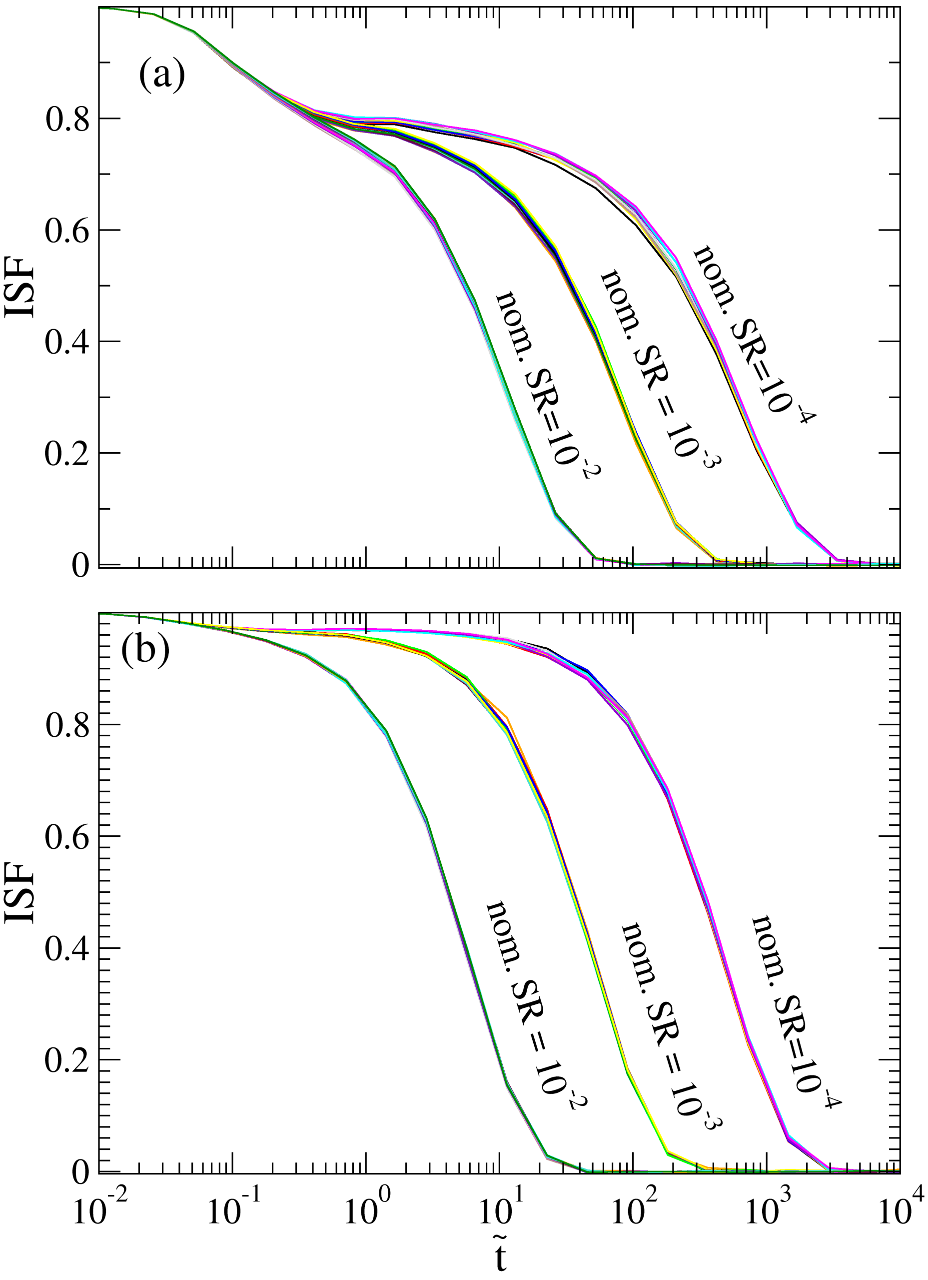

Figure 4.11: Self-part of the intermediate scattering function for larger (A) particles based on particle displacements transverse to the shearing direction for (a) the high temperature isomorph and (b) the low temperature isomorph, for different strain rates.

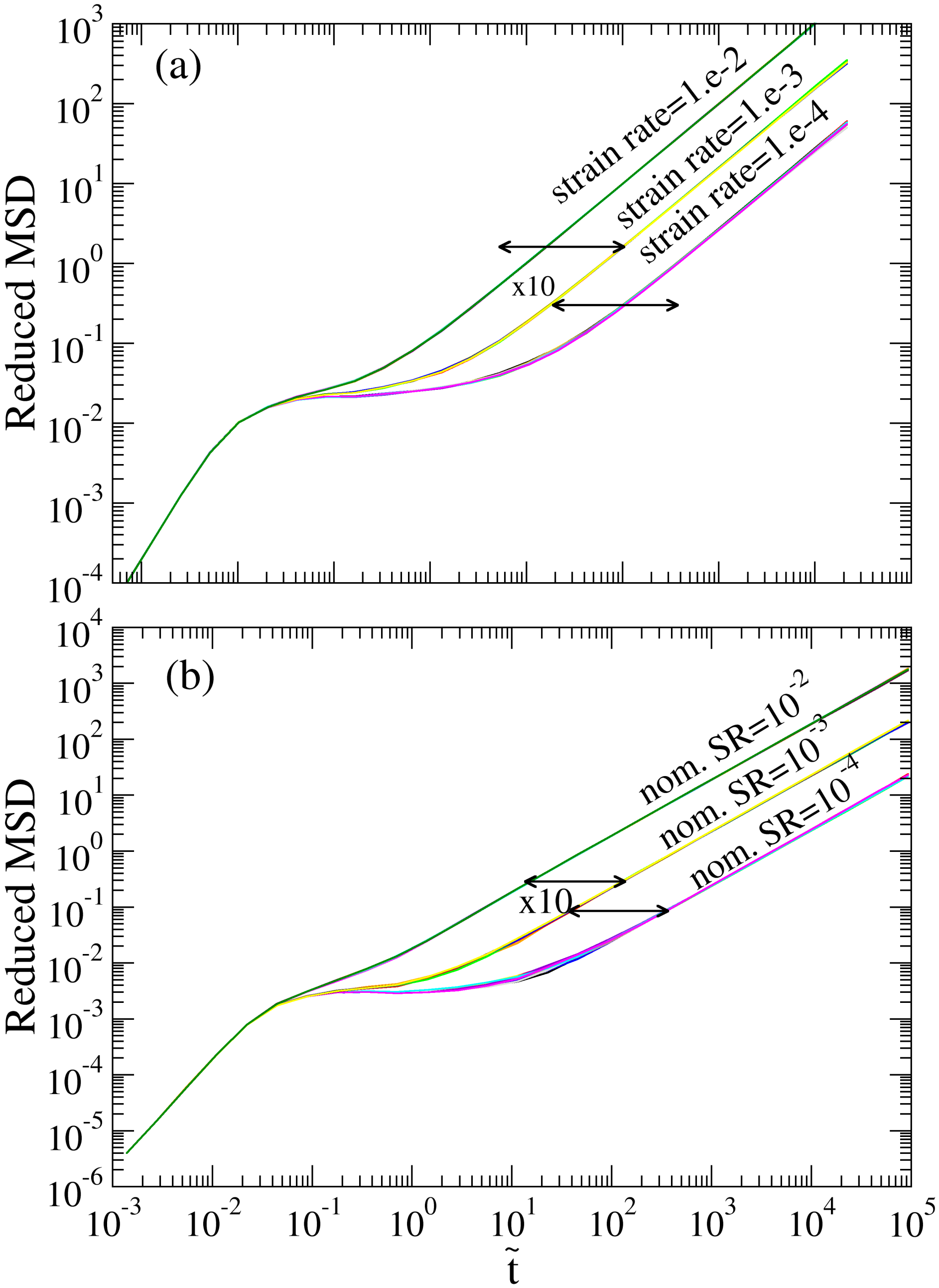

Figure 4.12: Mean squared transverse displacement plotted in reduced units for (a) high temperature isomorph and (b) low temperature isomorph. The horizontal arrows indicate a factor of ten in the time axis, and can be used to judge by what factor the curves can be shifted onto each other in time.

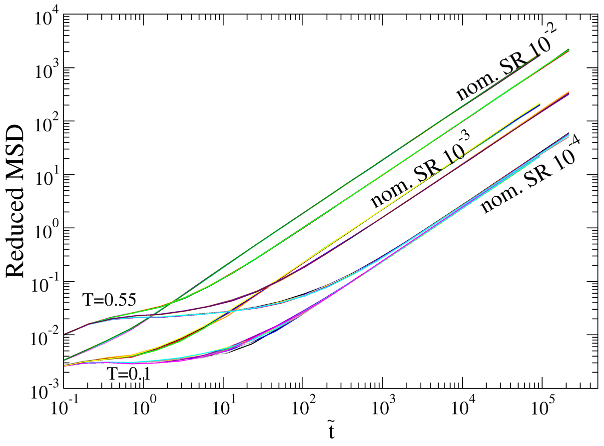

Figure 4.13: The MSD curves from Fig. 4.12 (a) and (b) plotted together, though without the short-time parts. At low strain rates the MSD appears to become independent of isomorph, as well as which point on the isomorph. The definition of reduced units means that the curves for the different isomorphs are plotted in terms of different time scales, so caution is required when drawing conclusions from the apparent collapse.

the low-temperature case, the diffusivity curves are essentially a factor of 10 apart in the time axis, corresponding to the factor 10 change in strain rate, while for the high-temperature case the diffusivity curves are shifted by a factor smaller than 10 on the time axis. The interpretation is that thermal activation plays a noticeable role in particle diffusion in the high-temperature case, but almost no role in the low-temperature case. In the latter the diffusive motion is determined entirely by the strain rate at the lowest temperatures. Figure 4.13 emphasizes the long-time parts of the MSD for both isomorphs. In this plot the difference at long times between the two isomorphs appears minimal; the MSD is determined much more by the strain rate than by which isomorph is considered (and almost not at all by which point on the isomorph, which is the essence of isomorph invariance). It must be noted, however, that direct numerical comparison of the MSD curves at different temperatures (isomorphs) for the same nominal strain rate can be difficult to interpret due to the use of reduced units; thus it appears that at nominal strain rate 10^{-2} the diffusivity, counterintuitively, is greater on the lower temperature isomorph. Recall, though, that this is in reduced units, *i.e.*, with respect to a timescale defined by the thermal velocity. A meaningful comparison would first of all involve identical reduced (rather than nominal) strain rates; the reduced strain rates for the low-temperature isomorph are a factor of 2.3 higher than the corresponding ones for the high-temperature isomorph. Second, there is a further complication already alluded to, which will be discussed further below, namely, that the definition of reduced units is not unique and a different choice could in principle be more relevant, and elucidate the physics better, in the limit of low temperatures. We emphasize that the most important result in this section is the near perfect collapse of the MSD for different state points along a given isomorph (and given reduced strain rate), when reduced units are used.

Lemaître and co-workers have studied over several papers the effect of finite temperatures and strain rates on avalanche dynamics[80, 17, 18]. They found that studying transverse particle diffusivity is useful for disentangling the effects of strain and temperature. In particular, Chattoraj *et al.*[18] used the transverse diffusivity D determined from the long-time limit of the MSD curves and its strain-normalized analog $D/\dot{\gamma}$. Their Fig. 5 shows nicely the crossover from strain-dominated to temperature-dominated diffusion. As they pointed out, the strain-normalized diffusivity is the more relevant one in the strain-driven regime (low temperatures and strain rates), while normal diffusivity is relevant at high temperatures. Moreover, they showed that the crossover strain rate as a function of temperature tracks more or less the inverse relaxation time: Strain begins to have a pronounced effect on particle diffusion once the strain per relaxation time exceeds an amount of order $10^{-3} - 10^{-2}$. Our results are consistent with theirs in terms of the interplay of strain-driven and thermal contributions to particle motion. They did not consider density as a parameter, but our results show that it can be simply accounted for through isomorph invariance and by remembering that "at high temperature" really means "on high-temperature isomorphs."

4.4 Implication for Alternative Reduced Units

Our definition of reduced units, apart from the length unit, is based on thermal motion; thus the energy scale is $e_0 = k_BT$, the velocity scale is $v_0 = (k_BT/m)^{1/2}$, and the timescale is the time for a particle with such a constant velocity v_0 to cross the interparticle spacing, $t_0 = \rho^{-1/3}(k_BT/m)^{-1/2}$. This choice has the advantage of using only macroscopic parameters; apart from the particle mass, no knowledge about the system under consideration (its Hamiltonian, phase diagram, or isomorphs) is needed. However, as noted above, this definition becomes problematic as temperature approaches zero; it is natural at finite temperature but not in the limit of zero temperature, where the thermal timescale diverges. A vibrational timescale which is well defined in that limit is preferable. Noting that the definition of reduced units must satisfy the condition that the reduced quantity is still constant along isomorphs, we can define a new energy scale $e_1 = e_0h(\rho)/k_BT = h(\rho)$ and timescale $t_1 = t_0(h(\rho)/k_BT)^{-1/2} = \rho^{-1/3}[h(\rho)/m]^{-1/2}$. These are independent of T and therefore suitable for use in the limit $T \to 0$. From the interpretation of $h(\rho)$ in terms of the curvature of the pair potential at the nearest-neighbor distance[14], we can interpret t_1 as a vibrational timescale for a single neighbor pair. Thus we can introduce an alternative reduced stress, denoted by a circumflex,

$$\hat{\sigma} \equiv \frac{\sigma}{\rho h(\rho)} = \tilde{\sigma}\frac{k_BT}{h(\rho)} \tag{4.9}$$

and alternative reduced strain rate

$$\hat{\dot{\gamma}} \equiv \dot{\gamma}\rho^{-1/3}[h(\rho)/m]^{-1/2} = \tilde{\dot{\gamma}}(\frac{k_BT}{h(\rho)})^{1/2} \tag{4.10}$$

We stress that for the purpose of checking for isomorph invariance of a quantity the choice of which system of reduced units is not important except for practical purposes, e.g., when $T = 0$. However, it can become relevant when comparing different isomorphs in order to identify the relevant physics. Another example is the comparison of flow stress shown in Fig. 4.4, where the strong temperature dependence of the reduced flow stress was partly ascribed to our choice of reduced units. Using $\rho h(\rho)$ instead of $\rho k_B T$ would probably reduce this variation and is potentially therefore more relevant for the glassy regime. Thus the advantages of one choice over the other are potentially greater clarity, insight, or ease of interpretation.

Lerner and Procaccia studied the flow stress for simulated glasses under steady-state conditions covering both finite temperatures and the athermal limit [82], using a scaling theory based on the approximation of their pair potential by an inverse power law. Their system is modeled using an approximate inverse power law potential, which means that $h(\rho)$ is approximately a power law ρ^{γ} , in their notation $\rho^{\nu-1}$. Noting that their exponent ν corresponds to our $\gamma + 1$, all their scaling expressions are in fact compatible with isomorph theory, once one recognizes that their choice of time scaling is equivalent to our alternative reduced units. Our point in the present discussion is that there is a choice of which system of reduced units to use and that that choice is related to how relevant physics is best revealed. It is analogous to the choice of whether we study the standard diffusivity based on mean square displacement as a function of time or the strain normalized diffusivity based on the mean square displacement as a function of strain[18]. We note again, however, that using $h(\rho)$[62, 13] is less straightforward than $k_B T$ because it depends on the potential and is not directly available in the simulation. In some cases, including the Kob-Andersen system used here, it is known analytically[62, 14]; otherwise it must be identified from the shape of the numerically determined isomorph before conversion into reduced units can take place.

4.5 Conclusion

We have simulated isomorphs for the Kob-Andersen binary Lennard-Jones glass and compared their static structure and their dynamics under steady-state shearing deformation. Two isomorphs were generated using the potential energy and virial fluctuations during an NVT simulation (no shear), assuming that aging effects could be ignored. This is probably a reasonable assumption for the lower-temperature isomorph, but this is less clear for the high-temperature one, which is only a few percent below the conventional mode-coupling temperature for this system and therefore can be equilibrated as a liquid with longer (but still feasible) simulation times than we have used here. Nevertheless, excellent collapse of the radial distribution function is observed and good collapse for most of the dynamical measures. The worst collapse is observed for the shear stress autocorrelation function, which exhibited a systematic variation of the characteristic decay strain along an isomorph. Better statistics, *i.e.*, longer runs, would probably help, but a more careful determination of the correct isomorph might be necessary, as it could be that this quantity is simply more sensitive to deviations from the correct isomorph than the others we have investigated. Going beyond simply checking for isomorph invariance, we have analyzed the distributions of stress changes over different strain intervals. We showed that different features emerge according to whether purely thermal effects are visible or avalanches, as indicated by an exponential tail in the distribution, or more complex and extremely non-Gaussian distributions at larger strain intervals which include multiple avalanches. Isomorph invariance is clear in all the data presented for this analysis. In comparing the mean square transverse particle displacements, in addition to almost perfect isomorph invariance, we noted how the MSD curves apparently become independent of temperature in the limit of long times, but also that one has to be careful to compare the same reduced strain rates. We note that no noticeable difference in the quality of the isomorphs is observed, despite the lower-temperature isomorph showing lower values of the correlation coefficient R (see Table 4.1). We also showed how the existence of isomorphs can inform and constrain the development of analytical theories for how, for example, the flow stress can depend on density, temperature, and strain rate. In addition, an alternative definition of reduced units emerged, the full implications of which are left for future work.

Chapter 5

Isomorph theory on sheared glassy systems: Part II

After chapter 4, we also investigate the extent to which the transient part of the stress strain curves is invariant when the thermodynamic state point is varied along an isomorph. In this chapter, the shear deformations are carried out on glass samples of varying stability, determined by cooling rate, and at varying strain rates, at a state point deep in the glass. Density changes up to and exceeding a factor of two are made this time (10% in previous chapter). The temperatures for these higher densities were chosen to give state points isomorphic to the starting state point by requiring the steady state flow stress for isomorphic state points to be invariant in reduced units. We compare the performance of different methods to obtain the isomorphic temperatures for such a large density span. After finding the corresponding isomorph, we show however that the peak stress on the stress strain curve is not invariant, but decreases by a few percent for each ten percent increase in density, although the differences decrease with increasing density. We can rationalize this behavior by considering how different parts of the potential energy landscape scale differently under changes of density.

Same RUMD package discussed previously is used for simulation in this chapter.

5.1 Introduction

Background information can be found in chapter 1 and 4. We here are more ambitious in terms of density changes since unlike the standard numerical method we used in chapter 4, a recently defined “force method” (defined below in section 5.3) is able to allow for large changes in density without having to simulate many small density changes in between. Our second investigation here thus involves a much larger density range so as to perform a systematic check on the performance of various methods to find the isomorph. We compare five methods by checking the matching of reduced mean steady state stress, i.e. the reduced flow stress. Although they all give similar results for a small density change, the difference between them grows with increasing density. None of them can match the reference reduced flow stress within errors for the largest density. We hence turn to a pragmatic approach to determine isomorphic temperatures, which is the best empirically determined isomorph whose reduced flow stress matches that at the reference density.

With the isomorph we find, shear then is applied in the same way as in last chapter. But here one important feature of the non-steady state regime is that the thermal history of the glass prior to deformation becomes relevant. Therefore, our glasses are now prepared by cooling at different fixed cooling rates, and at fixed density from a given temperature at the lowest density considered. Any deformation simulation is characterized by four parameters: the density ρ, temperature T, cooling rate R_c and strain rate $\dot{\epsilon}$. Since we focus on trying to identify isomorphs, density and temperature are varied according to the (putative) isomorph, and cooling rate always refers to the initial (low) density in real units, while strain rate is referred to using reduced units (isomorph invariance can only be expected when the strain rate is fixed in reduced units). Each glassy configuration is sheared with various strain rates. We find that the isomorph works well for all cooling rates in terms of matching the reduced flow stress. While good invariance is verified for the reduced flow stress, the peak stress shows a decreasing trend against density along the isomorph for all cooling rates and strain rates we check. We explain such non-isomorphic behavior through checking the local spatial homogeneity of strain profile at the transient state.

5.2 Simulation

First some details of our simulation. It should be noted here that one important feature of working on the transient part of the stress and strain curve is that the fluctuations cannot just be averaged out by running longer simulations. Even though the temperature we study here is not as low as in chapter 4, the fluctuations in the stress are still quite severe and avalanche-like. To manage the fluctuations we use 10 times larger system size and run multiple independent runs, starting from an ensemble configurations generated by separate cooling runs. Studying the run-to-run deviations also allows us to determine errors on flow stress and peak stress quite precisely.

The details are the following. We work on the same KABLJ system as last chapter but with 10000 particles. Here we cool the system after equilibrium at $T = 1$ using three different cooling rates 10^{-5}, 10^{-6}, and 10^{-7} with NVT simulation instead of NPT. Note that here the cooling rate $\dot{T}$ is in Lennard Jones (LJ) units (see previous chapter for definition). We focus on one starting temperature 0.3 here that is not too deep in glassy state nor close to the liquid state, as shown in Fig. 4.1. For these three cooling rates, we create an ensemble containing 40 similar configurations at $T = 1$ (picked from one NVT simulation at $T = 1$ in equilibrium but are well separated in time so that the 40 can be considered equivalent but nonetheless statistically independent) and then cool them in the same way. Therefore, we have 120 configurations at $T = 0.3$, 40 for each of the three cooling rates. Unlike chapter 4, here we compare different methods to generate isomorph and choose one that works best for our purpose for all cooling rates. Again, the isomorph contains 10 points, along which the density of each point is 1.1 times of the previous point (1.01 in the previous chapter). For each configuration, we then apply shear with three different reduced strain rates $\tilde{\dot{\gamma}} = 10^{-3}, 10^{-4}, 10^{-5}$ and simulate up to strain $\epsilon = 4$, for all 10 isomorph points. We also choose the time step to be fixed in reduced units, which is practical–it automatically ensures that a time step which is stable at one density and temperature will be stable along the isomorph. The time step is 0.004 (LJ units) at the lowest density 1.183.

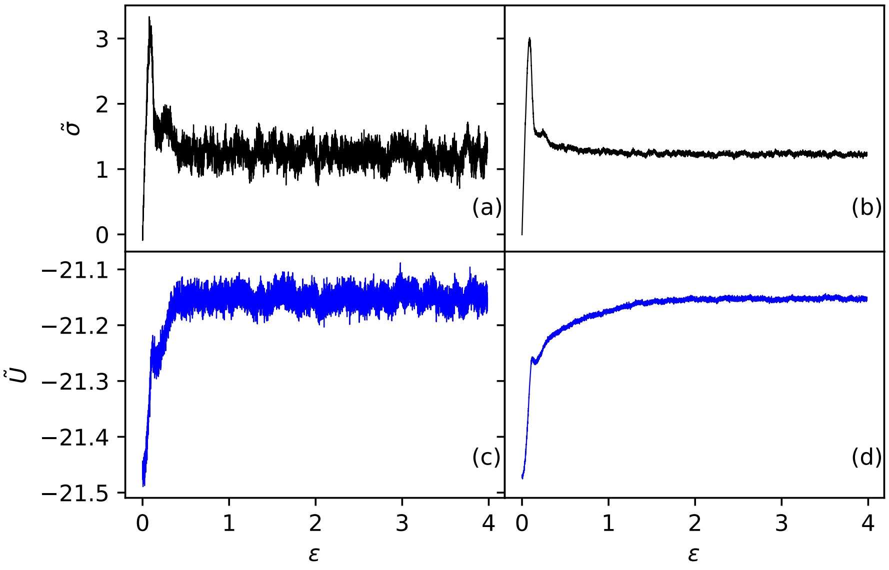

Figure 5.1: Examples of reduced-unit shear stress (top panels) and potential energy per particle (bottom panels) versus strain, from shear deformation of a binary Lennard-Jones glass with density 1.183 at temperature 0.3. The glass was prepared by cooling at the rate 10^{-7} (LJ units), while the deformation was carried out at reduced strain rate 10^{-5}, meaning the real strain rate was $10^{-5}\rho^{1/3}(T)^{1/2} \simeq 5.8 \times 10^{-6}$. The left panels show curves from a single run, while the right panels show the average of 40 independent runs.

Figure 5.1 shows examples of stress strain curves generated in similar ways as in the last chapter at density 1.183 and temperature 0.3. In this case the cooling rate for the glasses was 10^{-7} in LJ units. While ideally we are interested in investigating to what extent the entire stress-strain curve collapses along a given isomorph (with given cooling and strain rates), for many purposes as well as limitations, it is sufficient to consider (or at least start with) the flow stress and the peak stress, which give us two quantities (always in reduced units) that we can plot as a function of density along isomorphs.

The definitions of the two quantities are the following. Similar to previous study, the shear stress seems to be essentially at its steady-state value by strain 0.5 judged by eyes. However, as shown in panel (d) in Fig. 5.1, for this slowly cooled system the potential energy has not converged to the steady-state value until around strain 2.0 [125]. We hence define steady state as strain between $2-4$ from now on. Our observation on the reduced potential energy versus strain curves confirms this choice for steady state. We find that the potential energy of the slowest cooled configuration under slowest shear gradually reaches the steady state value at a strain between 1 to 2, see Fig. 5.2.

Figure 5.2 shows the potential energy versus strain up to strain 2 for the three cooling rates and the fastest and slowest strain rates. The potential energy can be rather slow in converging to its steady state value, especially for the highest strain rate and lowest cooling rate, where it appears to converge around strain 2. This is despite that the shear stress has typically converged before strain 1. The fact that potential energy must also be monitored to ensure steady state conditions was discussed by Singh *et al.* [125].

We calculate the average of reduced stress in the steady state for each shear simulation. We then use the average of 40 shear runs as the flow stress at the corresponding density, temperature, strain rate, and cooling rate. Error bars is computed as sample standard deviation of the 40 independent flow-stress values divided by $\sqrt{40}$. The

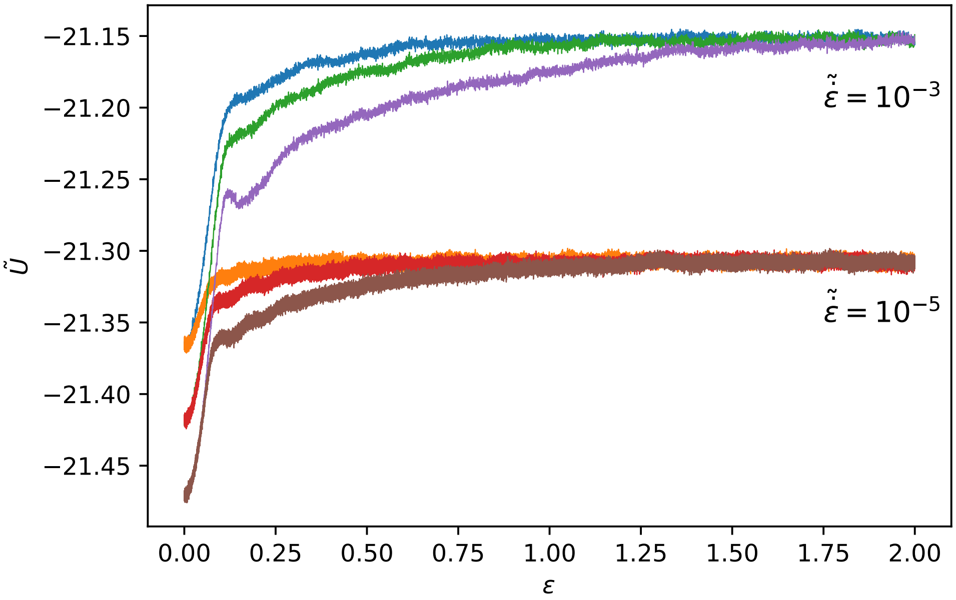

Figure 5.2: Reduced potential energy against strain sheared with the $\dot{\tilde{\epsilon}} = 10^{-3}, 10^{-5}$ for the three cooling rates $|\dot{T}| = 10^{-5}$ (blue and orange), 10^{-6} (green and red), 10^{-7} (purple and brown) at $\rho = 1.183$ and $T = 0.3$. Each curve is an average of 40 simulations.

height of the peak that precedes the steady state, in reduced units, $\widetilde{\sigma_p}$ is determined by fitting the region of the averaged stress-strain curve around the peak to a fourth-degree polynomial. The interval for fitting is the strain with the numerically largest shear stress, plus or minus 0.05. We check that our main results do not vary with this choice of fitting range as long as reasonable amount of data points are included. To estimate the error on the peak height the 40 independent runs were averaged 8 at a time to give five independent stress strain curves, for which the fitting procedure was used to estimate the peak height. The error was then estimated as the sampled standard deviation of the 5 groups divided by $\sqrt{5}$.

Here to set the stage we show flow stress and peak stress at the starting state point first for different strain rates and cooling rates. Let us recall from our results in previous chapter that we do not expect perfect isomorphs, both because isomorphs are never perfect, especially over large density changes, and because the intrinsic fluctuations in the stress can obscure the degree of collapse. Therefore, we need to

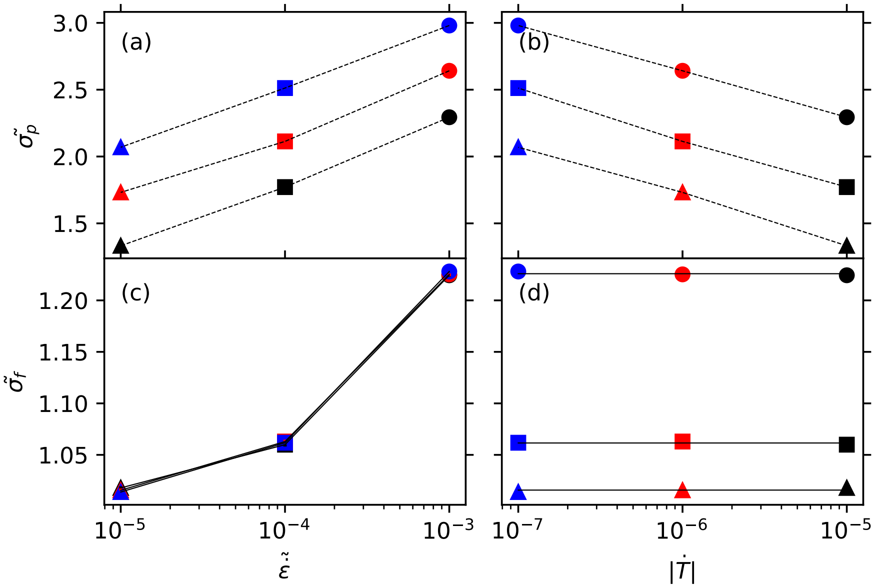

Figure 5.3: Reduced peak stress $\tilde{\sigma}_p$ and flow stress $\tilde{\sigma}_f$ as function of reduced strain rate $\dot{\tilde{\epsilon}}$ (a,c) and cooling rate $|\dot{T}|$ (b,d). Black, red, and blue are for $|\dot{T}| = 10^{-5}, 10^{-6}, 10^{-7}$; sphere, square, and up triangle are for $\dot{\tilde{\epsilon}} = 10^{-3}, 10^{-4}, 10^{-5}$. The $\tilde{\sigma}_f$ is within errors independent of $|\dot{T}|$ but increases with $\dot{\tilde{\epsilon}}$. Each point of $\tilde{\sigma}_f$ is an average of 40 independent shear simulations and we estimate the errors as the standard deviation divided by $\sqrt{40}$. For the peak stress we divide the 40 simulations into 5 groups randomly and obtain 5 averaged stress and strain curves. We then find the strain ϵ_p of the maximum $\tilde{\sigma}_p$ and use $\epsilon_p \pm 0.05$ as the fitting range. A 4th order polynomial is fit and we identify the maximum value of the fit as $\tilde{\sigma}_p$. Each point of $\tilde{\sigma}_p$ is an average of the 5 subgroups and we use the standard deviation divided by $\sqrt{5}$ as the error. The three horizontal lines in panel (d) are the average of the corresponding three points of the same $\dot{\tilde{\epsilon}}$.

be able to compare “approximate invariance” with the variation observed when non-isomorphic changes of parameters are considered. In equilibrium situations varying the temperature and density separately while keeping the other fixed are the only possibilities. In the non-equilibrium case more interesting possibilities arise, namely varying the cooling and strain rates. To show how much variation in rheological properties results from varying these rates we plot the peak and flow stresses in Fig. 5.3, first as a function of strain rate for different cooling rates, and then as a function of cooling rate for different strain rates. It can be seen that an order of magnitude increase in strain rate increases the peak stress by 25-30% [panel (a)] and the flow stress by 5-15% [panel (c)] while an order of magnitude increase in cooling rate decreases the peak stress also 15-20% [panel (b)] but has no effect on the flow stress [panel (d)]. These dependencies are expected in glassy rheology. In particular a lower cooling rate generates a more stable glass, which requires a larger stress to initiate deformation (i.e. it has a larger yield stress).

With this preliminary check on the influence of cooling rate and strain rate in mind, we then move on to generate the isomorph.

5.3 Methods to generate isomorph

In the previous chapter, we only check a small density span such as $1.265 - 1.384$. Here we are much more ambitious and check a density span $1.183 - 2.789$. Here 1.183 is close to the density 1.2 studied by Kob and Andersen and most often by others. We trace the isomorph with an increment of 1% of density at each step before and 10% here. For such large density changes, the accuracy of isomorph generating method becomes important. It is thus of particular significance to evaluate various methods to generate isomorphs first.

In the following we compare different methods, using as a test case glasses cooled

Method	Ensemble	T-ratio	T_2
γ	NVT	1.593	0.4779
γ	SSS	1.609	0.4828
DIC-pe	NVT	1.593	0.4779
DIC-pe	SSS	1.609	0.4827
DIC-sts	NVT	1.595	0.4786
DIC-sts	SSS	1.597	0.4791
FM	NVT	1.653	0.4959
FM	SSS	1.649	0.4947
FM-mod	NVT	1.647	0.4940
FM-mod	SSS	1.637	0.4911

Table 5.1: Comparison of methods for identifying isomorphic temperature upon raising density by 10% from 1.183 to 1.301, for glasses cooled at rate 10^{-5}. SSS refers to steady state shearing, data taken between strains 2 and 4, with reduced strain rate 10^{-3}; NVT refers to NVT simulations of 10^7 steps.

at 10^{-5} (LJ units) and then we apply both NVT at $T = 0.3$ and shearing at $\tilde{\dot{\epsilon}} = 10^{-3}$ (reduced units), and the case of a density increase of 10% from 1.183 to 1.301. We give a quick summary of the results here first and then go through each method one by one below. The results for the temperature scaling factor and estimated temperature at the latter density are summarized in the Table 5.1. Results from NVT simulation data are labeled with “NVT” and from shearing simulation are labeled “SSS”, short for “steady state stress”.

5.3.1 Integration using the density scaling exponent γ

In the previous chapter, we introduced one method to identify isomorph. A brief summary here is that in equilibrium situations, determining isomorphic state points involves studying fluctuations, in particular of the potential energy U, and the virial W. The latter is essentially (apart from a factor of the volume) the part of the pressure associated with the interactions. It can be defined as the derivative of U for a configuration with respect to $\ln \rho$, where $\rho \equiv N/V$ is the number density of the system with N particles in a volume V. When taking the derivative it should be understood that the relative positions of the particles are kept fixed and only

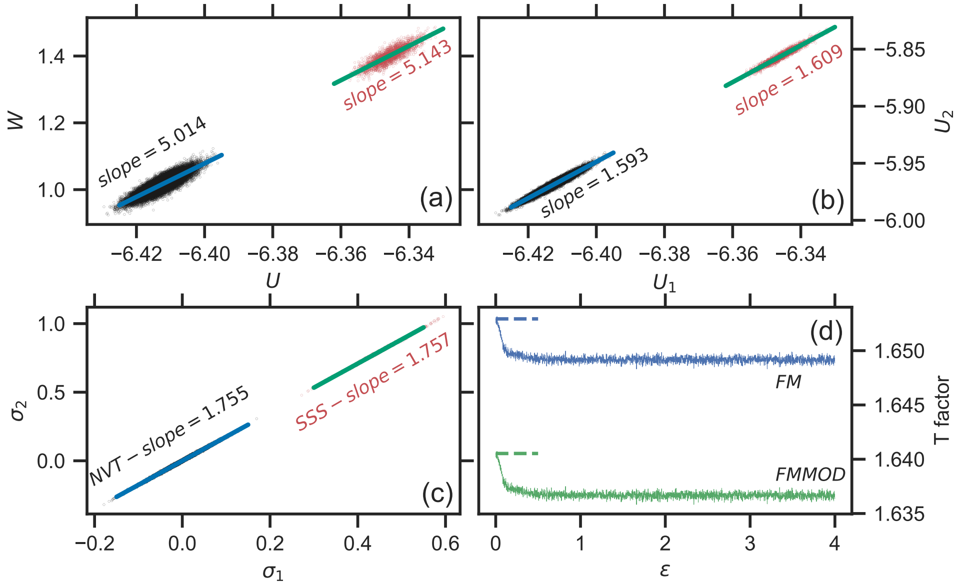

Figure 5.4: Various methods to obtain the temperature ratio T_2/T_1 used to identify the state point ρ_2, T_2 isomorphic to state point ρ_1, T_1 from simulations at the latter. The example here uses reference density and temperature $\rho_1 = 1.183$ and $T_1 = 0.3$ and a starting configuration cooled at $|\dot{T}| = 10^{-5}$. We consider a new density $\rho_2 = 1.1\rho_1 = 1.301$. Black indicates results from NVT simulations and red is for the steady state from a shear simulation with the highest (reduced) strain rate $\tilde{\dot{\epsilon}} = 10^{-3}$. During the simulations the system was rescaled to ρ_2 at regular intervals and the potential energy, forces, and shear stress were calculated on the scaled configurations. Panel (a), scatter-plot of the virial W versus potential energy U. The slopes (correlation coefficient) of the two fits are 5.014 (0.869) and 5.143 (0.859) respectively, where the slopes can be considered estimates of the density scaling exponent γ, which yields the temperature factor via Eqs. (5.6) and (5.8). Panel (b), scatter-plot of U_2 against U_1 (DIC-pe). The slopes (correlation coefficient) are 1.593 (0.975) and 1.609 (0.972) respectively. Here the slopes correspond directly to the temperature ratios. Panel (c), scatter-plot of σ_2 against σ_1. The slopes (correlation coefficient) are 1.755 (1.00) and 1.757 (0.999). Here the temperature ratio is the slope divided by the density ratio 1.1. Panel (d) shows the temperature ratio given by the force method FM (blue), Eq. (5.3), and modified force method (green), Eq. (5.4) from the same shear simulation. The dotted horizontal lines indicate the corresponding temperature ratios from the NVT simulation. Table 5.1 gives the results of the different methods.

a uniform scaling is involved. As elaborated below, strong equilibrium correlations between U and W allow isomorphs to be identified via the slope in the W, U-scatter plot, called the density scaling exponent and denoted γ. The latter is the local slope of an isomorph in the $\ln\rho, \ln T$ plane, also defined generally as the slope of configurational adiabats–curves along which the excess entropy is constant[53].

$$\left(\frac{\partial T}{\partial \rho}\right)_{S_{\text{ex}}} = \gamma(\rho, T) = \frac{\langle \Delta U \Delta W \rangle}{\langle (\Delta U)^2 \rangle} \tag{5.1}$$

where the second equality indicates how γ is determined from fluctuations at a particular state point. Angle brackets represent NVT ensemble averages, and the expression is simply the linear regression slope of a scatter plot of W against U. From the same linear regression fit a correlation coefficient R may be extracted, which is used to gauge the expected quality of the isomorphs. By determining γ from fluctuations an isomorph in equilibrium may be traced by simple numerical integration (explicit Euler method) of Eq. (5.1), taking one small step in density (typically 1% although larger jumps are possible with higher order integration techniques). In summary, we perform this method through NVT simulations at one density and temperature point to obtain the γ and solve for the isomorphic new density and temperature. The same process is repeated at the new density and temperature so that an isomorph can be traced.

In the present work we include some glasses cooled relatively quickly; in these cases γ determined from NVT fluctuations could be sensitive to aging effects and thus hard to define precisely. Nevertheless for comparison we have determined γ from NVT simulations in the less stable glasses (cooled with the fastest cooling rate). In the absence of true equilibrium the next best thing is steady-state deformation. Thus one could look at U, W fluctuations in the steady state and identify an exponent γ from the slope there. An example of this is shown in Fig. 5.4 (a). Here U, W correlations are shown both for the static NVT simulation and the steady-state regime of the shearing simulation. The NVT value for γ is 2.5% lower than the value from the steady state fluctuations. With a γ value we can generate isomorph curves analytically. This difference in γ translates to a difference in the estimated isomorphic temperature T_2 for the density $\rho_2 = 1.1\rho_1$ as shown in Table 5.1; for this density change of 1.1 the temperatures differ by 1% but the difference will increase with larger density jumps.

5.3.2 Direct isomorph check

For Lennard-Jones systems a simple analytic formula for isomorphs exists which in principle only requires a single evaluation of the exponent γ. This avoids the many simulations needed for numerical integration. For systems where an analytic expression is not available, a method involving scaling configurations sampled at one state point to another density allows the corresponding temperature to be identified from a plot of potential energies at scaled density versus at unscaled configurations. This is known as the direct isomorph check and can give accurate estimates of isomorphic temperatures up to fairly large density changes. Such formulation of two state points being isomorphic is equal to involving the proportionality of Boltzmann factors of corresponding microscopic states. Here corresponding means all particles being the same in reduced coordinates, i.e., one configuration is obtained from the other by a uniform scaling. A consequence of this proportionality, obtained simply by taking logarithms, is a proportionality between scaled and unscaled potential energies

$$U_2(\mathbf{R}) = \frac{T_2}{T_1} U_1(\mathbf{R}) + \text{const.}, \tag{5.2}$$

where subscripts 1 and 2 indicate potential energies evaluated at densities ρ_1 and density ρ_2, respectively for any configuration with given reduced coordinates. Here we use the upper case boldface $\mathbf{R}$ to represent the entire 3N-vector of particle coordinates, for convenience. This was originally considered a simple check of the basic isomorph concept of proportional energy fluctuations, hence the name direct isomorph check (DIC), but it also suggests that given two densities, and the temperature of the first, T_1, the second temperature T_2 may be identified by sampling configurations from an equilibrium simulation at the first state point, scaling them to density ρ_2, calculating the potential energies of the scaled configurations, and making a scatter plot of the scaled versus unscaled potential energies. Furthermore, when considering infinitesimal density changes the DIC reduces to the method of integrating Eq. (5.1).

Here the DIC data is shown in Fig. 5.4 (b), containing both "SSS" and corresponding "NVT" data. Determining the slope gives a direct estimate of the temperature factor, 1.609 from the steady-state and 1.593 in NVT. These are equal to the estimates from combining γ and the analytical formula (consistent with γ being the infinitesimal version of the DIC). Both these methods are based on the full fluctuations of potential energy during the steady state or NVT, and how these fluctuations change as density is changed.

5.3.3 Stress-based direct isomorph check

One can interpret the DIC as choosing the temperature T_2 by requiring the reduced-unit energy fluctuations to be as close as possible between the two state points, where "as close as possible" involves a linear regression fit. One can in principle make a similar requirement for other quantities, for example the virial, whose fluctuations should also be related by being the same in reduced units. Or the more related quantity we care about: the shear stress (configurational part). The latter leads to an alternative version of the direct isomorph check where the shear stress for scaled configurations is plotted against that for the unscaled ones. In this case, in view of $\tilde{\sigma}_f \equiv \frac{\sigma_f}{\rho k_B T}$, the slope of the linear regression should be $\rho_2 T_2/\rho_1 T_1$. This suggests an alternative method for identifying an isomorphic temperature which may be relevant in deformation simulations.

Fig. 5.4 (c) shows the related data. The observed slope when plotted the scaled versus unscaled shear stresses is not the temperature-factor, but includes also a factor of the density ratio $\rho_2/\rho_1 = 1.1$. After dividing the latter out the temperature ratio (T_2/T_1) estimate from steady state fluctuations is slightly lower (0.7%) than the corresponding energy-based DIC estimate, see Table 5.1. Interestingly, the correlation coefficient is much closer to unity for the stress-based DIC than for the energy-based DIC, and the difference between NVT and SSS estimates is much smaller than that for the energy-based DIC, at only 0.1%. These two estimates are also very close to the NVT energy-based DIC estimate.

5.3.4 Force method

Another recent development is the introduction of the "force-method (FM)" which rather than examining fluctuations in the global potential energy during a simulation, examines the forces on all particles, from a single configuration, and how these change upon a uniform scaling (density change)[**?**]. The great advantage of being able to work with a single configuration is that equilibrium fluctuations are no longer needed, and non-equilibrium states can also be mapped to isomorphic states at different densities. Given, as before densities ρ_1 and ρ_2, and temperature T_1, the estimated isomorphic T_2 is given using the force method by

$$T_2 = T_1 \left(\frac{\rho_1}{\rho_2}\right)^{1/3} \frac{|\mathbf{F_2}|}{|\mathbf{F_1}|} \tag{5.3}$$

The above expression was derived by minimizing a certain mismatch function between reduced forces at the two densities, but it can be interpreted quite simply: it is the temperature for which the magnitude of the force vector is the same in reduced units for both densities. Note that the concept of temperature may not be well defined for an isolated configuration when non-equilibrium, *i.e.*, T_1 could be unknown if only one single configuration is provided. Dyre has shown, however, that a temperature can be defined for individual configurations, based on their potential energy, called the *systemic temperature.*[43, 44] The force method can then also be interpreted as giving the ratio of systemic temperatures upon a change of density.

Yet another interpretation of the force method is that it is analogous to the DIC, but considering energy fluctuations associated with infinitesimal displacements of all 3N coordinates from a given configuration. However in that case, expression (5.3) corresponds not to the linear regression slope of the DIC plot but to a symmetric slope equal to the ratio of standard deviations of the two variables. A version of the force method more directly analogous to the DIC would involve the asymmetric linear regression slope, giving the following "modified force method (FMMOD)" expression for the new temperature

$$T_2 = T_1 \left(\frac{\rho_1}{\rho_2}\right)^{1/3} \frac{\mathbf{F_1} \cdot \mathbf{F_2}}{\mathbf{F_1} \cdot \mathbf{F_1}} \tag{5.4}$$

The modified force method gives a slightly lower temperature estimate. Since both force methods only require a single configuration to give a temperature ratio T_2/T_1, they can be applied repeatedly through a simulation, giving an immediate estimate of statistical errors and possible systematic changes. Fig. 5.4(d) shows the temperature ratios for both force methods for a simulation carried out at density 1.183 and a density increase of 1.1. There is a clear systematic decrease in the estimated temperature ratio for the original force method as the strain increases from zero to steady state conditions, from 1.653 to 1.649. The former value coincides with the estimate from an NVT simulation, shown with a short horizontal line. It is also clear that the statistical fluctuations are rather small in the steady state–the differences appear only in the fourth decimal, so that the estimate from a single configuration would indeed give a precise estimate of the ensemble average. The figure shows also the estimate from the modified force method, which is systematically lower by about 0.7%. The

SSS values are lower than the NVT values for both force methods, opposite to what is seen in the γ and DIC methods, and the differences are small, of order 0.25%.

Note here that even apart from the ability in principle to do large density changes, the standard numerical methods for generating isomorphs (integration of the equation of a configurational adiabat and the direct isomorph check) are both technically based on sampling from an equilibrium ensemble. The appeal of the force method is that it requires in principle only a single configuration, though averaging over (relatively) few independent configurations gives more precise estimates. Thus it allows generation of isomorphic state points without erasing the thermal history.

5.3.5 Comparison of above methods

In this subsection we compare the methods described so far. We have seen in the example shown in the figures above that for the initial density 1.183 and a density increase of 10%, slightly different estimates of the temperature ratio are given by the different methods, which are summarized in Table 5.1. The largest temperature factor is given by the force method in the steady state flow, while the smallest is given by either the γ method or DIC using NVT data or the stress-based DIC using either NVT or SSS data. Concentrating from now on on the SSS estimates, the spread between highest and lowest corresponds to 3.5%. We next consider how this variation depends on the size of the density jump.

What we do is the following. First of all, for the results from the NVT simulation, we run one NVT simulation at the starting density $\rho = 1.183$ and temperature $T_{start} = 0.3$ (cooled with the fastest rate). At each simulation time step, the configuration is scaled to other nine densities and the needed quantities such as potential energy, force method temperature factor as well as the stress are then calculated at these scaled densities. We label the densities with subscripts starting from zero, as $\rho_0 = 1.183$, $\rho_1 = 1.1\rho_0$, ..., $\rho_9 = (1.1)^9\rho_0$. The temperature factors of all methods can then

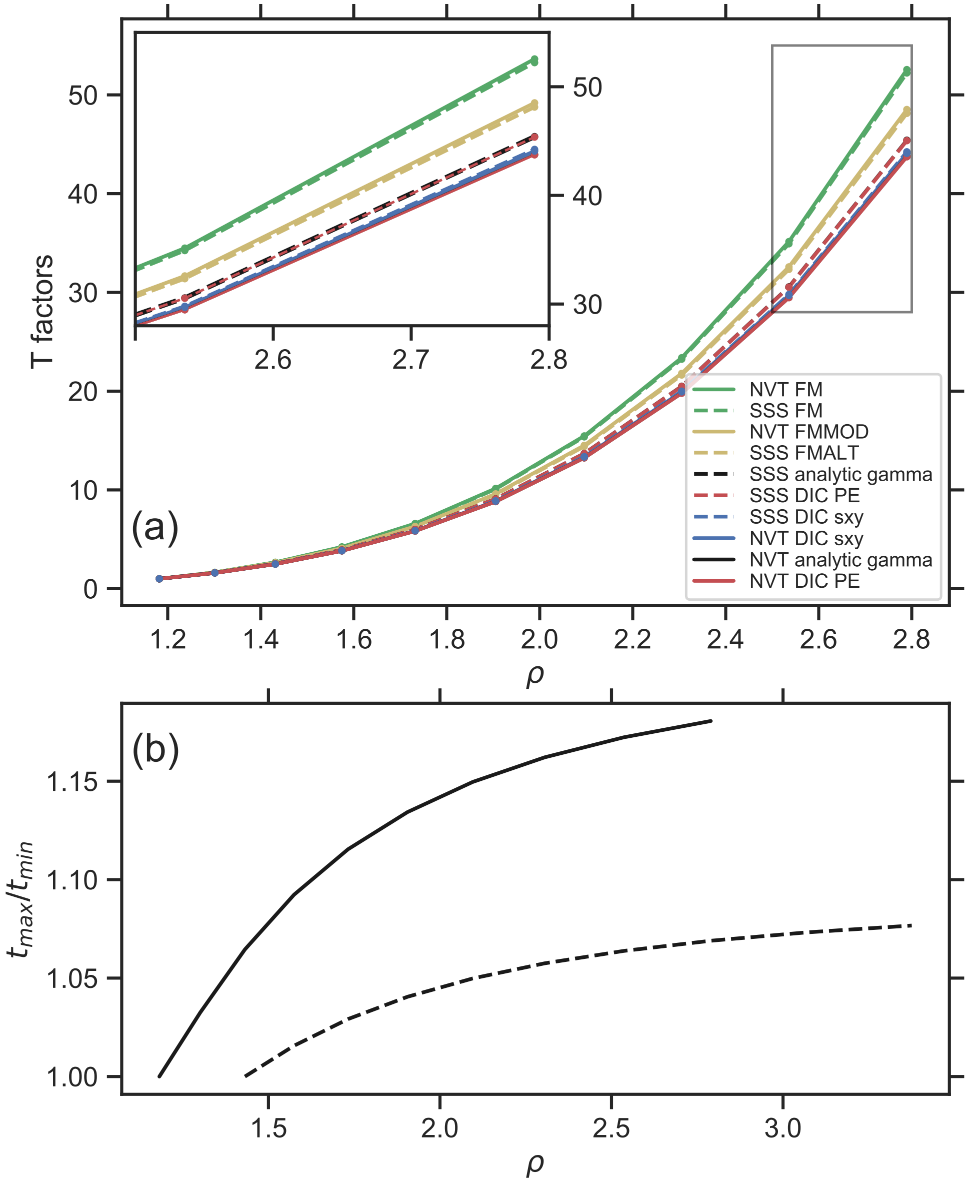

Figure 5.5: Top panel: temperature factors from different methods against density for starting density 1.183. Solid lines are for NVT simulation (NVT) 10^7 steps and dashed lines are for steady state (SSS). Inset zooms in for the largest two densities. Bottom panel: the ratio between the highest and lowest temperature factors of the SSS from the top panel versus density. Solid line starts at $\rho = 1.183$, and dashed line starts at $\rho = 1.301$.

be obtained. Similar for the steady state results (SSS). We shear the same starting configuration with the fastest strain rate $\tilde{\dot{\epsilon}} = 10^{-3}$. At each simulation time step, same procedure is performed and the corresponding SSS results are acquired. Fig. 5.5 (a) shows the temperature factors from the aforementioned methods versus density. For small density changes, all these methods return similar results with little discrepancy, even for our non-equilibrium state. This discrepancy increases with larger density spans, indicating that one needs to be more cautious when finding isomorphs under such situations. On the other hand, the same calculation of temperature factors but at a 10% higher starting density shows much less difference between various methods, as shown in Fig. 5.5 (b). The higher the starting density is, the closer the system is to the inverse power law potential (IPL) system, the more accurate the isomorph approximation is, leading to the overall smaller T_{max}/T_{min} in Fig. 5.5. Note here that the IPL system is generally considered to be isomorphically exact. For our lowest density the value of the correlation coefficient R, is around 0.86-0.87 (see the caption of Fig. 5.4), lower than the typical criterion of 0.9 for good isomorphs, therefore it is not surprising that the methods give diverging estimates. For the next lowest density, 1.301, the value of R is 0.972, substantially higher, and therefore one can expect less divergence between the different methods, as the potential energy landscape becomes increasingly well approximated by that of an IPL.

5.3.6 Matching the flow stress

We are primarily interested in identifying isomorphs as curves along which physically relevant quantities, a key example being the flow stress, are invariant (in reduced units). Therefore the question is now which of the above methods actually yields the most invariant flow stress?

Figure. 5.6(a) shows for density 1.301 the reduced flow stress obtained by simulating at several temperatures, corresponding to the temperature estimates using the

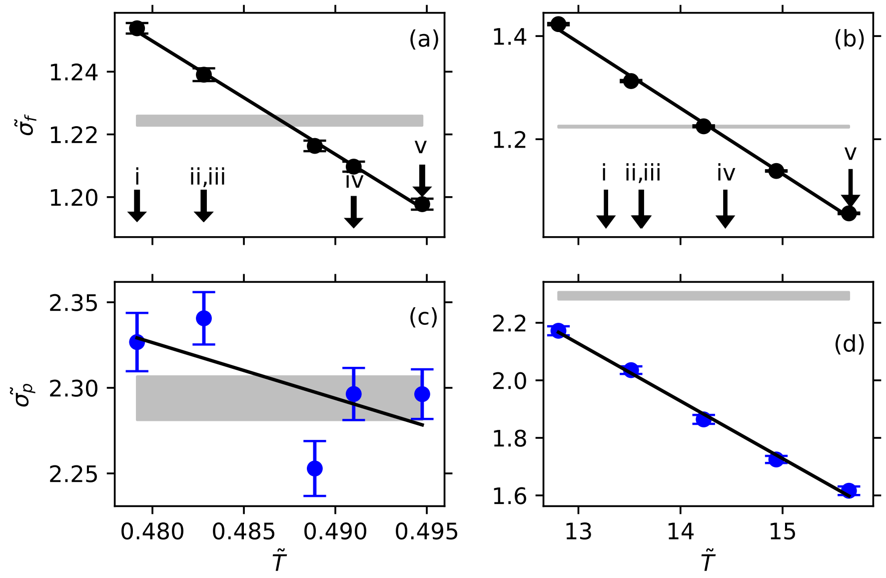

Figure 5.6: The reduced flow stress $\tilde{\sigma_f}$ and reduced peak stress $\tilde{\sigma_p}$ against temperature near the point of matching stress at $\rho = 1.301$ (left two panels) and $\rho = 2.789$ (right two panels). Same cooling rate and strain rate as in Fig. 5.1. Solid black lines are linear fits. Gray horizontal lines indicate the $\tilde{\sigma_f}$ in panel (a) and (b), and $\tilde{\sigma_p}$ in (c) and (d) at the reference density with shaded region indicating error. Arrows in panel (a) and (b) point to T estimated using: (i) DIC stress method; (ii) DIC PE method; (iii) Analytical gamma method; (iv) FMMOD; (v) FM.

five methods mentioned above. Panel (b) of the figure shows a similar plot for the highest simulated density; here the trial temperatures were not those given by the other methods, but chosen to span a similar range. To obtain precise estimates of flow and peak stresses, averaging of the 40 independent runs is necessary. The errors on the flow stress can be made reasonably small by averaging over strains $2-4$ and over the 40 runs. The errors on the peak stress are necessarily larger because long runs do not help here, although averaging independent runs still helps. There is a clear negative linear dependence of the reduced flow stress on temperature, reflecting that barriers to flow can be crossed more easily at higher temperature (thus requiring smaller external driving). The arrows indicate the temperatures determined by the various methods, which clearly don't match the reference flow stress within errors. The method that comes closest is the modified force method.

Panels (c) and (d) of Fig. 5.6 show the measured reduced peak stresses at the same two densities and and the same temperatures as the flow stress in panels (a) and (b). Like the flow stress, the peak stress also has a negative linear correlation with temperature, although the larger errors combined with the limited temperature range in panel reduced the apparent correlation in (c) . Comparison with the value at the reference density indicated by the gray bars presages one of our main results, that for high density changes no temperature can be found which matches both the flow and peak stresses with their values at the reference state point.

We then decide to determine the isomorphic temperatures pragmatically for each density using the linear relation in Fig. 5.6(a) and (b). The ultimate criteria is to match the flow stress at each density to the reference one ρ_0. Assuming the linear relation in Fig. 5.6 is generally true near all densities, the rigorous way is to follow what we do in Fig. 5.6, which is to simulate several temperatures in a small range and calculate the slope of stress against temperature. Then the T_i at density ρ_i can be obtained by simply solving the linear equation provided the stress at ρ_0. However, this procedure of simulating several temperatures at each density would be very time consuming if it should be done at all densities of interest.

Let's recall that for pair potentials, an analytic formula describing the shapes of isomorphs is available[62], which for the Lennard-Jones potential takes the form $T(\rho) \propto h(\rho)$, where the density scaling function $h(\rho)$ is given by

$$h(\rho) = A\rho^4 - B\rho^2 \tag{5.5}$$

The analytic form of $h(\rho)$ is directly related to that of the potential (indeed it is essentially the second derivative of the pair potential, evaluated at $r = \rho^{-1/3}$ and expressed in reduced units)[14]. The overall normalization of $h(\rho)$ is undefined since there is a proportionality constant in the relation between it and the temperature, so there is in fact only one free parameter, which can be taken to be the ratio B/A. If this is known then given two densities, ρ_1 and ρ_2, and a temperature T_1 corresponding to density ρ_1, the temperature T_2 corresponding to density ρ_2 is given by

$$T_2 = T_1 \frac{h(\rho_2)}{h(\rho_1)} = T_1 \frac{\rho_2^4 - (B/A)\rho_2^2}{\rho_1^4 - (B/A)\rho_1^2} \tag{5.6}$$

To fix the parameter B/A, two options are available. One can note that the logarithmic derivative of $h(\rho)$ must also be equal to the density scaling exponent γ,

$$\gamma(\rho) = \frac{d \ln h(\rho)}{d \ln \rho} = \frac{4\rho^4 - 2(B/A)\rho^2}{\rho^4 - (B/A)\rho^2}, \tag{5.7}$$

where here the approximation of γ depending only on density is explicit. Considering a particular reference density ρ_{ref} at which γ is to be evaluated (for example by simulation), isolating B/A gives

$$\frac{B}{A} = \frac{\gamma(\rho_{ref} - 4)\rho_{ref}^2}{\gamma(\rho_{ref} - 2)} \tag{5.8}$$

In principle, if isomorph theory was exact, one could run a single simulation at the reference density, evaluate γ from the U, W fluctuations there, use Eq. (5.8) to determine B/A and generate the whole isomorph using Eq. (5.6). This works reasonably well for small density jumps, say 10%–so certainly better than integration method with steps of 1%, but it does not give accurate temperatures for very large density jumps. Rather, the greatest utility of the analytic isomorph expression is its use in *interpolating* between points known to be isomorphic to get the points between[13]. That is, if both densities and temperatures for two state points, ρ_1, T_1 and ρ_2, T_2 are known, Eq. (5.6) can be solved for B/A, giving

$$\frac{B}{A} = \frac{\rho_2^4 - \rho_1^4 \frac{T_2}{T_1}}{\rho_2^2 - \rho_1^2 \frac{T_2}{T_1}} \tag{5.9}$$

Then temperatures for densities between ρ_1 and ρ_2 can readily be found. This is the manner in which we use the analytical formula here–note that it does not explicitly depend on having equilibrium. In order to use this interpolation, two isomorphic points are needed in prior. In this way, instead of all nine densities, we only need to obtain two temperatures at the starting and ending densities.

It should be noted here that in applying the analytic expression for isomorphs, we have to treat ρ_0 separately. Related to its somewhat low value of the correlation coefficient R (Fig. 5.4) and the fact that methods for determining isomorphic temperature starting from this density diverge rather quickly (Fig. 5.5), it turns out that no parameterisation of the analytic formula can match the reduced flow stress over the full range from ρ_0 up to ρ_9. Such a parameterization can be found for the range ρ_1 to ρ_9, however. Thus we work as follows: Given the reduced flow stress at ρ_0 (and $T_0 = 0.3$) we use the linear fits in Fig. 5.6 (a) and (b) to determine the temperatures of matching reduced flow stress at densities ρ_1 and ρ_9, respectively. From Eq. (5.9) with ρ_2 replaced by ρ_9, and using these fit-determined temperatures T_1 and T_9 we fix the parameter B/A. Finally for the remaining densities $\rho_2, \ldots, \rho_8$ we determine the isomorphic temperatures from Eq. (5.6) in the form

$$T_i = T_1 \frac{h(\rho_i)}{h(\rho_1)} = T_1 \frac{\rho_i^4 - (B/A)\rho_i^2}{\rho_1^4 - (B/A)\rho_1^2}. \tag{5.10}$$

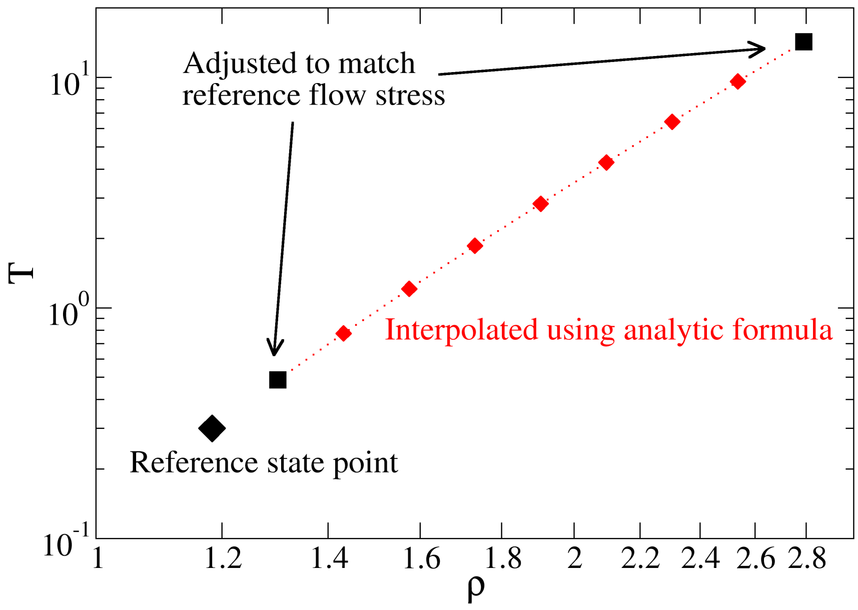

Figure 5.7: The isomorph determined by matching flow stress. The large black diamond indicates the reference state point. The two black squares represent points whose temperatures were identified by matching the reduced flow stress to that of the reference, using the linear fits in Fig. 5.6, and the red diamonds are points whose temperatures have been determined by interpolation between the black squares, using Eq. (5.10).

Figure 5.7 illustrates the construction of the isomorph using the interpolation method. The resulting densities and temperatures are listed in Table 5.2. These values were determined by matching the flow stress using the highest strain rate (reduced value 10^{-3}) (and fastest cooling-note though that cooling-rate should not matter for the flow stress). Rather than separately repeat this procedure for identifying isomorphic temperatures for the other strain rates and cooling rates, we take as a working hypothesis that the isomorphs in the $\rho - T$ plane determined by matching reduced

Density	Temperature
1.183	0.3
1.301299	0.487031
1.431428	0.774540
1.574571	1.208396
1.732028	1.859225
1.905231	2.831010
2.095754	4.276669
2.305330	6.420943
2.535863	9.593855
2.789449	14.279829

Table 5.2: The densities and temperatures along the isomorph identified through matching the flow stress at the first, second, and last densities, and then using the analytical method to obtain the temperatures in between.

flow stress do not depend on which reduced strain rate and which cooling rate was used. The validity of this hypothesis will be investigated in the next section. The next step is the shearing deformation simulations along this isomorph. These are still very time-consuming, because at each density, and the corresponding temperature determined by the above procedure, 40 independent runs were carried out. This was repeated for all three cooling rates and all three strain rates. From these simulations, stress strain curves in reduced units are plotted, and the flow stress and peak stress are extracted as described above.

5.4 Invariance of flow stress and peak stress

With the protocol for determining the putative isomorph established, we now present our main results. Figure 5.8 shows the full (reduced) stress strain curves for all densities along the isomorph generated as described above, using reduced strain rate 10^{-3} and initial configurations cooled at rate 10^{-5} (at the reference density; configurations were scaled to the indicated densities before shearing). The initial elastic parts of the curves overlay, showing that the elastic shear modulus is invariant in reduced units along the isomorph. Also it is clear that the steady state flow stresses match, at least within the fluctuations–this is expected since the isomorph was constructed to have invariant flow stress. Nevertheless it serves as a check that the analytic formula for constructing the isomorph is reliable. However, the peak in the stress-strain curve is clearly not invariant–it decreases systematically with increasing density, by about 20%, as the density rises to 2.8. Thus we have a clear deviation from isomorph invariance when the transient response to shearing is considered. It is worth recalling that the change in real (no reduced) shear stress over the density range studied involves a factor of $\rho k_B T$ which changes by over two orders of magnitude.

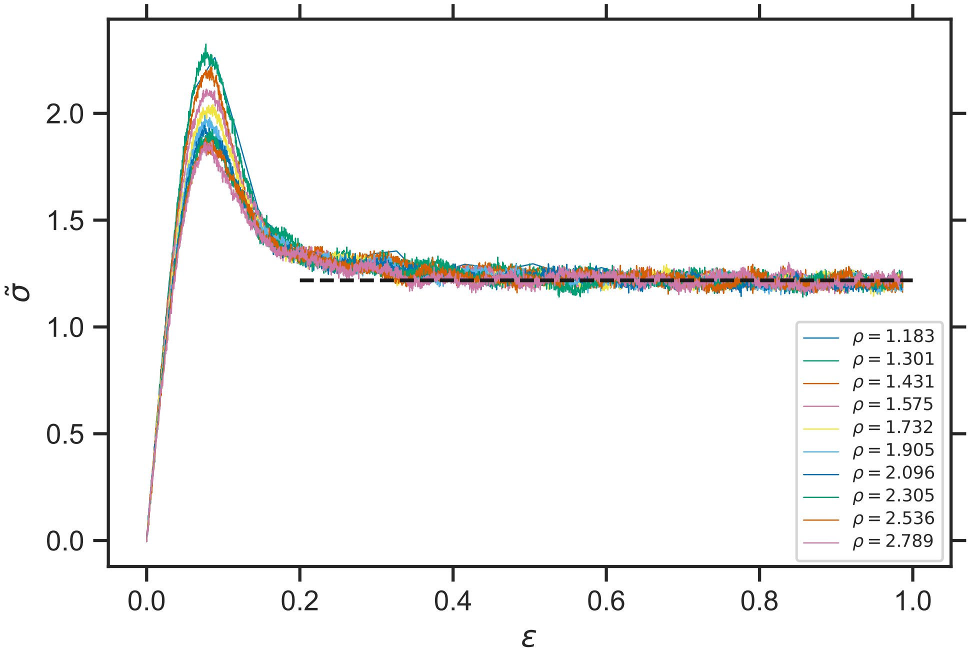

Figure 5.8: Stress-strain curves along isomorph determined by matching flow stress (in reduced units) of the largest density and second density to that of the first density (indicated by dashed line), and then using analytical formula to calculate corresponding T in between. Glasses at cooled (at lowest density) at rate $|\dot{T}| = 10^{-5}$ and sheared at reduced strain rate $\dot{\tilde{\epsilon}} = 10^{-3}$.

We find similar results for the other strain rates and cooling rates. Rather than show all of those stress-strain curves here, we instead extract the flow stress and peak stress from each stress strain curve, and plot these as a function of density in Fig. 5.9(a) and (b), respectively.

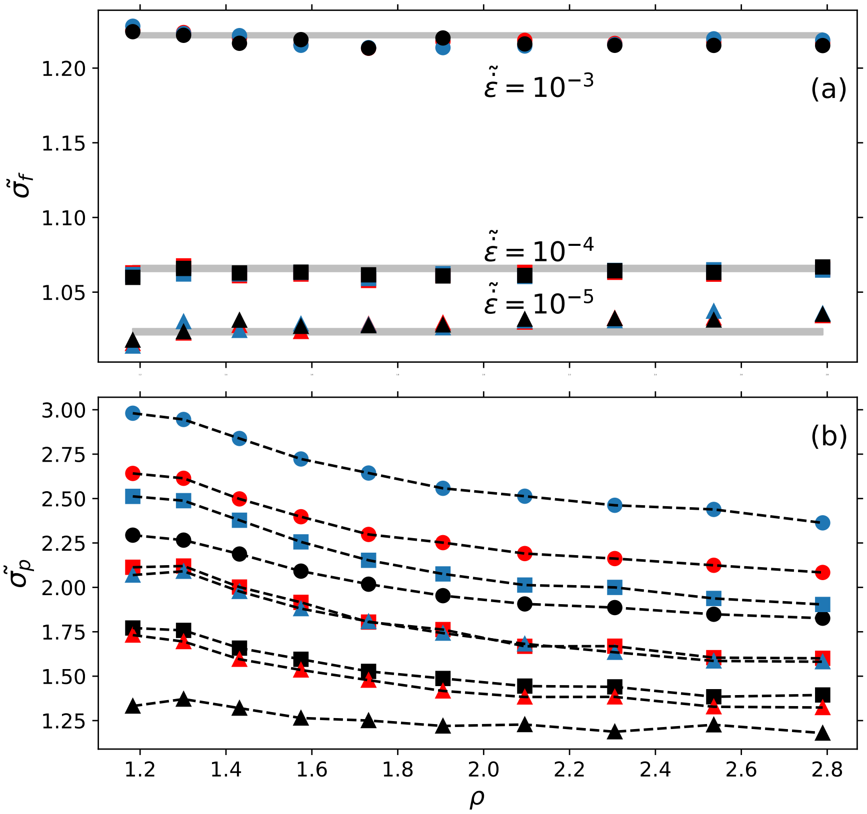

Figure 5.9: (a) $\tilde{\sigma_f}$ and (b) $\tilde{\sigma_p}$ against density along the isomorph for $|\dot{T}| = 10^{-5}, 10^{-6}, 10^{-7}$ (black, red, blue), and $\tilde{\dot{\epsilon}} = 10^{-3}, 10^{-4}, 10^{-5}$ (circle, square, triangle). Each point in (a) is an average of 40 shear simulations (on 40 individual configurations) and we use the standard deviation divided by $\sqrt{40}$ as the error ($\sqrt{30}$ for $\tilde{\dot{\epsilon}} = 10^{-5}$). For the peak stress (panel (b)), we first divide the 40 shear runs into 5 groups and obtain 5 averaged stress and strain curves. We then fit the data for 10% strain around the maximum stress using a fourth-degree polynomial and identify the maximum of the fit as the $\tilde{\sigma_p}$. The error is the standard deviation of the 5 values divided by $\sqrt{5}$. The three families in (a) correspond to $\tilde{\dot{\epsilon}} = 10^{-3}, 10^{-4}, 10^{-5}$ from top to bottom respectively. The errors are all smaller than the marker size. The position of the gray bars in (a) are the reference $\tilde{\sigma_f}$ (at ρ_1 cooled with $|\dot{T}| = 10^{-5}$ and sheared with $\tilde{\dot{\epsilon}} = 10^{-3}$) and the width of the bar indicates the reference $\tilde{\sigma_f}$ plus or minus the error (standard deviation divided by $\sqrt{40}$ or $\sqrt{30}$ for the slowest strain rate).

Before considering the isomorphic behavior, we note that as expected, slower strain rates decrease both the peak stress and the flow stress; and slower cooling rates increase the peak stress but leave the flow stress unchanged. The isomorphic behavior is understood through the dependence (or non-dependence) of these quantities on density. In part (a) of the figure we see that the flow stresses are indeed flat within errors, as they have been constructed to be (the errors are comparable to, though smaller than, the symbol sizes). This plot also confirms our hypothesis that the isomorph determined by requiring invariant flow stress at one cooling rate and reduced strain rate is valid also for the others. Part (b) of the figure shows the evolution of the reduced peak stress as a function of density along the isomorph. The trend is similar for all cooling and strain rates, with more or less similar relative drops of peak stress as density increases. In all cases the bulk of the drop occurs over densities $\rho_1 \simeq 1.3$ to $\rho_5 \simeq 1.9$, after which the change in reduced peak stress for each 10% increase in density is reduced. Interestingly the change between densities ρ_0 and ρ_1 is also smaller. Above density 1.9, $\tilde{\sigma}_p$ apparently continues to decrease linearly, which is surprising, since one would expect it to flatten out in the high-density limit as pure-IPL behavior begins to dominate. The magnitudes of the relative stress drops over the full density range for all strain and cooling rates are given in Table 5.3. The only apparent trend here is that both faster cooling and faster shearing tend to give slightly smaller drops, around 20% instead of around 24%. An apparent outlier is the value for the highest cooling rate and the lowest strain rate (black triangles), where the change in reduced peak stress is quite limited, only 11%. This case corresponds to the least stable glass being very slowly deformed, and has the lowest peak stress to start with. Table 5.4 shows the ratio between peak stress and flow stress at the lowest density. This indicates indeed that that same case of lowest strain rate and fastest cooling has the lowest ratio of peak to flow stress at the lowest density, 1.31. However there does not seem to be, upon comparing Tables 5.3 and 5.4, a general

	$\tilde{\dot{\epsilon}} = 10^{-3}$	$\tilde{\dot{\epsilon}} = 10^{-4}$	$\tilde{\dot{\epsilon}} = 10^{-5}$
$\lvert\dot{T}\rvert = 10^{-5}$	0.204 ± 0.011	0.213 ± 0.014	0.114 ± 0.009
$\lvert\dot{T}\rvert = 10^{-6}$	0.211 ± 0.006	0.243 ± 0.008	0.236 ± 0.012
$\lvert\dot{T}\rvert = 10^{-7}$	0.207 ± 0.010	0.242 ± 0.006	0.236 ± 0.008

Table 5.3: Fractional change of $\tilde{\sigma_p}$ between the highest- and lowest-density isomorph points for different $|\dot{T}|$ and $\tilde{\dot{\epsilon}}$ combinations.

	$\tilde{\dot{\epsilon}} = 10^{-3}$	$\tilde{\dot{\epsilon}} = 10^{-4}$	$\tilde{\dot{\epsilon}} = 10^{-5}$
$\lvert\dot{T}\rvert = 10^{-5}$	1.87	1.67	1.31
$\lvert\dot{T}\rvert = 10^{-6}$	2.16	1.99	1.71
$\lvert\dot{T}\rvert = 10^{-7}$	2.43	2.37	2.04

Table 5.4: Ratio of $\tilde{\sigma_p}$ to $\tilde{\sigma_f}$ for the lowest-density isomorph points for different $|\dot{T}|$ and $\tilde{\dot{\epsilon}}$ combinations.

correlation between fractional drop of peak stress with increasing density, and initial ratio of peak to flow stress. The most that can be said probably is that when the latter ratio is very low, there is less contrast between the non-flowing and flowing states, in the sense that the microscopic barriers to be crossed are not much different to start with and therefore there is less room for variation along the isomorph.

5.5 Invariance of pair structure and single-particle dynamics in the steady state

The results of the previous subsection concern macroscopic mechanical properties. In this subsection we consider more microscopic properties, in particular self-diffusion and structure. To investigate self-diffusion we plot in Fig. 5.10(a) the mean squared transverse displacement (MSD) in reduced units, as a function of reduced time, for all densities along the isomorph at reduced shear rate 10^{-4}. By transverse we mean that only components of displacement orthogonal to the shearing direction are included. The quality of the collapse is extremely good, so that it is not obvious to the eye that there are in fact ten curves plotted. This plot is based on data from a single run out of 40, since there is sufficient averaging over particles to get good statistics for single-particle dynamics.

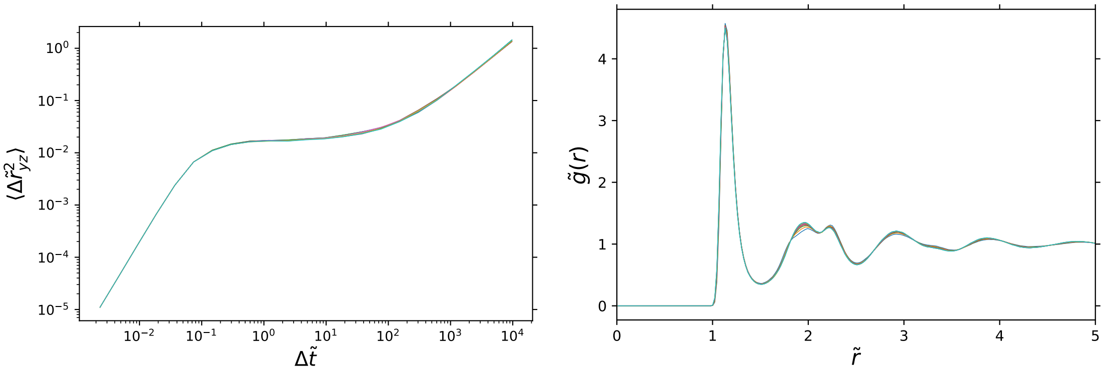

Figure 5.10: Collapse of (a) $\langle \Delta \tilde{r}^2_{yz}(\tilde{t}) \rangle$ and (b) $g(\tilde{r})$ (for AA pairs) for steady state only along an isomorph containing 10 points in the phase diagram calculated using the method described above. The starting configuration is at $\rho_0 = 1.183$ and $T_0 = 0.3$ and was cooled with $|\dot{T}| = 10^{-5}$. Shearing for all state points was with reduced strain rate $\dot{\tilde{\epsilon}} = 10^{-4}$.

Fig. 5.10(b) shows the radial distribution function (RDF) for AA pairs along the same isomorph. The collapse here is also very good, similar to what is seen in equilibrium liquids[53]. Both the MSD and RDF are determined from configurations drawn from the steady state. The quality of the invariance apparent in Fig. 5.10 confirms that the isomorph has been determined correctly. The non-invariance evidenced by the failure of the peak stress to collapse seems therefore to be restricted to the transition from non-flowing to flowing states. This will be discussed more below.

5.6 Investigation on the non-isomorphic peak stress

In attempting to understand the failure of the peak stresses to collapse, an important question is whether the configurations sampled near the stress peak at different densities are equivalent. Equivalent means (statistically) indistinguishable after scaling to match densities. The simplest way to answer this question is to take configurations from near the peak in a simulation at one density, scale them to a different density and calculate the shear stress at the new density, thus generating a fictional stress-strain curve based on scaling configurations statically. This is similar to what is done in the stress-DIC method proposed above, but rather than use it to generate an isomorph we use it to compare the potential energy surface sampled by the same reduced configurations at different densities. If the “fake” high-density stress-strain curve matches that actually simulated at high density, then the conclusion would be that configurations near peak stress are essentially equivalent to the corresponding ones at low densities. The interactions are softened more at high densities near peak stress than for high densities at lower stress (i.e. the steady state). If they do not match then something different must be happening in the microscopic dynamics during the stress peak. Fig. 5.11 shows the result of this check. The curve generated from configurations sampled at the reference density ρ_0 and scaled ρ_9 (green) matches the curve at the reference density well, except for a small difference in normalization, and does not match the curve obtained from actual simulating at the high density ρ_9, which has the much lower stress peak. This shows that the second possibility mentioned above must be the case: the particles undergo non-equivalent motion when simulated at the higher density. We examine what this non-equivalence is below.

We now present results of analyzing strain profiles and local measures of nonaffine activity in order to determine whether the variation of peak stress can be associated with some systematic difference in the spatial organization of the initiation of flow, for example if flow is more or less localized in the peak at higher densities compared to lower densities.

The first indicator we consider is the non-affine displacement at the particle level, same as in chapter 3 except here it is 3D. Recall that shearing motion occurs in the x-direction, while the gradient is in the y-direction. We first define the affine displacement $\Delta\vec{r}_{A,i}$ for particle i as $\Delta\vec{r}_{\mathrm{A,i}} = \Delta\epsilon\, y_i\hat{x}$, where y_i is the position of particle i in the gradient direction and $\hat{x}$ is the velocity direction. This is simply the displacement as-

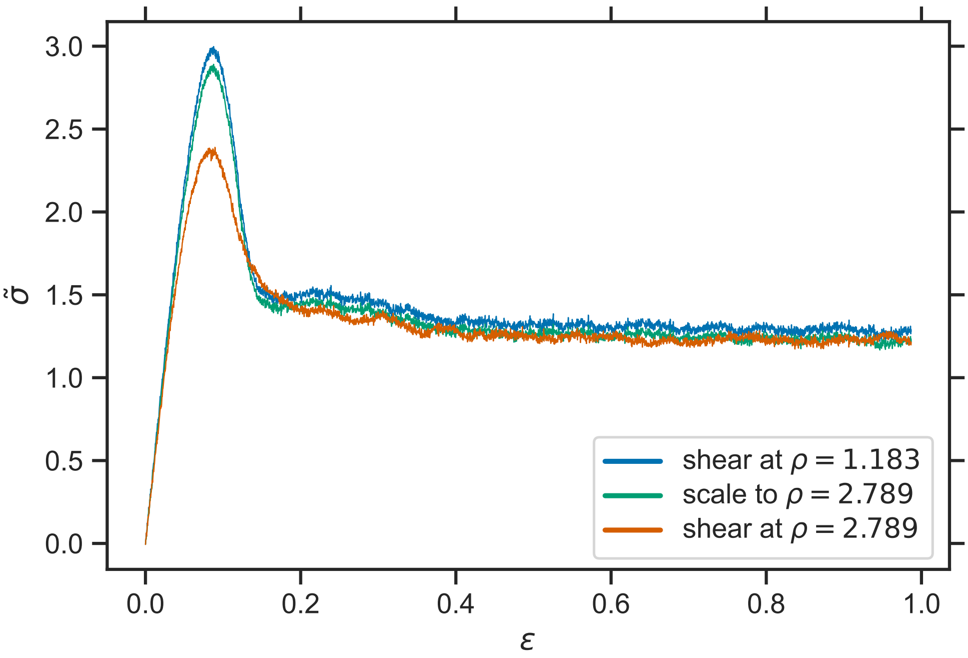

Figure 5.11: Comparison between stress-strain curves obtained from shearing at the lowest density (blue), computing the stress from the same configurations scaled to the highest density (green), and actually shearing at the highest density (orange) with $\dot{\tilde{\epsilon}} = 10^{-3}$ and $|\dot{T}| = 10^{-7}$.

sociated with the macroscopic strain imposed on the system, which is known. Under shear, local rearrangements cause deviations from this affine motion. We define such deviation as the non-affine motion $\Delta\tilde{\vec{r}}_{\mathrm{NA,i}} = \Delta\tilde{\vec{r}}_{\mathrm{real,i}} - \Delta\vec{r}_{\mathrm{A,i}}$, where $\Delta\tilde{\vec{r}}_{\mathrm{real,i}}$ is the full displacement of particle i [78, 54, 19]. We expect that each component of the non-affine displacement is symmetrically distributed about zero, but it is possible that the distributions for the different components could be different. Figure 5.12 shows the variance of the non-affine displacement for each component, in reduced units.

The data in part (a) of the figure are for displacements between undeformed configurations (strain 0) and corresponding configurations deformed to strain 0.12. The figure thus contains information about particle motions during the transition from the non-flowing to the flowing state, specifically those associated with the stress peak. As a function of increasing density the variance for each component increases systematically, indicating a non-isomorph invariant behavior. In part (b) of the figure, data

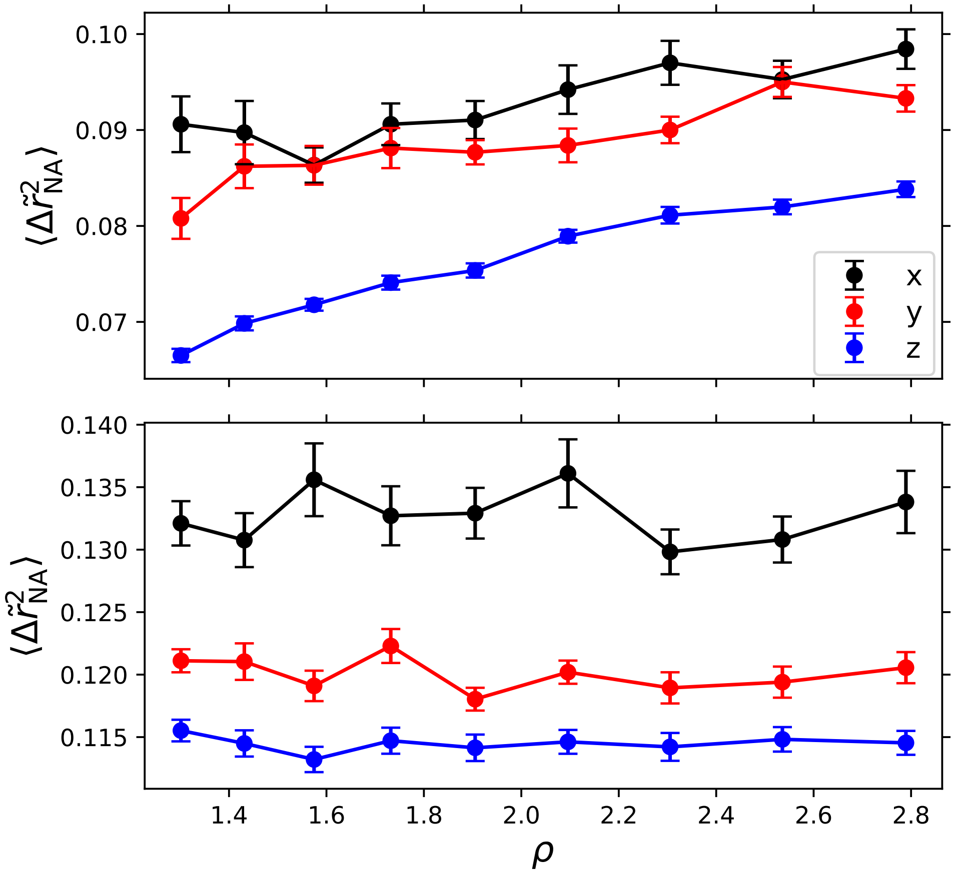

Figure 5.12: Comparison of non-affine particle motion over 12%-strain intervals between (a) transient state with $\epsilon \in [0, 0.12]$ and (b) steady state with $\epsilon \in [3.65, 3.77]$. Data is averaged over all particles and 40 independent runs. Color indicates the three components of the nonaffine motion squared and shown in the legend in (a).

for a similar strain interval, but taken from the steady steady regime is shown. Here no systematic variation as a function of density is apparent. Systematic differences between components are visible, with the variance for the x-component of non-affine displacement being highest both in the transient case and in the steady state. Chen *et al.* studied distributions of non-affine motion in experiments on colloids[19]; their Fig. 8 shows PDFs of non-affine motion in the three different directions. The distribution for the out-of-plane direction (their y-direction, corresponding to our z-direction) is slightly narrower than for the other two directions, which is consistent with what we see.

This measurement of nonaffine motions indicates increasing possibility for rearrangements to occur within systems at larger densities. Such dependence could be one contribution to the easier initiation of flow along the isomorph. The reason behind this larger variance of nonaffine motions for larger densities needs further investigation.

We note here that larger variance does not guarantee stronger spatial heterogeneity. The variance can originate either from spatial heterogeneity, i.e. different positions in the system behave differently; or simply from larger fluctuation, as illustrated in Fig. 5.13.

Therefore, we consider another related measure for spatial inhomogeneity which is the displacement profiles like Fig. 5.13 left panel. We calculate it by first binning particles according to their y-coordinate and then averaging the x-displacement Δx for all particles in a bin. This gives a probe of systematic variation in the gradient direction, while averaging over other directions.

An example is shown in Fig. 5.14 for a 12% strain interval from the steady state in a particular run. A clear systematic deviation from the affine profile is visible: the system exhibits two distinct regions with the strain differing by a factor of two as indicated by the linear fits (note that the region of the left is connected to that

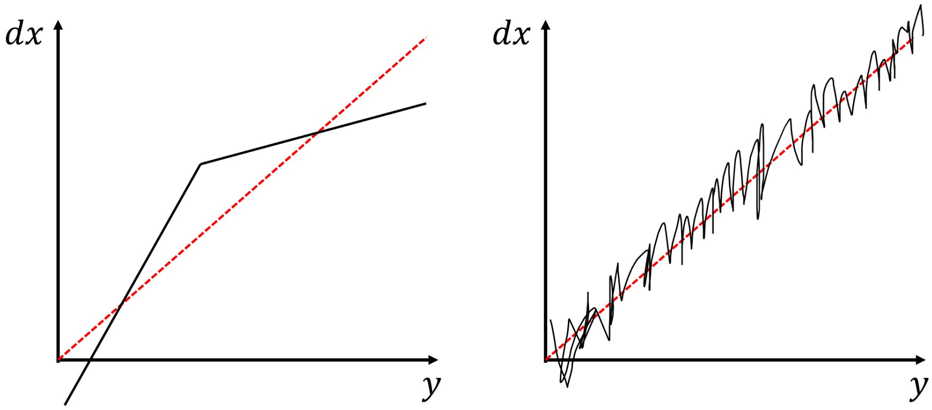

Figure 5.13: A sketch to illustrate the two possible origins for nonaffine motion variance. The left panel shows spatial heterogeneity while the right panel shows simple fluctuations.

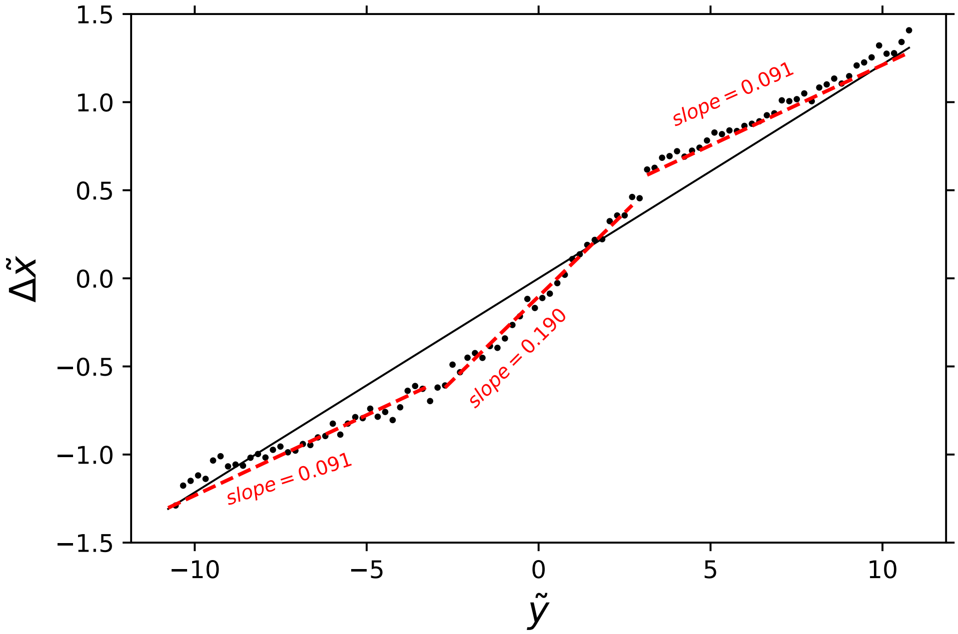

Figure 5.14: Example of a displacement profile. Displacement is calculated in steady state between $\epsilon = 3.65$ and $\epsilon = 3.77$ from a shear simulation at $\dot{\tilde{\epsilon}} = 10^{-4}$ from a configuration originally cooled at $|\dot{T}| = 10^{-5}$, by averaging the x-component of the particles' displacements over all particles within a bin defined by their y-coordinate. The straight line is the affine displacement following the applied strain. Dotted red lines are linear fits at different regions with two distinct slopes (treating the leftmost and rightmost regions together due to periodic boundary conditions).

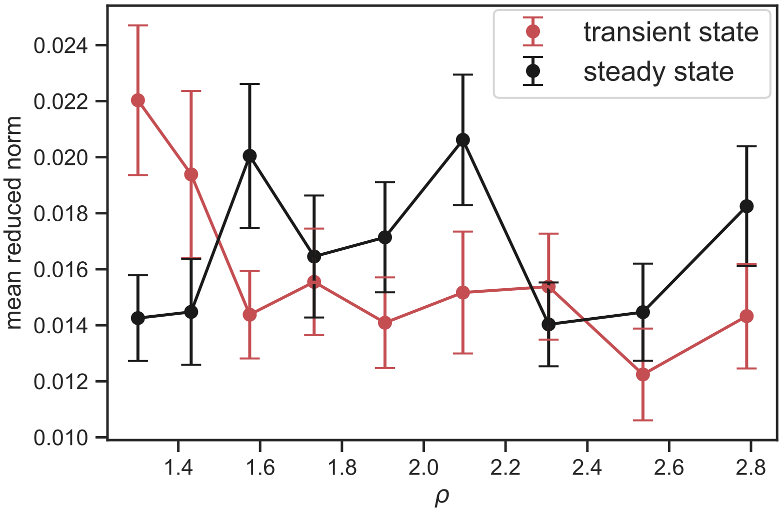

Figure 5.15: Comparison of norm of non-affine motion in velocity direction averaged of 40 configurations over 12%-strain intervals between transient state with $\epsilon \in [0, 0.12]$ and steady state with $\epsilon \in [3.65, 3.77]$. Errors are the standard deviation of the 40 runs divided by square root of 40. The definition of norm is the mean squared deviation of the displacement profile in Fig. 5.14. Note that the first density points are not shown here.

on the right via the periodic boundary conditions). This coexistence of regions with differing strain is akin to shear-banding, whereby strain is localized into a narrow band [136, 129, 50].

Profiles for different runs exhibit somewhat similar shapes, with mostly a single region of higher strain, more or less sharply delimited from the rest of the system, with varying contrast (i.e. difference in strain). To quantify this contrast and look for systematic variations along the isomorph, we take the mean squared deviation of each point from the affine line, yielding a norm of the (non-affine) displacement profile. For the example in Fig. 5.14 the norm is 0.022. Note this measure of non-affine motion differs from that presented in Fig. 5.12 in the initial averaging within a y-bin *before* squaring and further averaging over bins. We calculate the mean norm from the 40 runs at each density, and plot these as a function of density in Fig. 5.15.

As with Fig. 5.12 we see a clear trend in the transient data in panel (a), and no discernible trend in the steady state data in panel (b). This suggests that at lower density there is a greater tendency for quasi-shear-banding to occur during the stress peak. This decreases with increasing density, particularly over the first three densities. The steady-state values in panel (b) are mostly below the low-density transient values; there are a couple of exceptions to this but no overall trend.We have only looked at a specific interval covering 12% of strain in all cases; an interesting question for future work is to what extent a given quasi-shear-band persists over longer amounts of strain. Interestingly, and apparently counterintuitively, the trend visible in Fig. 5.15(a) is in the opposite direction to those shown in Fig. 5.12(a). An interpretation which encompasses both behaviors would be that the stress peak at the lower densities coincides with particles exhibiting less overall non-affine motion than at higher densities, but where whatever non-affine motion is actually present is more coherent (less contribution from fluctuation as in Fig. 5.13 right panel), and gives a larger signal in the displacement profiles.

5.7 Conclusion

The first part of this chapter was concerned with studying different methods for determining isomorphs in out-of-equilibrium situations. Particularly when large density changes are involved, different methods give varying results for the temperature at which the new state point should be isomorphic to the starting, or reference state point. The difference is up to 20%–of an overall variation of temperature up to a factor of order 50, for density changes of a factor up to about 2.3. For moderate density changes one can at least argue that any of these methods can give a reasonable estimate of isomorph temperatures; in particular the force method or its modification can do so with little computational cost. However one cannot be sure about the quality of the isomorph determined this way. The dream of being able to make directly reliable isomorph jumps in non-equilibrium situations is thus not realized. Presumably one could still make small jumps of 1-2% in density, simulating at each step and using a fluctuation method to compute the next temperature, as in the original isomorph paper[53]. This would be time consuming, but perhaps would not require as many independent runs as we have used here. Given these difficulties our strategy has been to require the reduced flow stresses to match at all densities as a practical method of identifying the isomorph.

Although gamma/DIC method can match most of the energy fluctuations very well, it does not guarantee the flow stress is matched. The latter is a signature of the energy barriers and what is clear is that the relevant energy barriers scale with a smaller factor than the more dominant contribution to the energy fluctuations. This would be worth investigating using barrier finding techniques on small systems to trace the way an energy barrier scales with increasing density.

Since Fig. 5.15 indicates that shear banding occurs also in the steady state, a varying tendency towards shear banding depending on density could actually be present in the steady state. Since we have chosen the isomorph temperatures to match the reduced steady-state shear stress we do not see this in our data, but this could potentially underlying the failure of the fluctuation methods to predict the steady-state stress.

Nevertheless, we show that our pragmatical method utilizing the analytical formula which describes the shape of an isomorph is able to match the flow stress to an excellent degree. The invariance of pair structure and the single-particle dynamics in the steady state is also verified. However, the peak stress is not invariant. Strain profiles and dependence of nonaffine activity on the density are examined. We find that particles in configurations with larger densities in average are more likely to have larger nonaffine motions, which supports our observation that peak stress decreases against density along the isomorph (i.e. easier to initiate the flow). More radical explanations for this non-isomorphic behavior of peak stress needs further investigation and the barrier finding techniques mentioned above might help.

Chapter 6

Conclusion

How materials react to externally applied deformation has been studied for centuries for various purposes. For example, it is of extreme importance for industrial application to understand how and when certain brittle materials fail or ductile materials flow under load. To be more specific, avalanches and earthquake are real life instances of such but at a huge length scale and understanding the mechanisms of which would be invaluable. There is no doubt that numerous ways exist to characterize and study these phenomenon. My interest is to understand them from the microscopic scale, *i.e.* what happens to the individual particles that causes the macro-scale behaviors, specifically for disordered solids. Recall that in the first chapter, the disordered solids or amorphous solids are defined as materials with disordered structures at any scales that share both solid and liquid properties.

However, this picture is too big. A metaphor that I used before in the first chapter is that the whole research area mentioned in the previous paragraph is like a tall building under construction. I work on amorphous solids systems that flow when deformed, which is like one floor in the building. Different properties or quantities that people care about are then like rooms in this floor. My first project (chapter 3) where we investigated the influence of polydispersity is trying to add bricks to these rooms. A reminder that large polydispersity generally means that the systems are composed of particles of various sizes. We verify that highly polydisperse systems behave qualitatively different than low-polydisperse systems that people usually study. We show that size matters in a way that large particles behave qualitatively different than small ones and have strong influence on their surroundings. An effective threshold size can be defined to distinguish large from small. We believe these bricks are significant in the sense that polydispersity is so widely prevalent in both real life and model systems people study and its effects on the behaviors of different systems are of great necessity to be understood. In fact, as mentioned in the introduction, indeed many novel interesting results are found for highly-polydisperse systems. Our results provide some new “bricks” for this purpose.

Furthermore, polydispersity has been drawing increasing amount of attention recently among the soft matter physics community. An example is that the “Swap Monte Carlo” simulation method has been applied to probe increasingly low temperatures of the glassy systems. Recall that a glassy system is defined as an out of equilibrium state where it takes unrealistic amount of time for the system to equilibrite on its own. In terms of simulation studies on these systems, the cost is indicated by the required computation power and time. The lower the temperature the harder the equilibrium process is and the more expensive the computation cost is. For decades people have been working on trying to reach equilibrium state at as low temperature as possible for glassy systems. The “Swap Monte Carlo” method has been shown to have excellent performance for this purpose. The key point here is that the method crucially relies on having sufficiently broad polydispersity so that Monte Carlo swaps of particle radii help equilibrate the system. Our results are thus important for this area and hopefully can raise more interesting studies along this route.

My second project is about a different “room” where the application of isomorph theory on glassy systems under shear is studied. A reminder here that isomorph theory shows the existence of a hidden scale invariance for many certain systems. The invariance here can be simply understood as the following. When the density and temperature of a system are scaled properly, many structural and dynamical properties of the system are invariant when expressed in appropriate units. Such a density and temperature curve is called an isomorph. One particular reason that I think the isomorph theory is interesting is that it simplifies the description of the state of matter for isomorphic systems. The two control parameters density and temperature can be essentially unified as one that determines which isomorph the system is at, which is the beauty of the theory. It also provides an alternative perspective to understand the behaviors of glassy systems and many interesting physics have been learned. For example, new insights have been shown to the understanding of the density-temperature state diagram. The glass transition line is also an isomorph for isomorphic systems. Glass transition line separates the glass and liquid states on the state diagram (see chapter one for more information). Crunching and quenching are also related through the theory. Crunching an isomorphic system to a different density is essentially the same as quenching to the final state from a state point with isomorphic temperature to the starting state and same density as the final state. The thermal histories of the two different ways are shown to be the same.

We verified the applicability of the isomorph theory on glassy systems at finite temperature under shear for steady state. Recall that after the elastic response, a glassy system in general first goes through a transient state where the stress usually shows an overshoot and then enters the steady state where the stress fluctuates around a certain value. Invariance of many quantities are verified. More importantly, we show that the steady state stress is isomorphic while the peak stress at the transient state is not. There must be some key differences between the transient and steady states that cause the distinct results. We provide an initial investigation on the spatial heterogeneity and nonaffinity for the two states which do show some differences. Nonaffinity quantifies the overall degree of deviation of individual particle motions to the affine shear motion. More work is needed. In fact, we note that the finding of the opposite isomorphic behaviors of the two states indeed supports the “alternative perspective” idea mentioned above, which triggers new questions waiting to be answered.

In conslusion, we show the effects of polydispersity and application of isomorph theory on glassy systems under shear. Further studies are required to understand 1) more other properties of the polydisperse systems and 2) the differences between the transient and steady state that cause the non-isomorphic peak stress at the transient state.

Bibliography

[1] M. P. Allen and D. J. Tildesley. *Computer Simulation of Liquids*. Oxford University Press, 1987.

[2] S. Ardanza-Trevijano, Iker Zuriguel, Roberto Arévalo, and Diego Maza. Topological analysis of tapped granular media using persistent homology. *Phys. Rev. E*, 89(5):052212, May 2014. doi: 10.1103/physreve.89.052212.

[3] N. P. Bailey, J. Schiøtz, Anaël Lemaître, and K. W. Jacobsen. Avalanche size scaling in sheared three-dimensional amorphous solid. *Phys. Rev. Lett.*, 98: 095501, 2007.

[4] N. P. Bailey, T. Christensen, B. Jakobsen, K. Niss, N. B. Olsen, U. R. Pedersen, T. B. Schrøder, and J. C. Dyre. Glass-forming liquids: One or more "order" parameters? *J. Phys.: Condens. Matter*, 20:244113, 2008.

[5] N. P. Bailey, U. R. Pedersen, N. Gnan, T. B. Schrøder, and J. C. Dyre. Pressure-energy correlations in liquids. I. Results from computer simulations. *J. Chem. Phys.*, 129:184507, 2008. doi: 10.1063/1.2982247.

[6] N. P. Bailey, U. R. Pedersen, N. Gnan, T. B. Schrøder, and J. C. Dyre. Pressure-energy correlations in liquids. II. Analysis and consequences. *J. Chem. Phys.*, 129:184508, 2008. doi: 10.1063/1.2982249.

[7] M. Ballauff, J. M. Brader, S. U. Egelhaaf, M. Fuchs, J. Horbach, N. Koumakis,

M. Krüger, M. Laurati, K. J. Mutch, G. Petekidis, M. Siebenbürger, Th. Voigtmann, and J. Zausch. Residual Stresses in Glasses. *Physical Review Letters*, 110 (21):215701, May 2013. ISSN 0031-9007, 1079-7114. doi: 10.1103/PhysRevLett.110.215701. URL `https://link.aps.org/doi/10.1103/PhysRevLett.110.215701`.

[8] Victor Bapst, Thomas Keck, A Grabska-Barwińska, Craig Donner, Ekin Dogus Cubuk, Samuel S Schoenholz, Annette Obika, Alexander WR Nelson, Trevor Back, Demis Hassabis, et al. Unveiling the predictive power of static structure in glassy systems. *Nature Physics*, 16(4):448–454, 2020.

[9] G. K. Batchelor and J. T. Green. The determination of the bulk stress in a suspension of spherical particles to order c^2. *Journal of Fluid Mechanics*, 56(3): 401–427, December 1972. doi: 10.1017/S0022112072002435.

[10] J. Bergenholtz, J. F. Brady, and M. Vicic. The non-Newtonian rheology of dilute colloidal suspensions. *Journal of Fluid Mechanics*, 456:239–275, April 2002. doi: 10.1017/S0022112001007583.

[11] L. Berthier and J.-L. Barrat. Nonequilibrium dynamics and fluctuation-dissipation relation in a sheared fluid. *J. Chem. Phys.*, 116:6228–6242, 2002. doi: 10.1063/1.1460862.

[12] Emanuele Boattini, Frank Smallenburg, and Laura Filion. Averaging local structure to predict the dynamic propensity in supercooled liquids. *Physical Review Letters*, 127(8):088007, 2021.

[13] L. Bøhling, T. S. Ingebrigtsen, A. Grzybowski, M. Paluch, J. C. Dyre, and T. B. Schrøder. Scaling of viscous dynamics in simple liquids: theory, simulation and experiment. *New J. Phys.*, 14:113035, 2012. doi: 10.1088/1367-2630/14/11/113035.

[14] L. Bøhling, N. P. Bailey, T. B. Schrøder, and J. C. Dyre. Estimating the density-scaling exponent of a monatomic liquid from its pair potential. *J. Chem. Phys.*, 140:124510, 2014. doi: 10.1063/1.4869114.

[15] David Cantor, Emilien Azéma, Philippe Sornay, and Farhang Radjai. Rheology and structure of polydisperse three-dimensional packings of spheres. *Phys. Rev. E*, 98(5):052910, November 2018. doi: 10.1103/PhysRevE.98.052910. URL `https://link.aps.org/doi/10.1103/PhysRevE.98.052910`.

[16] Cong Cao, Jianshan Liao, Victor Breedveld, and Eric R. Weeks. Rheology finds distinct glass and jamming transitions in emulsions. *Soft Matter*, 17(9):2587–2595, 2021. ISSN 1744-683X, 1744-6848. doi: 10.1039/D0SM02097D. URL `http://xlink.rsc.org/?DOI=D0SM02097D`.

[17] J. Chattoraj, C. Caroli, and A. Lemaître. Universal Additive Effect of Temperature on the Rheology of Amorphous Solids. *Phys. Rev. Lett.*, 105:266001, 2010.

[18] J. Chattoraj, C. Caroli, and A. Lemaître. Robustness of avalanche dynamics in sheared amorphous solids as probed by transverse diffusion. *Phys. Rev. E*, 84: 011501, 2011.

[19] Dandan Chen, Denis Semwogerere, Jun Sato, Victor Breedveld, and Eric R. Weeks. Microscopic structural relaxation in a sheared supercooled colloidal liquid. *Phys. Rev. E*, 81(1):011403, January 2010. doi: 10.1103/physreve.81.011403.

[20] Fuzhen Chen and Hong Yan. Elastic–viscoplastic constitutive theory of dense granular flow and its three-dimensional numerical realization. *Physics of Fluids*, 33(12):123310, December 2021. ISSN 1070-6631, 1089-7666. doi: 10.1063/5.0068458. URL `https://aip.scitation.org/doi/10.1063/5.0068458`.

[21] Kang Chen, Erica J. Saltzman, and Kenneth S. Schweizer. Molecular Theories of Segmental Dynamics and Mechanical Response in Deeply Supercooled Polymer Melts and Glasses. *Annual Review of Condensed Matter Physics*, 1(1):277–300, August 2010. ISSN 1947-5454, 1947-5462. doi: 10.1146/annurev-conmatphys-070909-104110. URL `https://www.annualreviews.org/doi/10.1146/annurev-conmatphys-070909-104110`.

[22] Vijayakumar Chikkadi, Gerard Wegdam, Daniel Bonn, Bernard Nienhuis, and Peter Schall. Long-Range strain correlations in sheared colloidal glasses. *Phys. Rev. Lett.*, 107(19):198303, November 2011. doi: 10.1103/physrevlett.107.198303.

[23] Hyun Woo Cho, Gyemin Kwon, Bong June Sung, and Arun Yethiraj. Effect of polydispersity on diffusion in random obstacle matrices. *Phys. Rev. Lett.*, 109 (15):155901, October 2012. doi: 10.1103/PhysRevLett.109.155901.

[24] J. S. Chong, E. B. Christiansen, and A. D. Baer. Rheology of concentrated suspensions. *J. Appl. Polym. Sci.*, 15(8):2007–2021, August 1971. doi: 10.1002/app.1971.070150818.

[25] Dong Jae Chun, Younghoon Oh, and Bong June Sung. Translation-rotation decoupling of tracers reflects medium-range crystalline order in two-dimensional colloid glasses. *Physical Review E*, 104(5):054615, November 2021. ISSN 2470-0045, 2470-0053. doi: 10.1103/PhysRevE.104.054615. URL `https://link.aps.org/doi/10.1103/PhysRevE.104.054615`.

[26] J. Clara-Rahola, T. A. Brzinski, D. Semwogerere, K. Feitosa, J. C. Crocker, J. Sato, V. Breedveld, and Eric R. Weeks. Affine and nonaffine motions in sheared polydisperse emulsions. *Phys. Rev. E*, 91(1):010301(R), January 2015. doi: 10.1103/physreve.91.010301.

[27] Joel T. Clemmer, Ishan Srivastava, Gary S. Grest, and Jeremy B. Lechman. Shear Is Not Always Simple: Rate-Dependent Effects of Flow Type on Granular Rheology. *Physical Review Letters*, 127(26):268003, December 2021. ISSN 0031-9007, 1079-7114. doi: 10.1103/PhysRevLett.127.268003. URL `https://link.aps.org/doi/10.1103/PhysRevLett.127.268003`.

[28] L. Costigliola, D. M. Heyes, T. B. Schrøder, and J. C. Dyre. Revisiting the Stokes-Einstein relation without a hydrodynamic diameter. *J. Chem. Phys.*, 150:021101, 2019. doi: 10.1063/1.5080662.

[29] Philippe Coussot and Stphane Boyer. Determination of yield stress fluid behaviour from inclined plane test. *Rheologica Acta*, 34(6):534–543, 1995. ISSN 0035-4511, 1435-1528. doi: 10.1007/BF00712314. URL `http://link.springer.com/10.1007/BF00712314`.

[30] E. D. Cubuk, S. S. Schoenholz, J. M. Rieser, B. D. Malone, J. Rottler, D. J. Durian, E. Kaxiras, and A. J. Liu. Identifying structural flow defects in disordered solids using machine-learning methods. *Phys. Rev. Lett.*, 114(10):108001, March 2015. doi: 10.1103/physrevlett.114.108001.

[31] E. D. Cubuk, R. J. S. Ivancic, S. S. Schoenholz, D. J. Strickland, A. Basu, Z. S. Davidson, J. Fontaine, J. L. Hor, Y. R. Huang, Y. Jiang, N. C. Keim, K. D. Koshigan, J. A. Lefever, T. Liu, X. G. Ma, D. J. Magagnosc, E. Morrow, C. P. Ortiz, J. M. Rieser, A. Shavit, T. Still, Y. Xu, Y. Zhang, K. N. Nordstrom, P. E. Arratia, R. W. Carpick, D. J. Durian, Z. Fakhraai, D. J. Jerolmack, Daeyeon Lee, Ju Li, R. Riggleman, K. T. Turner, A. G. Yodh, D. S. Gianola, and Andrea J. Liu. Structure-property relationships from universal signatures of plasticity in disordered solids. *Science*, 358(6366):1033–1037, November 2017. doi: 10.1126/science.aai8830.

[32] Nicolas Cuny, Eric Bertin, and Romain Mari. Dynamics of microstructure anisotropy and rheology of soft jammed suspensions. *Soft Matter*, 18(2):328–339, 2022. ISSN 1744-683X, 1744-6848. doi: 10.1039/D1SM01345A. URL `http://xlink.rsc.org/?DOI=D1SM01345A`.

[33] Peter J. Daivis and B. D. Todd. A simple, direct derivation and proof of the validity of the SLLOD equations of motion for generalized homogeneous flows. *The Journal of Chemical Physics*, 124(19):194103, May 2006. ISSN 0021-9606, 1089-7690. doi: 10.1063/1.2192775. URL `http://aip.scitation.org/doi/10.1063/1.2192775`.

[34] Kenneth W. Desmond and Eric R. Weeks. Measurement of stress redistribution in flowing emulsions. *Phys. Rev. Lett.*, 115(9):098302, August 2015. doi: 10.1103/physrevlett.115.098302.

[35] Kenneth W. Desmond, Pearl J. Young, Dandan Chen, and Eric R. Weeks. Experimental study of forces between quasi-two-dimensional emulsion droplets near jamming. *Soft Matter*, 9(12):3424–3436, October 2013. doi: 10.1039/c3sm27287g.

[36] Jun Ding, Sylvain Patinet, Michael L Falk, Yongqiang Cheng, and Evan Ma. Soft spots and their structural signature in a metallic glass. *Proceedings of the National Academy of Sciences*, 111(39):14052–14056, 2014.

[37] Thibaut Divoux, Catherine Barentin, and Sebastien Manneville. Stress overshoot in a simple yield stress fluid: An extensive study combining rheology and velocimetry. *Soft Matter*, 7(19):9335–9349, 2011. doi: 10.1039/c1sm05740e.

[38] Remi Dreyfus, Ye Xu, Tim Still, L. A. Hough, A. G. Yodh, and Salvatore Torquato. Diagnosing hyperuniformity in two-dimensional, disordered, jammed

packings of soft spheres. *Phys. Rev. E*, 91(1), January 2015. doi: 10.1103/physreve.91.012302.

[39] Roel P. A. Dullens and Clemens Bechinger. Shear thinning and local melting of colloidal crystals. *Phys. Rev. Lett.*, 107:138301, September 2011. doi: 10.1103/physrevlett.107.138301.

[40] D. J. Durian. Foam mechanics at the bubble scale. *Phys. Rev. Lett.*, 75(26): 4780–4783, December 1995. doi: 10.1103/physrevlett.75.4780.

[41] J. C. Dyre. Simple liquids' quasiuniversality and the hard-sphere paradigm. *J. Phys.: Condens. Mat.*, 28:323001, 2016. doi: 10.1088/0953-8984/28/32/323001.

[42] Jeppe C. Dyre. Isomorph theory of physical aging. *J. chem. Phys.*, 148:154502, 2018.

[43] Jeppe C. Dyre. Isomorph theory of physical aging. *The Journal of Chemical Physics*, 148(15):154502, April 2018. ISSN 0021-9606, 1089-7690. doi: 10.1063/1.5022999. URL `http://aip.scitation.org/doi/10.1063/1.5022999`.

[44] Jeppe C. Dyre. Isomorph theory beyond thermal equilibrium. *The Journal of Chemical Physics*, 153(13):134502, October 2020. ISSN 0021-9606, 1089-7690. doi: 10.1063/5.0024212. URL `http://aip.scitation.org/doi/10.1063/5.0024212`.

[45] Lance E. Edens, Enrique G. Alvarado, Abhinendra Singh, Jeffrey F. Morris, Gregory K. Schenter, Jaehun Chun, and Aurora E. Clark. Shear stress dependence of force networks in 3D dense suspensions. *Soft Matter*, 17(32):7476–7486, 2021. ISSN 1744-683X, 1744-6848. doi: 10.1039/D1SM00184A. URL `http://xlink.rsc.org/?DOI=D1SM00184A`.

[46] M. D. Ediger and J. A. Forrest. Dynamics near free surfaces and the glass transition in thin polymer films: A view to the future. *Macromolecules*, 47(2): 471–478, January 2014. doi: 10.1021/ma4017696.

[47] D. J. Evans and G. Morriss. *Statistical Mechanics of Nonequilibrium Liquids*. Cambridge University Press, second edition, 2008.

[48] M. L. Falk and J. S. Langer. Dynamics of viscoplastic deformation in amorphous solids. *Phys. Rev. E*, 57:7192–7205, 1998.

[49] M. L. Falk and J. S. Langer. Dynamics of viscoplastic deformation in amorphous solids. *Phys. Rev. E*, 57(6):7192–7205, June 1998. doi: 10.1103/physreve.57.7192.

[50] Michael L. Falk and J. S. Langer. Deformation and failure of amorphous, solidlike materials. *Ann. Rev. Cond. Mat. Phys.*, 2(1):353–373, 2011. doi: 10.1146/annurev-conmatphys-062910-140452.

[51] N. Gnan, T. B. Schrøder, U. R. Pedersen, N. P. Bailey, and J. C. Dyre. Pressure-energy correlations in liquids. IV. 'Isomorphs' in liquid state diagrams. *J. Chem. Phys.*, 131:234504, 2009. doi: 10.1063/1.3265957.

[52] N. Gnan, C. Maggi, T. B. Schrøder, and J. C. Dyre. Predicting the effective temperature of a glass. *Phys. Rev. Lett.*, 104:125902, 2010.

[53] Nicoletta Gnan, Thomas B. Schrøder, Ulf R. Pedersen, Nicholas P. Bailey, and Jeppe C. Dyre. Pressure-energy correlations in liquids. IV. " isomorphs" in liquid phase diagrams. *J. Chem. Phys.*, 131(23):234504+, December 2009. doi: 10.1063/1.3265957.

[54] C. Goldenberg, A. Tanguy, and J.-L. Barrat. Particle displacements in the elastic deformation of amorphous materials: Local fluctuations *vs.* non-affine

field. *Europhysics Letters (EPL)*, 80(1):16003, October 2007. ISSN 0295-5075, 1286-4854. doi: 10.1209/0295-5075/80/16003. URL `https://iopscience.iop.org/article/10.1209/0295-5075/80/16003`.

[55] P. Hébraud, F. Lequeux, J. P. Munch, and D. J. Pine. Yielding and rearrangements in disordered emulsions. *Phys. Rev. Lett.*, 78(24):4657–4660, June 1997. doi: 10.1103/physrevlett.78.4657.

[56] D. Heckendorf, K. J. Mutch, S. U. Egelhaaf, and M. Laurati. Size-dependent localization in polydisperse colloidal glasses. *Phys. Rev. Lett.*, 119(4), July 2017. doi: 10.1103/physrevlett.119.048003.

[57] Xia Hong, Meghan Kohne, Mia Morrell, Haoran Wang, and Eric R. Weeks. Clogging of soft particles in two-dimensional hoppers. *Phys. Rev. E*, 96(6): 062605, December 2017. doi: 10.1103/physreve.96.062605.

[58] W. G. Hoover. Canonical dynamics: Equilibrium phase-space distributions. *Phys. Rev. A*, 31:1695–1697, 1985.

[59] F. Hummel, G. Kresse, J. C. Dyre, and U. R. Pedersen. Hidden scale invariance of metals. *Phys. Rev. B*, 92:174116, 2015. doi: 10.1103/PhysRevB.92.174116.

[60] Gary L. Hunter and Eric R. Weeks. The physics of the colloidal glass transition. *Rep. Prog. Phys.*, 75(6):066501, May 2012. doi: 10.1088/0034-4885/75/6/066501.

[61] Atsushi Ikeda, Ludovic Berthier, and Peter Sollich. Unified study of glass and jamming rheology in soft particle systems. *Phys. Rev. Lett.*, 109:018301, July 2012. doi: 10.1103/physrevlett.109.018301.

[62] T. S. Ingebrigtsen, L. Bøhling, T. B. Schrøder, and J. C. Dyre. Thermodynamics

of condensed matter with strong pressure-energy correlations. *J. Chem. Phys.*, 136:061102, 2012. doi: 10.1063/1.3685804.

[63] T. S. Ingebrigtsen, T. B. Schrøder, and J. C. Dyre. What is a simple liquid? *Phys. Rev. X*, 2:011011, 2012. doi: 10.1103/PhysRevX.2.011011.

[64] T. S. Ingebrigtsen, T. B. Schrøder, and J. C. Dyre. Isomorphs in model molecular liquids. *J. Phys. Chem. B*, 116:1018, 2012.

[65] T. S. Ingebrigtsen, J. C. Dyre, T. B. Schrøder, and C. P. Royall. Crystallization Instability in Glassforming Mixtures. 2018.

[66] Charlotte Jacobsen, Karsten Hartvigsen, Pia Lund, Anne S Meyer, Jens Adler-Nissen, Jens Holstborg, and Gunhild Hølmer. Oxidation in fish-oil-enriched mayonnaise. page 18.

[67] Yonglun Jiang, Eric R. Weeks, and Nicholas P. Bailey. Isomorph invariance of dynamics of sheared glassy systems. *Phys. Rev. E*, 100(5):053005, November 2019. doi: 10.1103/PhysRevE.100.053005. URL `https://link.aps.org/doi/10.1103/PhysRevE.100.053005`.

[68] Jissy Jose, Gerhard A. Blab, Alfons van Blaaderen, and Arnout Imhof. Jammed elastic shells - a 3D experimental soft frictionless granular system. *Soft Matter*, 11(9):1800–1813, 2015. doi: 10.1039/c4sm02098g.

[69] Yogesh M. Joshi and George Petekidis. Yield stress fluids and ageing. *Rheologica Acta*, 57(6-7):521–549, June 2018. doi: 10.1007/s00397-018-1096-6.

[70] Ken Kamrin and Georg Koval. Nonlocal constitutive relation for steady granular flow. *Phys. Rev. Lett.*, 108(17):178301, April 2012. doi: 10.1103/physrevlett.108.178301.

[71] W. Kob and H. C. Andersen. Scaling behavior in the β-relaxation regime of a supercooled Lennard-Jones mixture. *Phys. Rev. Lett.*, 73:1376–1379, 1994.

[72] W. Kob and H. C. Andersen. Testing mode-coupling theory for a supercooled binary Lennard-Jones mixture I: The van Hove correlation function. *Phys. Rev. E*, 51:4626–4641, 1995.

[73] W. Kob and H. C. Andersen. Testing mode-coupling theory for a supercooled binary Lennard-Jones mixture. II. Intermediate scattering function and dynamic susceptibility. *Phys. Rev. E*, 52:4134–4153, 1995.

[74] W. Kob and J.-L. Barrat. Fluctuations, response and aging dynamics in a simple glass-forming liquid out of equilibrium. *Eur. Phys. J. B*, 13:319–333, 2000.

[75] Florent Krzakala and Jorge Kurchan. Landscape analysis of constraint satisfaction problems. *Physical Review E*, 76(2):021122, August 2007. doi: 10.1103/PhysRevE.76.021122. URL `https://link.aps.org/doi/10.1103/PhysRevE.76.021122`.

[76] Sameer Kumar, Jay Prakash Singh, Debaprasad Giri, and Shradha Mishra. Effect of polydispersity on the dynamics of active Brownian particles. *Phys. Rev. E*, 104(2):024601, August 2021. doi: 10.1103/PhysRevE.104.024601.

[77] A. J. C. Ladd. Equations of motion for non-equilibrium molecular-dynamics simulations of viscous-flow in molecular liquids. *Mol. Phys.*, 53:459, 1984. doi: 10.1080/00268978400102441.

[78] Stephen A. Langer and Andrea J. Liu. Effect of Random Packing on Stress Relaxation in Foam. *The Journal of Physical Chemistry B*, 101(43):8667–8671, October 1997. ISSN 1520-6106, 1520-5207. doi: 10.1021/jp971265b. URL `https://pubs.acs.org/doi/10.1021/jp971265b`.

[79] A. Lemaître and C. Caroli. Plastic response of a two-dimensional amorphous solid to quasistatic shear: Transverse particle diffusion and phenomenology of dissipative events. *Phys. Rev. E*, 76:036104, 2007.

[80] A. Lemaître and C. Caroli. Rate-dependent Avalanche Size in Athermally Sheared Amorphous Solids. *Phys. Rev. Lett.*, 103:065501, 2009.

[81] Anaël Lemaître and Christiane Caroli. Rate-Dependent avalanche size in athermally sheared amorphous solids. *Phys. Rev. Lett.*, 103(6):065501, August 2009. doi: 10.1103/physrevlett.103.065501.

[82] E. Lerner and I. Procaccia. Scaling theory for steady-state plastic flows in amorphous solids . *Phys. Rev. E*, 80:026128, 2009.

[83] E. Lerner and I. Procaccia. Locality and nonlocality in elastoplastic responses of amorphous solids. *Phys. Rev. E*, 79:066109, 2009. doi: 10.1103/PhysRevE.79.066109.

[84] E. Lerner and I. Procaccia. Density Scaling of Avalanche Statistics in Amorphous Solids. 2009.

[85] Edan Lerner, Nicholas P. Bailey, and Jeppe C. Dyre. Density scaling and quasiuniversality of flow-event statistics for athermal plastic flows. *Phys. Rev. E*, 90:052304, 2014.

[86] Andrea J. Liu and Sidney R. Nagel. Jamming is not just cool any more. *Nature*, 396(6706):21–22, November 1998. doi: 10.1038/23819.

[87] Andrea J. Liu, Sriram Ramaswamy, T. G. Mason, Hu Gang, and D. A. Weitz. Anomalous viscous loss in emulsions. *Phys. Rev. Lett.*, 76(16):3017–3020, April 1996. doi: 10.1103/physrevlett.76.3017.

[88] Xiaohui Liu, Joel A. Lefever, Daeyeon Lee, Jie Zhang, Robert W. Carpick, and Ju Li. Friction and Adhesion Govern Yielding of Disordered Nanoparticle Packings: A Multiscale Adhesive Discrete Element Method Study. *Nano Letters*, 21(19):7989–7997, October 2021. ISSN 1530-6984, 1530-6992. doi: 10.1021/acs.nanolett.1c01952. URL `https://pubs.acs.org/doi/10.1021/acs.nanolett.1c01952`.

[89] V. Lubchenko and P. G. Wolynes. Theory of Structural Glasses and Supercooled Liquids. *Ann. Rev. Phys. Chem.*, 58:235–266, 2007.

[90] Xiaoguang Ma, Zoey S. Davidson, Tim Still, Robert J. . S. Ivancic, S. . S. Schoenholz, A. . J. Liu, and A. . G. Yodh. Heterogeneous activation, local structure, and softness in supercooled colloidal liquids. *Phys. Rev. Lett.*, 122 (2), January 2019. doi: 10.1103/physrevlett.122.028001.

[91] Moumita Maiti and Srikanth Sastry. Free volume distribution of nearly jammed hard sphere packings. *J. Chem. Phys.*, 141(4):044510, July 2014. doi: 10.1063/1.4891358.

[92] D. L. Malandro and D. J. Lacks. Molecular-level mechanical instabilities and enhanced self-diffusion in flowing liquids. *Phys. Rev. Lett.*, 81:5576–5579, 1998.

[93] C. Maloney and A. Lemaître. Subextensive scaling in the athermal, quasistatic limit of amorphous matter in plastic shear flow. *Phys. Rev. Lett.*, 93:016001, 2004.

[94] C. E. Maloney and A. Lemaître. Amorphous Systems in Athermal, Quasistatic Shear. *Phys. Rev. E*, 74:016118, 2006.

[95] M. L. Manning and A. J. Liu. Vibrational modes identify soft spots in a sheared disordered packing. *Phys. Rev. Lett.*, 107:108302, August 2011. doi: 10.1103/physrevlett.107.108302.

[96] Jeffrey D. Martin and Y. Thomas Hu. Transient and steady-state shear banding in aging soft glassy materials. *Soft Matter*, 8(26):6940–6949, 2012. doi: 10.1039/c2sm25299f.

[97] T. G. Mason, Martin-D Lacasse, Gary S. Grest, Dov Levine, J. Bibette, and D. A. Weitz. Osmotic pressure and viscoelastic shear moduli of concentrated emulsions. *Phys. Rev. E*, 56(3):3150–3166, September 1997. doi: 10.1103/physreve.56.3150.

[98] Lavanya Mohan, Roger T. Bonnecaze, and Michel Cloitre. Microscopic Origin of Internal Stresses in Jammed Soft Particle Suspensions. *Physical Review Letters*, 111(26):268301, December 2013. ISSN 0031-9007, 1079-7114. doi: 10.1103/PhysRevLett.111.268301. URL `https://link.aps.org/doi/10.1103/PhysRevLett.111.268301`.

[99] Duc-Hanh Nguyen, Emilien Azéma, Farhang Radjai, and Philippe Sornay. Effect of size polydispersity versus particle shape in dense granular media. *Phys. Rev. E*, 90(1):012202, July 2014. doi: 10.1103/PhysRevE.90.012202.

[100] Duc-Hanh Nguyen, Emilien Azéma, Philippe Sornay, and Farhang Radjai. Effects of shape and size polydispersity on strength properties of granular materials. *Phys. Rev. E*, 91(3):032203, March 2015. doi: 10.1103/PhysRevE.91.032203. URL `https://link.aps.org/doi/10.1103/PhysRevE.91.032203`.

[101] Andrea Ninarello, Ludovic Berthier, and Daniele Coslovich. Models and algorithms for the next generation of glass transition studies. *Physical Review X*, 7(2):021039, 2017.

[102] Corey S. O'Hern, Leonardo E. Silbert, Andrea J. Liu, and Sidney R. Nagel. Jamming at zero temperature and zero applied stress: The epitome of disorder. *Phys. Rev. E*, 68(1):011306, July 2003. doi: 10.1103/physreve.68.011306.

[103] Peter Olsson and S. Teitel. Critical scaling of shearing rheology at the jamming transition of soft-core frictionless disks. *Phys. Rev. E*, 83(3):030302, March 2011. doi: 10.1103/physreve.83.030302.

[104] Ian K. Ono, Corey S. O'Hern, D. J. Durian, Stephen A. Langer, Andrea J. Liu, and Sidney R. Nagel. Effective temperatures of a driven system near jamming. *Phys. Rev. Lett.*, 89(9):095703, August 2002. doi: 10.1103/physrevlett.89.095703.

[105] Sylvain Patinet, Damien Vandembroucq, and Michael L Falk. Connecting local yield stresses with plastic activity in amorphous solids. *Physical review letters*, 117(4):045501, 2016.

[106] U. R. Pedersen, N. P. Bailey, T. B. Schrøder, and J. C. Dyre. Strong Pressure-Energy Correlations in Van der Waals Liquids. *Phys. Rev. Lett.*, 100:015701, 2008. doi: 10.1103/PhysRevLett.100.015701.

[107] Sidhant Pednekar, Jaehun Chun, and Jeffrey F. Morris. Bidisperse and polydisperse suspension rheology at large solid fraction. *J. Rheo.*, 62(2):513–526, March 2018. doi: 10.1122/1.5011353.

[108] Hugo Perrin, Cécile Clavaud, Matthieu Wyart, Bloen Metzger, and Yoël Forterre. Interparticle Friction Leads to Nonmonotonic Flow Curves and Hysteresis in Viscous Suspensions. *Physical Review X*, 9(3):031027, August 2019. ISSN 2160-3308. doi: 10.1103/PhysRevX.9.031027. URL `https://link.aps.org/doi/10.1103/PhysRevX.9.031027`.

[109] Hugo Perrin, Matthieu Wyart, Bloen Metzger, and Yoël Forterre. Nonlocal Effects Reflect the Jamming Criticality in Frictionless Granular Flows Down Inclines. *Physical Review Letters*, 126(22):228002, June 2021. ISSN 0031-9007,

1079-7114. doi: 10.1103/PhysRevLett.126.228002. URL `https://link.aps.org/doi/10.1103/PhysRevLett.126.228002`.

[110] G. Petekidis, A. Moussaïd, and P. N. Pusey. Rearrangements in hard-sphere glasses under oscillatory shear strain. *Phys. Rev. E*, 66(5):051402, November 2002. doi: 10.1103/physreve.66.051402.

[111] W. H. Press, S. A. Teukolsky, William T. Vetterling, and Brian P. Flannery. *Numerical Recipes in C*. Cambridge University Press, second edition, 1992.

[112] William H. Press, Brian P. Flannery, Saul A. Teukolsky, and William T. Vetterling. *Numerical Recipes in C: The Art of Scientific Computing, Second Edition*. Cambridge University Press, Cambridge ; New York, 2nd edition, October 1992. ISBN 978-0-521-43108-8.

[113] Rodney D. Priestley. Physical aging of confined glasses. *Soft Matter*, 5(5): 919–926, 2009. doi: 10.1039/b816482g.

[114] Douglas Ridgway, Gordon Broderick, Ana Lopez-Campistrous, Melania Ru'aini, Philip Winter, Matthew Hamilton, Pierre Boulanger, Andriy Kovalenko, and Michael J. Ellison. Coarse-grained molecular simulation of diffusion and reaction kinetics in a crowded virtual cytoplasm. *Biophys. J.*, 94(10):3748–3759, May 2008. doi: 10.1529/biophysj.107.116053.

[115] J. Rottler and M. O. Robbins. Shear yielding of amorphous glass solids: Effect of temperature and strain rate. *Phys. Rev. E.*, 68:011507, 2003. doi: 10.1103/PhysRevE.68.011507.

[116] J. Rottler and M. O. Robbins. Yield conditions for deformation of amorphous polymer glasses. *Phys. Rev. E*, 64:051801, 2005.

[117] Peter Schall, David A. Weitz, and Frans Spaepen. Structural rearrangements that govern flow in colloidal glasses. *Science*, 318(5858):1895–1899, December 2007. doi: 10.1126/science.1149308.

[118] S. S. Schoenholz, E. D. Cubuk, D. M. Sussman, E. Kaxiras, and A. J. Liu. A structural approach to relaxation in glassy liquids. *Nature Phys.*, 12(5):469–471, February 2016. doi: 10.1038/nphys3644.

[119] T. B. Schrøder and J. C. Dyre. Simplicity of condensed matter at is core: Generic definition of a Roskilde-simple system. *J. Chem. Phys.*, 141:204502, 2014. doi: 10.1063/1.4901215.

[120] T. B. Schrøder, N. P. Bailey, U. R. Pedersen, N. Gnan, and J. C. Dyre. Pressure-energy correlations in liquids. III. Statistical Mechanics and thermodynamics of liquids with hidden scale invariance. *J. Chem. Phys.*, 131:234503, 2009. doi: 10.1063/1.3265955.

[121] T. B. Schrøder, N. Gnan, U. R. Pedersen, N. P. Bailey, and J. C. Dyre. Pressure-energy correlations in liquids. V. Isomorphs in generalized Lennard-Jones systems. *J. Chem. Phys.*, 134:164505, 2011. doi: 10.1063/1.3582900.

[122] G. E. Schröder-Turk, W. Mickel, M. Schröter, G. W. Delaney, M. Saadatfar, T. J. Senden, K. Mecke, and T. Aste. Disordered spherical bead packs are anisotropic. *Europhys. Lett.*, 90(3):34001+, May 2010. doi: 10.1209/0295-5075/90/34001.

[123] Prateek Sehgal, Meera Ramaswamy, Itai Cohen, and Brian J. Kirby. Using Acoustic Perturbations to Dynamically Tune Shear Thickening in Colloidal Suspensions. *Physical Review Letters*, 123(12):128001, September 2019. ISSN 0031-9007, 1079-7114. doi: 10.1103/PhysRevLett.123.128001. URL `https://link.aps.org/doi/10.1103/PhysRevLett.123.128001`.

[124] L. Separdar, N. P. Bailey, T. B. Schrøder, S. Davatolhagh, and J. C. Dyre. Isomorph invariance of Couette shear flows simulated by the SLLOD equations of motion. *J. Chem. Phys.*, 138:154505, 2013. doi: 10.1063/1.4799273.

[125] Murari Singh, Misaki Ozawa, and Ludovic Berthier. Brittle yielding of amorphous solids at finite shear rates. *Physical Review Materials*, 4(2):025603, February 2020. ISSN 2475-9953. doi: 10.1103/PhysRevMaterials.4.025603. URL `https://link.aps.org/doi/10.1103/PhysRevMaterials.4.025603`.

[126] Peter Sollich and Nigel B. Wilding. Crystalline phases of polydisperse spheres. *Phys. Rev. Lett.*, 104(11):118302, March 2010. doi: 10.1103/physrevlett.104.118302.

[127] Frank H. Stillinger and Pablo G. Debenedetti. Glass Transition Thermodynamics and Kinetics. *Annual Review of Condensed Matter Physics*, 4(1):263–285, April 2013. ISSN 1947-5454, 1947-5462. doi: 10.1146/annurev-conmatphys-030212-184329. URL `https://www.annualreviews.org/doi/10.1146/annurev-conmatphys-030212-184329`.

[128] Daniel M. Sussman, Samuel S. Schoenholz, Ekin D. Cubuk, and Andrea J. Liu. Disconnecting structure and dynamics in glassy thin films. *Proc. Nat. Acad. Sci.*, 114(40):10601–10605, October 2017. doi: 10.1073/pnas.1703927114.

[129] A. Tanguy, F. Leonforte, and J. L. Barrat. Plastic response of a 2D Lennard-Jones amorphous solid: Detailed analysis of the local rearrangements at very slow strain rate. *Euro. Phys. J. E*, 20(3):355–364, July 2006. doi: 10.1140/epje/i2006-10024-2.

[130] J. Taylor. *An Introduction to Error Analysis: The Study of Uncertainties in Physical Measurements*. University Science Books, 2 edition, 1996.

[131] S. Torquato and F. H. Stillinger. Jammed hard-particle packings: From kepler to bernal and beyond. *Rev. Mod. Phys.*, 82(3):2633–2672, September 2010. doi: 10.1103/revmodphys.82.2633.

[132] S. Toxvaerd and J. C. Dyre. Shifted forces in molecular dynamics. *J. Chem. Phys.*, 134:081102, 2011. doi: 10.1063/1.3558787.

[133] S. Toxvaerd, U. R. Pedersen, T. B. Schrøder, and J. C. Dyre. Stability of supercooled binary liquid mixtures. *J. Chem. Phys.*, 130:224501, 2009.

[134] Jih-Chiang (JC) Tsai, Guan-Hao Huang, and Cheng-En Tsai. Signature of transition between granular solid and fluid : Rate-dependent stick slips in steady shearing. *Phys. Rev. Lett.*, 126(12):128001, March 2021. doi: 10.1103/PhysRevLett.126.128001.

[135] Brian Utter and R. P. Behringer. Experimental measures of affine and nonaffine deformation in granular shear. *Phys. Rev. Lett.*, 100(20):208302, May 2008. doi: 10.1103/physrevlett.100.208302.

[136] F. Varnik, L. Bocquet, J.-L. Barrat, and L. Berthier. Shear localization in a model glass. *Phys. Rev. Lett.*, 90:095702, 2003.

[137] A. A. Veldhorst, J. C. Dyre, and T. B. Schrøder. Scaling of he dynamics of flexible Lennard-Jones chains. *J. Chem. Phys.*, 141:054904, 2014.

[138] T. Voigtmann. Nonlinear glassy rheology. *Curr. Opin. Colloid In.*, 19:549–560, 2014. doi: 10.1016/j.cocis.2014.11.001.

[139] R. Yamamoto and A. Onuki. Nonlinear rheology of a highly supercooled liquid. *Europhys. Lett.*, 40(1):61–66, 1997.

[140] Rongrong Zhang, Lei Ni, Zhenyu Jin, Jiahong Li, and Fan Jin. Bacteria slingshot more on soft surfaces. *Nature Comm.*, 5:5541+, November 2014. doi: 10.1038/ncomms6541.